UNIVERSITY OF CALIFORNIA
RIVERSIDE

Analysis of Shear-horizontal Vibrations of Crystal Plates for Acoustic Wave Resonators and Sensors

A Dissertation submitted in partial satisfaction
of the requirements for the degree of

Doctor of Philosophy

in

Mechanical Engineering

by

Bo Liu

August 2010

Dissertation Committee:

Dr. Qing Jiang, Chairperson

Dr. Guanshui Xu

Dr. Cengiz Ozkan

The dissertation of Bo Liu is approved

_____

_____

_____

Committee Chairperson

University of California, Riverside

Acknowledgements

First of all, I am appreciative and thankful to my advisor Dr. Qing Jiang, for his understanding, patience and kind guidance not only on my research, but also in the daily life. His exceptional scholarship and passion for research have been a source of inspiration to me during my study, and his continuous encouragement and support are greatly appreciated. I would like to thank Dr. Jiashi Yang, professor of Nebraska University, Lincoln. Without his selfless help, my study cannot be accomplished. I also thank Dr. Guanshui Xu, Dr. Cengiz Ozkan, Dr. Javier Garay and Dr. Sheldon Tan for being my dissertation or Ph. D. qualify-exam committee members.

I would like to thank all Dr. Qing Jiang's group members and all Dr. Guanshui Xu's group members, including Dr. Xiaohong Wang, Mr. Younghoon Kim, Dr. Lili, Mr. Ahmad Ali, Dr. Zijun Fang, Dr. Gang Liu and Mr. Gongbo Long. I also own my thanks to my other friends, including Mr. Stephen Chung, Mr. Jiebin Zhong, Miss Yanyan Zhang and Mr. Shiyan Chen. There is still a long name list of my friends. I benefit a lot from our discussion and enjoy the friendship.

I am grateful to my father Mr. Dashu Liu and my mother Ms. Shuling Xie for their love and support in my life. I also thank all my cousins for looking after my parents during my Ph. D. period in US.

ABSTRACT OF THE DISSERTATION

Analysis of Shear-horizontal Vibrations of Crystal Plates for Acoustic Wave Resonators and Sensors

by

Bo Liu

Doctor of Philosophy, Graduate Program in Mechanical Engineering
University of California, Riverside, August 2010
Dr. Qing Jiang, Chairperson

In this work, theoretical analysis of shear-horizontal vibrations of crystal plates under lateral electric field excitation (LFE) without and with a fluid layer is presented. A crystal plate with separated electrodes under thickness electric field excitation (TFE) in contact with a fluid layer is also analyzed.

We have started with analyzing the coupled face-shear (FS) and thickness-twist (TT) motions of piezoelectric plates with lateral electric fields, using the Mindlin's first-order theory of piezoelectric plates. Solutions for propagating waves, and for free and electrically-forced vibrations are obtained, leading to basic vibration characteristics for resonator applications including dispersion relations, frequency spectra, and motional capacitance. Numerical results are presented for AT-cut quartz plates.

We have then studied the coupled face-shear (FS) and thickness-twist (TT) motions of a piezoelectric plate with mass layers on the central parts of the plate surfaces, driven by a lateral electric field. An analytical solution is obtained. Numerical results are presented for an AT-cut quartz plate, including the motional capacitance of the plate as a resonator and vibration modes trapped under the mass layers in the central portion of the plate. The relationship between the dimensions of the mass layers and the number of trapped modes is examined.

We have studied the thickness-shear vibration of a rotated Y-cut quartz crystal plate whose one surface is in contact with a fluid layer. In this study, two configurations are considered. For the first configuration, we have analyzed the plate vibrations driven by a lateral electric field, using both the theory of piezoelectricity and the theory of Newtonian fluids. The solutions for both free and forced vibrations are obtained. Approximate expressions for the frequency shifts in the crystal plate due to the fluid are presented. The admittance of the structure is also calculated. The results illustrate the impacts of the thickness, the density and the viscosity of the fluid layer on the frequency shifts in the plate. In the second configuration, the fluid is under an electrode separated from the crystal plate and the driving electric field is in the plate thickness direction. This configuration qualitatively describes the effect of the liquid permittivity on the frequency shifts in a real LFE liquid sensor.

Finally, I studied the propagation of shear-horizontal waves in a piezoelectric plate in contact with a fluid layer as an acoustic wave sensor for measuring fluid viscosity or

density. Mindlin's first-order theory of piezoelectric plates and the theory of Newtonian fluids are used. Two kinds of fluid layers are considered. One is with finite thickness, and the other is semi-infinite. Approximate dispersion relations for long face-shear and thickness-twist waves are given analytically. In the first one, numerical results only show the effects of the fluid on wave characteristics. In the other, numerical results showing the effects of the fluid and the piezoelectric coupling in the plate on wave characteristics are presented.

Table of Contents

List of Figures

1. Introduction

1.1 Piezoelectric crystals and acoustic wave devices

Piezoelectric materials exhibit electromechanical coupling. They experience mechanical deformations when placed in an electric field, and become electrically polarized under mechanical loads. These materials have been used for a long time to make various electromechanical devices. Examples include transducers for converting electrical energy to mechanical energy or vice versa, resonators and filters for frequency control and selection for telecommunication equipment and precise timing and synchronization, and acoustic wave sensors. Many piezoelectric devices are resonant devices operating at a particular frequency and mode, either a stationary or a propagating wave. Both surface acoustic waves (SAWs) and bulk acoustic waves (BAWs) are used. In the applications of resonant piezoelectric devices, basic vibration characteristics like frequency and wave speed are of primary interest. How wave frequencies vary under, e.g., a temperature change, stress, surface additional mass or contact with a fluid is the foundation of acoustic wave sensors.

In principle, acoustic wave resonators and sensors do not have to be piezoelectric. These devices are based on mechanical vibration modes and waves. Piezoelectric crystals are often used so that the operating wave can be conveniently excited electrically. Otherwise transducers are needed for the excitation and detection of acoustic waves. Quartz is the most widely used material for resonant piezoelectric devices. It has little damping and desirable temperature behaviors buts its piezoelectric coupling is very weak.

During the last two decades the relatively new crystals of langasite, langanite, and langatate were developed which are used more and more for acoustic wave devices. These new crystals have relatively strong piezoelectric coupling. They are especially useful for high-temperature applications. Lithium niobate and lithium langasite crystals are mainly for SAW devices.

For frequency analysis of quartz devices the small piezoelectric coupling can usually be neglected and an elastic analysis is sufficient. Compared to piezoelectric analyses, an elastic analysis of vibration crystals is significantly simpler and can usually exhibit the basic frequency behavior. Generalization from an elastic solution to include piezoelectric effects is not always possible analytically. There are situations in which a piezoelectric analysis is necessary. To obtain the admittance (or impedance) of a device, a piezoelectric analysis of electrically forced vibrations is needed. A free vibration frequency analysis and an electrically forced vibration analysis for admittance together provide a complete simulation of a device. Piezoelectric coupling is known to cause a stiffening effect that raises resonant frequencies. This effect, although often negligible for quartz in qualitative analyses, needs to be considered in more refined analyses or in materials with relatively strong piezoelectric couplings.

1.2 Waves in crystal plates

Piezoelectric plates are common structures for acoustic wave devices. Many waves can exist or propagate in a crystal plate [1, 2]. These waves can be classified as low- and high-frequency waves. The usual extensional (E) and flexural (F) waves in plates

considered in traditional structural engineering are low-frequency waves whose frequencies depend strongly on the length and/or width of a plate in addition to the plate thickness *h*. Face-shear (FS) is another low-frequency wave. A fundamental characteristic of low-frequency waves is that for long waves their frequencies go to zero or the dispersion curves passes the origin. A rather unique feature of plate resonant piezoelectric devices is that they often operate with high-frequency waves called thickness modes including thickness-shear (TSh), thickness-stretch (TSt), and thickness twist (TT) whose frequencies are determined by the plate thickness, the smallest dimension only and therefore they have relatively high frequencies. For long waves their frequencies do not go to zero but have finite intercepts with the ω axis called cutoff frequencies below which the waves cannot propagate. This has important and useful implications in the behaviors of high-frequency waves and device applications. There in fact infinitely many branches of dispersion curves above the ones that are shown in the figure. One of the two dotted lines in the figure is the well-known Rayleigh surface wave ®, which can propagate over an elastic half-space and is not dispersive. The other dotted line is the well known Bleustein-Gulyaev surface wave (BG) [3, 4] which can propagate over a piezoelectric half-space but does not have an elastic counterpart. These two surface waves are included as references. The study of waves in crystal plates for different applications is an active research area [5-10].

Pure thickness modes [11, 12] vary along the plate thickness only and do not have in-plane variations. They can exist in unbounded plates only. In real devices thin plates are used to simulate unbounded plates. However, due to the presence of boundaries, two

complications arise. One is that the thickness modes have slight in-plane variations. The other is that the operating high-frequency mode of a device becomes coupled with low-frequency mode(s). Accurate prediction of the behaviors of low- and high-frequency waves in crystal plates and their interaction is fundamental to the understanding and design of acoustic wave devices. When thickness modes have in-plane variations, there are two important situations. In the first case the operating TSh mode has an in-plane variation in the same direction as the TSh particle displacement and is coupled to the F mode. This case is relatively well studied and understood, see, e.g., [13-18] and a review article [19]. In the second case the operating TSh mode has an in-plane variation in the direction perpendicular to the TSh particle displacement and is coupled to the FS mode. This case is as important but has been studied much less compared to the first case, with few and scattered results [20-25]. There is a lack of basic understanding of this situation. This dissertation is concerned with the second case. In terms of mechanics terminology, this case belongs to the so-called shear-horizontal (SH) or antiplane motions.

1.3 Quartz crystal microbalance (QCM) sensors used in the liquid phase

Nowadays, the quartz crystal microbalance (QCM) sensors using thickness-shear modes (TSM) in AT-cut quartz are widely used in the liquid phase sensing applications. The standard QCM sensors are always driven piezoelectrically by a thickness electric field, known as thickness field excitation (TFE), which is generated by the two electrodes attached on the both parallel main surfaces of the crystal. The detections mechanism is based on the mechanical loading, such as mass, density and viscosity. Because of the

electrode configuration, the sensing surface cannot contact the liquid phase directly which may cause some limitations when the sensors are used as chemical sensors and such sensors are not sensitive to the electrical properties of the liquid, such as the permittivity and the conductivity.

It is also possible to excite the TSM in the AT-cut quartz by applying a lateral electric field, known as lateral field excitation (LFE). There are many obvious advantages of LFE over TFE, such as reduced aging, higher Q values and increased frequency stability, since the regions of the greatest vibrational motion are free of electrodes. Additionally, in sensing applications, the free sensing surface allows the penetration of the TSM mechanical and electrical fields into the liquids, resulting in increased sensitivity to both mechanical and electrical properties changes of the liquids.

So far, there are several LFE sensors fabricated [26-29]. But the fundamental analysis based on the theory of piezoelectricity for such LFE sensors seems to be still missing, which is important for understanding the wave modes and their coupling in the LFE sensors and also for designing the sensors.

1.4 Modeling of plate acoustic wave devices

Due to the material anisotropy of crystals and piezoelectric coupling, modeling of acoustic wave devices using the three-dimensional (3D) theory of anisotropic elasticity or piezoelectricity usually involves considerable mathematical difficulties. In sensor applications, this is further complicated by surface mass layers or fluid-structure

interaction. Although lengthy frequency equations for determining the wave dispersion relations can often be formally obtained, they are typically transcendental equations with multi-valued solutions and complex roots. Therefore a numerical search for the roots of the frequency equation is usually needed which still presents various challenges even with high speed computers. Sometimes roots are missing or false roots are found. Once the roots are numerically determined, it is often difficult to connect the data points for dispersion curves because of the presence of many branches of dispersion curves and it is not clear which roots are on the same branch. This is especially challenging in the useful high-frequency range when the roots and dispersion curves are crowded.

For the analysis of plate acoustic wave devices, researchers have developed two-dimensional (2D) equations for motions of elastic and piezoelectric plates [13,14,30-33]. These equations effectively reduce the dimension of the problem by one which is a major simplification. In addition, the plate equations usually are only involved with the particular operating mode of a device plus a few other modes that are coupled to the main mode of interest. Therefore mode identification when using the 2D equations is not as serious a problem as when using 3D equations. The 2D plate equations have made theoretical and numerical analysis possible in many practically useful cases [13-19,34-37].

1.5 Scope of the present research

In this dissertation we systematically study the useful and relatively less studied LFE sensors using both 2D and 3D equations. This includes pure TSh vibrations and the

propagation of FS waves and TT waves in unbounded plates. AT-cut quartz is considered among which the widely used crystals of quartz and the Langasite family are special cases. For LFE sensors without the fluid layers, exact solutions for resonant frequencies and modes in unbounded and bounded structures are obtained from the 2D equations in Chapter 2. Then, the effect of partial mass layers attached to the surfaces of crystal plates on vibration distribution are analyzed using 2D equations in Chapter 3. This effect is crucial to device mounting. Lateral field excitation (LFE) and thickness field excitation (TFE) are studied when the plates are driven by different electric fields and in contact with fluid layers in Chapter 4 and Chapter 5, respectively. The effects of piezoelectric coupling, fluid viscosity, fluid dielectric constants, and fluid density on wave frequencies are examined. This is also a necessary preparation for using the 2D equations to analyze more complicated problems in later chapters. Finally, Chapter 6 and Chapter 7 are on propagating waves in unbounded plates by 2D equations. Dispersion relations for coupled FS and TT waves are derived. Their long wave approximations are obtained. The results obtained in this dissertation are useful to the fundamental understanding and design optimization of plate acoustic wave resonators and sensors.

1.6 References

[1] R. D. Mindlin, "An Introduction to the Mathematical Theory of Vibrations of Elastic Plates," J. S. Yang, ed., World Scientific, 2006.

[2] J. S. Yang, "Analysis of Piezoelectric Devices," World Scientific, 2006,

[3] J. L. Bleustein, "A new surface wave in piezoelectric materials," Applied Physics Letters, 13, 412-413, 1968.

[4] Yu. V. Gulyaev, "Electroacoustic surface waves in solids," Soviet Physics JETP Letters, 9, 37-38, 1969.

[5] Bleustein, J.L., "Some simple modes of wave propagation in an infinite piezoelectric plate," Journal of Acoustical Society of Amermican. 45, 614-620, 1969.

[6] Schmidt, G.H., "On anti-symmetric waves in an unbounded piezoelectric plate with axisymmetric electrodes," International Journal of Solids and Structures 13, 179-195, 1977.

[7] Schmidt, G.H., "Resonances of an unbounded piezoelectric plate with circular electrodes." Paul, H.S., 1977.

[8] H. S. Paul, D. P. Raju and T. R. Balakrishnan, "Free vibrations of a piezoelectric layer of hexagonal (6mm) class" International Journal of Engineering Science. 15, 495-510, 1983.

[9] S. Syngellakis and P. C. Y. Lee, "Piezoelectric wave dispersion curves for infinite anisotropic plates," J. Appl. Phys., 73(11), 7152-7161, 1993.

[10] Stewart, J.T. and Yong, Y.K., "Exact analysis of the propagation of acoustic waves in multilayered anisotropic piezoelectric plates," IEEE Transactions on Ultrasonics, Ferroelectrics, and Frequency Control 40, 375-390, 1994.

[11] I. Koga, "Thickness vibrations of piezoelectric oscillating crystals," Physics, 3, 70-80, 1932.

[12] H. F. Tiersten, "Thickness vibrations of piezoelectric plates," J. Acoust. Soc. Am., 35, 53-58, 1963.

[13] R. D. Mindlin, "Thickness-shear and flexural vibrations of crystal plates," J. Appl. Phys., 22, 316-323, 1951.

[14] R. D. Mindlin, "Forced thickness-shear and flexural vibrations of piezoelectric crystal plates," J. Appl. Phys., 23, 83-88, 1952.

[15] R. D. Mindlin and P. C. Y. Lee, "Thickness-shear and flexural vibrations of partially plated, crystal plates, Int. J. Solids Structures," 2, 125-139, 1966.

[16] F. Shen, S. J. O'Shea, K. H. Lee, P. Lu and T. Y. Ng, "Frequency interference between two mesa-shaped quartz crystal microbalance," IEEE Trans. Ultrason., Ferroelect., Freq. Contr., 51(2), 249-253, 2004.

[17] F. Shen, K. H. Lee, S. J. O'Shea, P. Lu and T. Y. Ng, "Frequency interference between two quartz crystal microbalances," IEEE Sensors Journal, 3(3), 274-281, 2003.

[18] F. Shen and P. Lu, "Influence of interchannel spacing on the dynamical properties of multichannel quartz crystal microbalance," IEEE Trans. Ultrason., Ferroelect., Freq. Contr., 50(6), 668-675, 2003.

[19] J. Wang and J. S. Yang, "Higher-order theories of piezoelectric plates and applications," Applied Mechanics Reviews, 53, 87-99, 2000.

[20] R. D. Mindlin, "On thickness twist vibrations of a quartz strip, Some Aspects of Mechanics of Continua," B. Sen Memorial Volume, Department of Mathematics, Jadavpur University, Calcuta, Part I, 1977, 29-31.

[21] J. Bleustein, "Thickness-twist and face-shear vibrations of a contoured crystal plate," Int. J. of Solids Structures, 2, 351-360, 1966.

[22] C. B. Loutzenheiser and W. J. Denkmann, "Thickness/twist vibrations of truncated, linearly tapered, crystal strip," J. Acoust. Soc. Am., 41, 962-968, 1967.

[23] G. T. Pearman, "Thickness-twist vibrations in beveled AT-cut quartz plates," J. Acoust. Soc. Am., 45, 928-934, 1969.

[24] Z. T. Yang, Y. T. Hu and J. S. Yang, "Effect of mass layer stiffness on propagation of thickness-twist waves in rotated Y-cut quartz crystal plates," Ultrasonics, 49, 401-403, 2009.

[25] J. S. Yang and S. H. Guo, "Effects of piezoelectric coupling on Bechmann's number for thickness-twist waves in a plate of hexagonal crystals," IEEE Trans. Ultrason., Ferroelect., Freq. Contr., 53, 1960-1962, 2006.

[26] Y. H. Hu, L. A. French, Jr., K. Radecsky, M. P. da Gunha, P. Millard and J. F. Vetelino, "A lateral field excited liquid acoustic wave sensor," IEEE Trans. Ultrason., Ferroelec., Freq. Contr., 51(11), 1373-1380, 2004.

[27] U. Hempel, R. Lucklum, P. R. Hauptmann, E. P. EerNisse, D. Puccio and R. Fernandez Diaz, "Quartz crystal resonator sensors under lateral field excitation—a theoretical and experimental analysis," Meas. Sci. Technol. 19 055201, 2008

[28] U. Hempel, R. Lucklum, J. F. Vetelino, P. Hauptmann, "Advanced application of the impedance spectrum of a lateral field excited sensor," Sensors and Actuators A 142, 97–103, 2008.

[29] D. F. McCann, J. M. McCann, J. M. Parks, D. J. Frankel, M. P. da Cunha, and J. F. Vetelino, "A lateral-field-excited $LiTaO_3$ high-frequency bulk acoustic wave sensor," IEEE Trans. Ultrason., Ferroelec., Freq. Contr., 56(4), 779-787, 2009.

[30] R. D. Mindlin, "High frequency vibrations of crystal plates," Quart. Appl. Math. 19, 51-61, 1961.

[31] H. F. Tiersten, R. D. Mindlin, "Forced vibrations of piezoelectric crystal plates," Quart. Appl. Math. 20, 107-119, 1962.

[32] R. D. Mindlin, "High frequency vibrations of piezoelectric crystal plates," Int. J. Solids Structures, 8 (7), 895-906, 1972.

[33] P. C. Y. Lee, S. Syngellakis, J. P. Hou, "A two-dimensional theory for high-frequency vibrations of piezoelectric crystal plates with or without electrodes," J. Appl. Phys. 61 (4), 1249-1262, 1987.

[34] J. Wang, P. C. Y. Lee, D. H. Bailey, "Thickness-shear and flexural vibrations of linearly contoured crystal strips with multiprecision computation," Computers & Structures, 70 (4), 437-445, 1999.

[35] J. Wang, W. H. Zhao, "The determination of the optimal length of crystal blanks in quartz crystal resonators," IEEE Trans. Ultrason., Ferroelec., Freq. Contr. 52 (11), 2023-2030, 2005.

[36] Y.-K. Yong, J. T. Stewart, "Mass-frequency influence surface, mode shapes, and frequency spectrum of a rectangular AT-cut quartz plate," IEEE Trans. Ultrason., Ferroelec., Freq. Contr. 38 (1), 67-73, 1991.

[37] J. N. Wang, Y. T. Hu and J. S. Yang, "Frequency spectra of at-cut quartz plates with electrodes of unequal thickness," IEEE Trans. Ultrason., Ferroelect., Freq. Contr., 57 (5), 1146-1151, 2010.

2. Vibrations of Piezoelectric Plates of AT-cut Quartz under Lateral Field Excitation

2.1 Introduction

Piezoelectric crystals are widely used to make resonators for time-keeping, frequency generation and operation, telecommunication, and sensing. Quartz is the most widely used crystal for resonator applications. Recently new crystals of the langasite family have shown great promise as materials for future resonators. A large portion of piezoelectric resonators operate with shear vibration modes of a plate. These modes can be excited either by a thickness electric field (Thickness field excitation or TFE) or by a lateral electric field (LFE). While there seem to be more resonators with TFE than LFE, LFE offers a number of advantages over TFE [1, 2]. For example, LFE can result in reduced aging, higher *Q* values and increased frequency stability because the regions of greatest vibrational motion are free of electrodes. This also makes LFE convenient for sensor applications. So far, several LFE resonators used as liquid sensor have been reported [3-6].

TFE resonators have been under sustained study theoretically, numerically, and experimentally. In particular, in a series of papers [7-10], Mindlin and his coworkers developed and refined the two-dimensional equations for motions of piezoelectric plates. These equations have been used in many analyses theoretically and numerically, e.g., [11-15], on TFE resonators. More references can be found in a review article [16]. In contrast, for LFE resonators, reported studies are much fewer. For example, energy

trapping was recently studied experimentally in [17]. Theoretical results are few and scattered. Electromechanical coupling coefficient was discussed in [18]. Electromagnetic radiation was calculated in [19]. The few and scattered theoretical results are significant limitations of designing a LFE resonator. In fact, Mindlin's first-order plate theory is as effective in LFE as in TFE, but it has rarely been used for LFE. In this chapter we use Mindlin's first-order plate theory to study systematically coupled face-shear (FS) and thickness-twist (TT) vibrations of piezoelectric plates of At-cut quartz under lateral field excitation. Both free and forced vibrations are studied. Important vibration characteristics including dispersion relations, frequency spectra, and motional capacitance are obtained.

2.2 Plate equations for lateral field excitation

Consider a thin plate as shown in Fig. 2.1. The plate normal is along the x_2 axis. The x_1 and x_3 axes are in the middle plane of the plate. The plate is electroded at the two end faces at $x_3 = \pm c$ which may be under a driving voltage $2V$. For free vibrations the driving voltage is zero or the two electrodes are shorted.

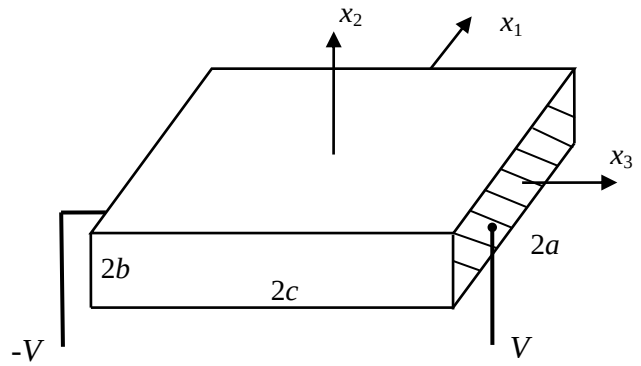

Fig. 2.1 A piezoelectric plate and coordinate system

We consider the so-called straight-crested waves without x_1 dependence in a plate with $2a= \infty$ in Fig. 2.1. In this case $u_2 = u_3 = 0$ [20]. There is only one displacement component u_1. The relevant equations in [9] reduce to the following equations of motion and electrostatics:

$$T_{31,3}^{(0)} = 2b\rho\ddot{u}_1^{(0)}, \tag{2-1a}$$

$$T_{3\,1,3}^{(1)} - T_{2\,1}^{(0)} = \frac{2b^3}{3}\rho\ddot{u}_1^{(1)}, \tag{2-1b}$$

$$D_{3,3}^{(0)} = 0, \tag{2-1c}$$

$$D_{3,3}^{(1)} - D_2^{(0)} = 0, \tag{2-1d}$$

where $u_1^{(0)}(x_3,t)$ is the FS displacement, and $u_1^{(1)}(x_3,t)$ is the TT displacement. They are related to u_1 through $u_1 = u_1^{(0)} + x_2 u_1^{(1)}$. The mechanical and electric resultants in (2-1) are related to the plate displacements $u_1^{(0)}$ and $u_1^{(1)}$ as well as electric potentials $\phi^{(0)}$ and $\phi^{(1)}$ by the following constitutive relations:

$$T_{31}^{(0)} = 2b(c_{55}u_{1,3}^{(0)} + \kappa_1 c_{56}u_1^{(1)} + e_{25}\phi^{(1)} + e_{35}\phi_{,3}^{(0)}), \tag{2-2a}$$

$$T_{12}^{(0)} = 2b(\kappa_1 c_{56}u_{1,3}^{(0)} + \kappa_1^2 c_{66}u_1^{(1)} + \kappa_1 e_{26}\phi^{(1)} + \kappa_1 e_{36}\phi_{,3}^{(1)}), \tag{2-2b}$$

$$T_{31}^{(1)} = \frac{2b^3}{3}(\gamma_{55}u_{1,3}^{(1)} + \psi_{35}\phi_{,3}^{(1)}), \tag{2-2c}$$

$$D_2^{(0)} = 2b(e_{25}u_{1,3}^{(0)} + \kappa_1 e_{26}u_1^{(1)} - \varepsilon_{22}\phi^{(1)} - \varepsilon_{23}\phi_{,3}^{(1)}), \tag{2-2d}$$

$$D_3^{(0)} = 2b(e_{35}u_{1,3}^{(0)} + \kappa_1 e_{36}u_1^{(1)} - \varepsilon_{23}\phi^{(1)} - \varepsilon_{33}\phi_{,3}^{(0)}), \tag{2-2e}$$

$$D_3^{(1)} = \frac{2b^3}{3}(\psi_{35}u_{1,3}^{(1)} - \zeta_{33}\phi_{,3}^{(1)}). \tag{2-2f}$$

$\phi^{(0)}$ and $\phi^{(1)}$ are related to the potential ϕ through $\phi = \phi^{(0)} + x_2\phi^{(1)}$. In (2-2), $c_{pq}(=c_{pq}^E)$, e_{ip}, and $\varepsilon_{ij}(=\varepsilon_{ij}^S)$ are the usual elastic stiffness, piezoelectric constants, and dielectric constants. The other material constants in (2-2) are defined by

$$\begin{aligned} &\gamma_{55} = 1/s_{55}, \quad \psi_{35} = e_{35} - e_{36}c_{56}/c_{66} = d_{35}\gamma_{55}, \\ &\zeta_{33} = \varepsilon_{33} + e_{36}^2/c_{66}, \end{aligned} \tag{2-3}$$

where $s_{pq}(=s_{pq}^E)$ is the elastic compliance and d_{ip} is another set of piezoelectric constants different from but related to e_{ip}. For a plate unelectroded at the major surfaces at $x_2 = \pm b$, the shear correction factors κ_1 in the above equations are given by [9]

$$\kappa_1^2 = \frac{\pi^2}{12}. \tag{2-4}$$

Substitution of (2-2) into (2-1) gives four equations for the plate displacements and potentials:

$$c_{55}u_{1,33}^{(0)} + e_{35}\phi_{,33}^{(0)} + \kappa_1 c_{56}u_{1,3}^{(1)} + e_{25}\phi_{,3}^{(1)} = \rho\ddot{u}_1^{(0)}, \tag{2-5a}$$

$$\gamma_{55}u_{1,33}^{(1)} + \psi_{35}\phi_{,33}^{(1)} - 3b^{-2}(\kappa_1 c_{56}u_{1,3}^{(0)} + \kappa_1^2 c_{66}u_1^{(1)} + \kappa_1 e_{26}\phi^{(1)} + \kappa_1 e_{36}\phi_{,3}^{(0)}) = \rho\ddot{u}_1^{(1)}, \tag{2-5b}$$

$$e_{35}u_{1,33}^{(0)} + \kappa_1 e_{36}u_{1,3}^{(1)} - \varepsilon_{33}\phi_{,33}^{(0)} - \varepsilon_{23}\phi_{,3}^{(1)} = 0, \tag{2-5c}$$

$$\psi_{35}u_{1,33}^{(1)} - \zeta_{33}\phi_{,33}^{(1)} - 3b^{-2}(e_{25}u_{1,3}^{(0)} + \kappa_1 e_{26}u_1^{(1)} - \varepsilon_{22}\phi^{(1)} - \varepsilon_{23}\phi_{,3}^{(0)}) = 0. \tag{2-5d}$$

2.3 Thickness vibration

First we study pure thickness modes independent of x_3 which are the ideal operating modes of devices. For LFE the motion is driven by

$$\phi_{,3}^{(0)} = -E\exp(i\omega t)\,, \tag{2-6}$$

where $E = -2V/(2c)$. E is the applied field and $2V$ is the applied voltage. In this case $\phi^{(0)}$ in linear in x_3 but $\phi_{,3}^{(0)}$ is no more than a function of time. Then (2-5a) and (2-5c) imply that $u_1^{(0)} = 0$, $\phi_{,3}^{(1)} = 0$. (2-5b) and (2-5d) become

$$-3b^{-2}(\kappa_1^2 c_{66} u_1^{(1)} + \kappa_1 e_{26}\phi^{(1)} + \kappa_1 e_{36}\phi_{,3}^{(0)}) = \rho\ddot{u}_1^{(1)}, \tag{2-7a}$$

$$\kappa_1 e_{26} u_1^{(1)} - \varepsilon_{22}\phi^{(1)} - \varepsilon_{23}\phi_{,3}^{(0)} = 0. \tag{2-7b}$$

Solving (2-7), we obtain

$$u_1^{(1)} = -AE\exp(i\omega t), \quad \phi^{(1)} = -BE\exp(i\omega t)\,, \tag{2-8}$$

where

$$\begin{aligned} A &= -\frac{\varepsilon_{22}\kappa_1 e_{36} - \varepsilon_{23}\kappa_1 e_{26}}{\kappa_1^2\varepsilon_{22}c_{66} + \kappa_1^2 e_{26}^2 - \dfrac{b^2}{3}\rho\omega^2\varepsilon_{22}}, \\ B &= -\left(\frac{\varepsilon_{23}}{\varepsilon_{22}} - \frac{\kappa_1^2\varepsilon_{22}e_{26}e_{36} - \kappa_1^2\varepsilon_{23}e_{26}^2}{\kappa_1^2\varepsilon_{22}^2 c_{66} + \kappa_1^2\varepsilon_{22}e_{26}^2 - \dfrac{b^2}{3}\rho\omega^2\varepsilon_{22}^2}\right). \end{aligned} \tag{2-9}$$

When the denominator of A vanishes, we have the frequency equation that determines the free-vibration resonant frequency of the fundamental TT mode. Since the first-order plate theory is used, the only resonant frequency is found to be

$$\omega_0^2 = \frac{3\kappa_1^2}{\rho b^2}(c_{66} + e_{26}^2/\varepsilon_{22}) = \frac{\pi^2}{4\rho b^2}(c_{66} + e_{26}^2/\varepsilon_{22})\,. \tag{2-10}$$

Resonators are used as circuit elements. Two basic properties of a resonator, its resonant frequency and capacitance, are of primary interest for circuit analysis. The capacitance of a resonator can only be obtained from an electrically forced vibration analysis. The capacitance of a piezoelectric resonator is called the motional capacitance because mechanical vibration of the resonator is involved through piezoelectric coupling. Recently there has been growing interest in forced vibration analysis of piezoelectric resonators and the computation of the motional capacitance [19-21]. To calculate the motional capacitance, from (2-2f) and (2-2e) we find that $D_3^{(1)}$ =0 and

$$D_3^{(0)} = -2b(\kappa_1 e_{36} A - \varepsilon_{23} B - \varepsilon_{33}) E \,. \tag{2-11}$$

Then the charge on the electrode at $x_3 = c$ per unit length along x_1 ($2a$=1 in Fig. 2.1) is given by

$$Q_e = -D_3^{(0)} = -2b(\kappa_1 e_{36} A - \varepsilon_{23} B - \varepsilon_{33}) \frac{V}{c} \,. \tag{2-12}$$

Hence the frequency-dependent capacitance is determined as

$$\begin{aligned} C &= \frac{Q_e}{2V} = (1 - \kappa_1 \frac{e_{36}}{\varepsilon_{33}} A + \frac{\varepsilon_{23}}{\varepsilon_{33}} B) C_0, \\ C_0 &= \frac{\varepsilon_{33} b}{c}. \end{aligned} \tag{2-13}$$

For later use we introduce a normalized driving frequency by

$$\Omega = \frac{\omega}{\omega_0} \,. \tag{2-14}$$

As a numerical example b=1mm is used. Damping is introduced by allowing the elastic constants to assume complex values, which can represent viscous damping. In our calculations, c_{pq} is replaced by $c_{pq}(1+iQ^{-1})$ where Q is a real, large and positive number. For quartz, Q is of the order of 10^5. We use Q=10^4 or smaller which is relatively low and represents relatively high damping for quartz. It is considered to be a single damping parameter representing all of the damping of the resonator. Note that the ω_0 in (2-14) is kept real.

In Fig. 2.2 we plot $|C/C_0|$ versus Ω for AT-cut quartz. $|C/C_0|$ is large near Ω=1, the only resonant frequency. For smaller values of Q or larger damping, the peaks are lower.

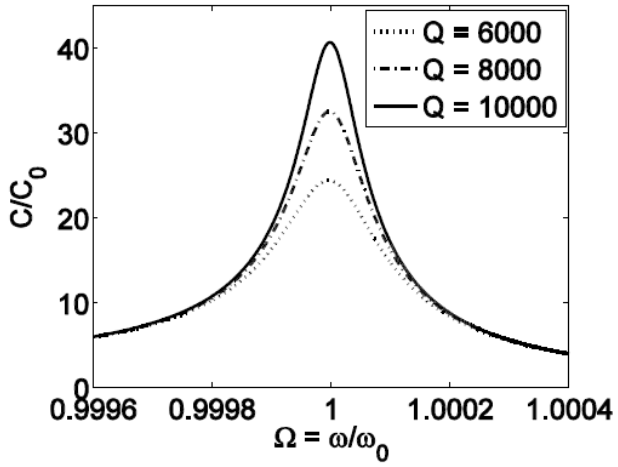

Fig. 2.2 Capacitance versus driving frequency for pure thickness modes.

2.4 Dispersion of strait-crest waves in unbounded plates

Next we study wave propagation in unbounded plates ($2c=\infty$). Let

$$\begin{aligned} u_1^{(0)} &= A_1 \cos(\zeta x_3 - \omega t), \quad u_1^{(1)} = A_2 \sin(\zeta x_3 - \omega t), \\ \phi^{(0)} &= A_3 \cos(\zeta x_3 - \omega t), \quad \phi^{(1)} = A_4 \sin(\zeta x_3 - \omega t), \end{aligned} \tag{2-15}$$

where A_1-A_4 un undetermined constants, ζ is wave number, and ω is frequency. (2-15) represents waves propagating in the x_3 direction. They are called straight-crested waves because there is no x_1 dependence. Substitution of (2-15) into (2-5) results in four linear, homogeneous equations for A_1-A_4. For nontrivial solutions the determinant of the coefficient matrix has to vanish, which yields an equation that determines ω versus ζ, or the dispersion relation. It is a quadratic equation for ω^2, which is too long to be presented here. For a given ζ, there are two roots for ω^2. For each root of ω^2, the two corresponding values of ω only differ by a sign and examining one of them is sufficient. When ζ is real or pure imaginary, the results are shown in Fig. 2.3 in which the dimensionless wave number is defined by

$$Z = \zeta \Big/ \frac{\pi}{2b} . \tag{2-16}$$

The curve for FS waves looks linear and therefore has little dispersion. The curve for TT waves is curved and is clearly dispersive. The curve for TT waves has a finite intercept with the Ω axis which is the cutoff frequency of the waves below which the waves cannot propagate. There are two vertical lines. One is at Re(Z)=0. The other is at Im(Z)

slightly larger than 1. These two vertical lines are due to the equations of electrostatics in (2-5c) and (2-5d). If we neglect piezoelectric coupling and drop (2-5c) and (2-5d), these two vertical lines will disappear.

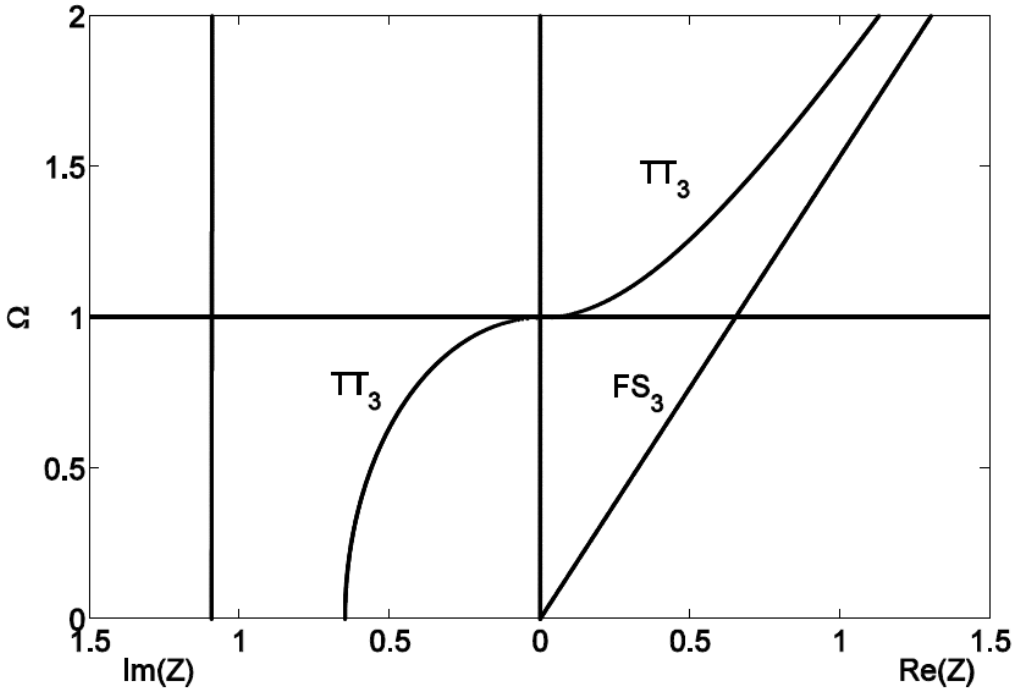

Fig. 2.3 Dispersion curves of straight-crested waves.

2.5 Frequency spectra of finite plates

In this section we study free vibrations of a plate finite in the x_3 direction with $|x_3|<c$. The governing equations are in (2-5). Let the edges at $x_3=\pm c$ be free and electroded, with the electrodes shorted. The boundary conditions are

$$T_{31}^{(0)}=0,\quad T_{31}^{(1)}=0,\quad \phi^{(0)}=0,\quad \phi^{(1)}=0,\quad x_3=\pm c. \tag{2-17}$$

Different from the propagating waves in (2-15), we consider stationary waves in the form of

$$\begin{aligned} u_1^{(0)} &= A_1\sin(\zeta x_3)\exp(i\omega t),\quad u_1^{(1)} = A_2\cos(\zeta x_3)\exp(i\omega t),\\ \phi^{(0)} &= A_3\sin(\zeta x_3)\exp(i\omega t),\quad \phi^{(1)} = A_4\cos(\zeta x_3)\exp(i\omega t), \end{aligned} \tag{2-18}$$

which may be called symmetric modes because the main displacement of interest, $u_1^{(1)}$, is an even function of x_3. There are also modes with $u_1^{(1)}$ being an odd function of x_3 which may be called antisymmetric modes. Antisymmetric modes are of less interest because they cannot be excited by a lateral electric field, and therefore will not be studied in this chapter.

Substitution of (2-18) into (2-5) results in four linear equations for A_1-A_4. For nontrivial solutions the determinant of the coefficient has to vanish, which yields a polynomial equation of degree four for ζ^2. There are four roots which are denoted by $(\zeta^{(m)})^2$, with m=1-4. Corresponding to a typical $\zeta^{(m)}$, let the eigenvector be $\beta_p^{(m)}$ with p=1-4. $\beta_p^{(m)}$ determines the ratios among A_1-A_4. It turns out that one of the roots for $(\zeta^{(m)})^2$ is zero. Therefore the general symmetric solution can be constructed as

$$\begin{Bmatrix} u_1^{(0)}\\ u_1^{(1)}\\ \phi^{(0)}\\ \phi^{(1)} \end{Bmatrix} = \sum_{m=1}^{3} C^{(m)} \begin{Bmatrix} \beta_1^{(m)}\sin(\zeta^{(m)}x_3)\\ \beta_2^{(m)}\cos(\zeta^{(m)}x_3)\\ \beta_3^{(m)}\sin(\zeta^{(m)}x_3)\\ \beta_4^{(m)}\cos(\zeta^{(m)}x_3) \end{Bmatrix} + C^{(4)} \begin{Bmatrix} 0\\ A\\ x_3\\ B \end{Bmatrix}. \tag{2-19}$$

When (2-19) is substituted into the boundary conditions in (2-17) at x_3=c, we obtain four linear, homogeneous equations for $C^{(m)}$. For nontrivial solutions, the determinant of the coefficient matrix has to vanish which yields the frequency equation for determining ω.

Frequency spectra are relations of frequency versus the length/thickness ratio *c/b* of the plate. They are very useful in design when determining the dimensions of plate resonators. We plot the frequency spectra determined from (2-19) and (2-17) in Fig. 2.4 (c). For comparison, two special cases are also shown in Figs. 2.4 (a) and (b). The curves in Fig. 2.4 are in fact formed by data points without connecting them. Each data point represents the frequency of a mode. Corresponding to a particular value of *c/b*, there are infinitely many modes. A few can be seen in the frequency range shown. In Fig. 2.4 (a), the piezoelectric coupling, the electric potentials, and the elastic coupling due to the relatively small elastic constant c_{56} are all neglected. In this case (2-5a) and (2-5b) become two uncoupled equations for $u_1^{(0)}$ and $u_1^{(1)}$. The two families of curves in Fig. 2.4 (a) intersect with each other. The relatively flat curves are for TT modes with $u_1^{(1)}$. In Fig. 2.4 (b) the elastic coupling due to c_{56} is considered but the piezoelectric coupling is ignored. This has such an effect on the curves in Fig. 2.4 (b) that, near the intersections in Fig. 2.4 (a), the curves in Fig. 2.4 (b) turn away from each other (mode veering). This is qualitatively different from Fig. 2.4 (a). Fig. 2.4 (c) has the effects of both piezoelectric couplings to $\phi^{(0)}$ and $\phi^{(1)}$, as well as the relatively small elastic coupling due to c_{56}. Qualitatively the curves are similar to those in Fig. 2.4 (b), with small, quantitative differences. The usefulness of the frequency spectra is that it is needed for determining

c/b. For example, for the lowest TT branch with Ω close to 1, those values of *c/b* that are close to the intersections with the FS curves need to be avoided.

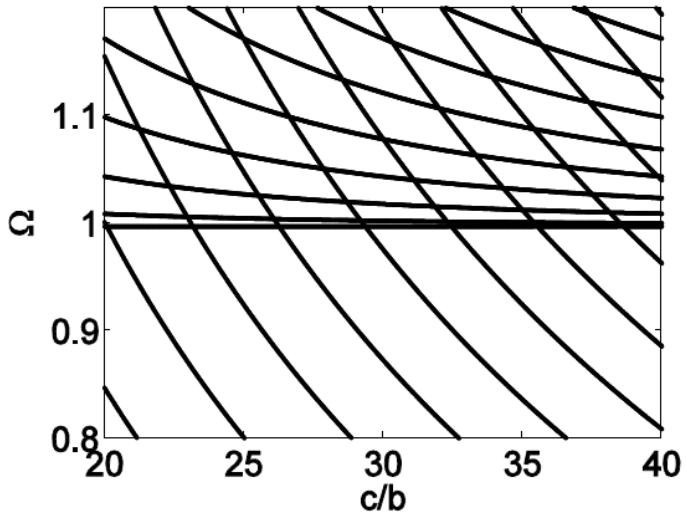

(a)

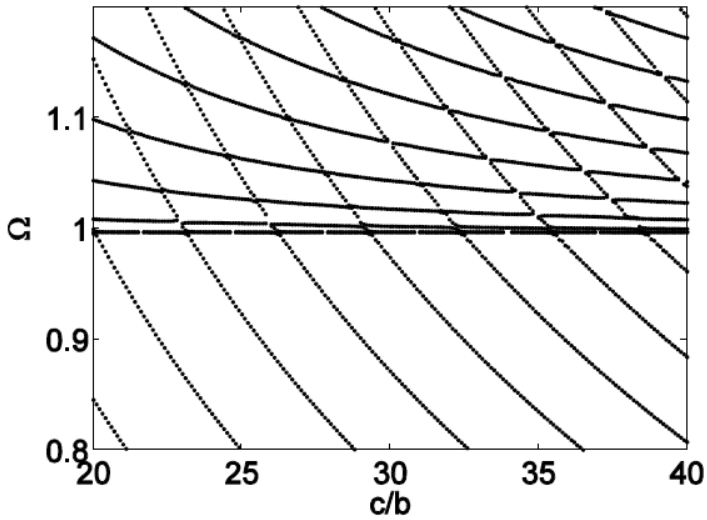

(b)

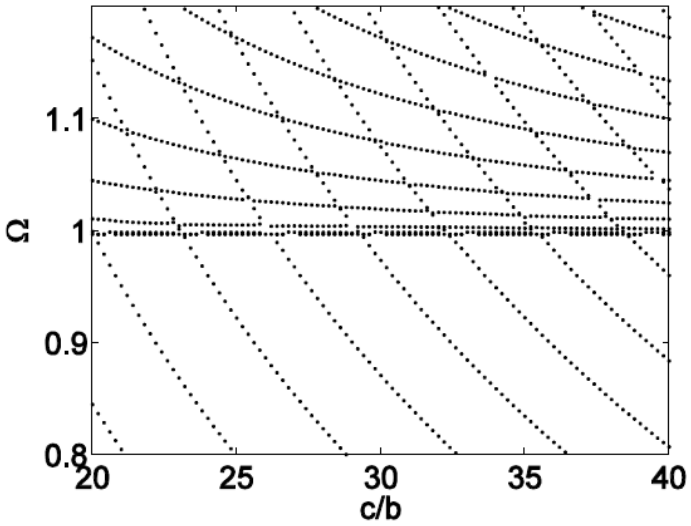

(c)

Fig. 2.4 Frequency spectra of symmetric modes. (a) Uncoupled elastic modes ($\phi^{(0)}=0$, $\phi^{(1)}=0$, c_{56}=0). (b) Coupled elastic modes ($\phi^{(0)}=0$, $\phi^{(1)}=0$, $c_{56}\neq 0$). (c) Coupled piezoelectric modes ($\phi^{(0)}\neq 0$, $\phi^{(1)}\neq 0$, $c_{56}\neq 0$).

2.6 Motional capacitance

Finally, we calculate the motional capacitance of a finite plate with $|x_3|<c$. Consider electrically forced vibrations with the following boundary conditions:

$$T_{31}^{(0)}=0,\quad T_{31}^{(1)}=0,\quad \phi^{(0)}=\pm V\exp(i\omega t),\quad \phi^{(1)}=0,\quad x_3=\pm c. \tag{2-20}$$

Substituting (2-19) into (2-20), we obtain four linear, inhomogeneous equations for $C^{(m)}$, driven by *V*. Once these equations are solved, the plate displacements and potentials are known. Then the charge and capacitance can be calculated from

$$Q_e = -D_3^{(0)}(x_3 = c), \quad C = \frac{Q_e}{2V}. \tag{2-21}$$

Fig. 2.5 shows $|C/C_0|$ versus Ω for AT-cut quartz. Similar to Fig. 2.2 for the pure thickness mode of $u_1^{(1)}$, $|C/C_0|$ is large near $\Omega=1$. However, due to the dependence on x_3 and the coupling to $u_1^{(0)}$, there are quite a few resonances in the frequency range shown. Even in the neighborhood of $\Omega=1$, there are in fact two peaks. The maxima of the two high peaks near $\Omega=1$ are not fully shown in order to see the lower peaks.

We plot $|C/C_0|$ in a narrower frequency range near $\Omega=1$ in Fig. 2.6, showing two resonances. The maximum of the left peak near $\Omega=1$ is slightly higher than that in Fig. 2.2. For finite plates the coupling to $u_1^{(0)}$ affects the charge on the electrodes through (2-2e) and (2-21) and hence affects the capacitance.

In Fig. 2.7 we vary the aspect ratio slightly around *c/b*=21.5 which is right in the middle of a flat potion of the lowest TT curve in Fig. 2.4 (c) which represents $u_1^{(1)}$ dominated modes. *c/b*=20.5 and 22.5 are also well within the same flat portion and are also $u_1^{(1)}$ dominated. We note that C_0 depends on *c/b* (2-13) and therefore the difference in the height of the peaks in Fig. 2.7 is exaggerated. When *c/b* varies slightly in Fig. 2.7, the two peaks on a curve in Fig. 2.7 move in opposite directions. This is a relatively more complicated behavior and is not uncommon when there are two coupled modes [22].

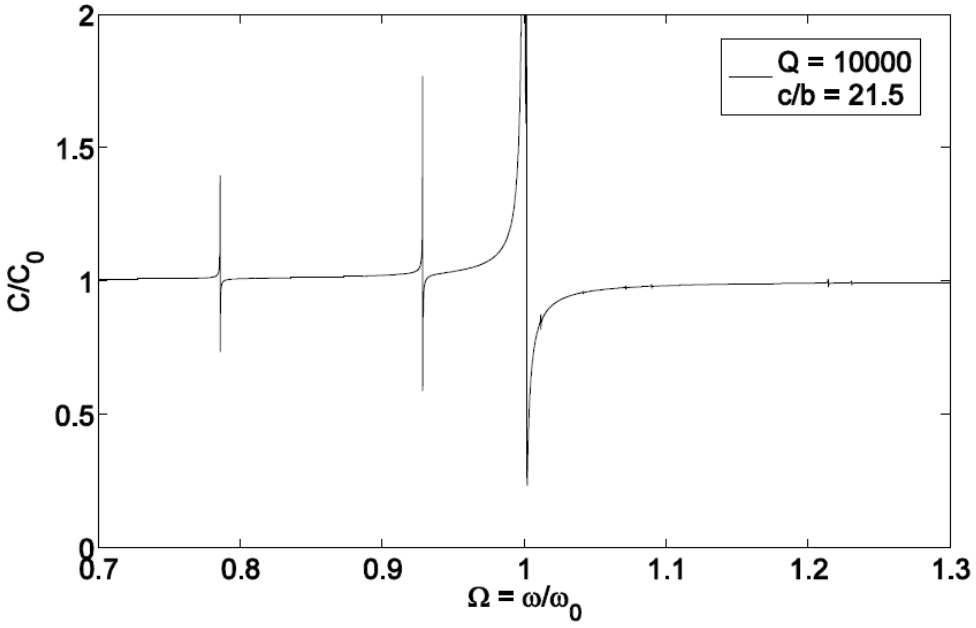

Fig. 2.5 Motional capacitance versus driving frequency (*b*=1mm).

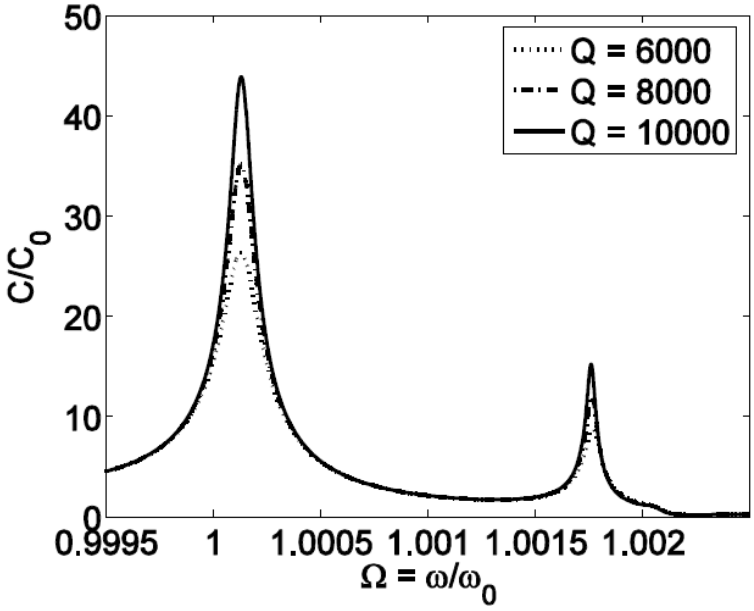

Fig. 2.6 Motional capacitance versus driving frequency for different *Q* (*b*=1mm, *c/b*=21.5).

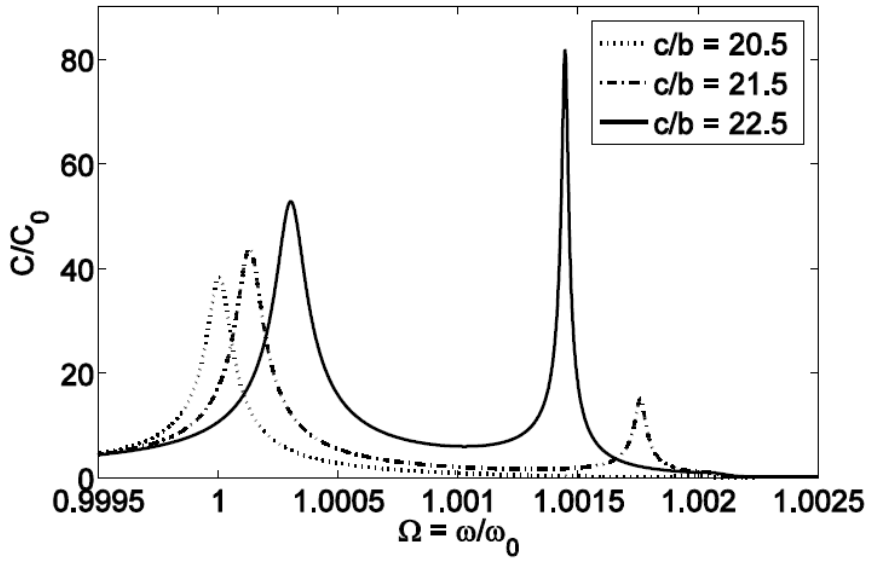

Fig. 2.7 Motional capacitance versus driving frequency for different *c/b* (*b*=1mm, *Q*=10000).

2.7 Conclusion

When an At-cut quartz plate is under LFE, the dominating displacements are FS and TT. Within the first-order plate theory, there is only one resonance for pure thickness vibration. For straight-crested waves, the two electrostatic equations contribute to two branches in the dispersion relations, in addition to the two branches for FS and TT waves. Frequency spectra of finite plates consists of the "sum" of those of FS and TT modes with mode veering at the intersections. To avoid strong couplings between FS and TT, certain values of the plate length/thickness ratio should be avoided. Mindlin's first-order plate theory is effective in analyzing vibrations of crystal plates under LFE.

2.8 References

[1] A. Ballato, E. R. Hatch, M. Mizan and T. L. Lukaszek, "Lateral field equivalent networks and piezocoupling factors of quartz plates driven in simple thickness modes," IEEE Trans. Ultrason., Ferroelec., Freq. Contr., 49(7), 922-928, 2002.

[2] A. Khan and A. Ballato, "Piezoelectric coupling factor calculations for plates of langatate driven in simple thickness modes by lateral-field-excitation," IEEE Trans. Ultrason., Ferroelec., Freq. Contr., 35(3), 435-436, 1988.

[3] Y. H. Hu, L. A. French, Jr., K. Radecsky, M. P. da Gunha, P. Millard and J. F. Vetelino, "A lateral field excited liquid acoustic wave sensor," IEEE Trans. Ultrason., Ferroelec., Freq. Contr., 51(11), 1373-1380, 2004.

[4] U. Hempel, R. Lucklum, P. R. Hauptmann, E. P. EerNisse, D. Puccio and R. Fernandez Diaz, "Quartz crystal resonator sensors under lateral field excitation—a theoretical and experimental analysis," Meas. Sci. Technol. 19 055201, 2008

[5] U. Hempel, R. Lucklum, J. F. Vetelino, P. Hauptmann, "Advanced application of the impedance spectrum of a lateral field excited sensor," Sensors and Actuators A 142, 97–103, 2008.

[6] D. F. McCann, J. M. McCann, J. M. Parks, D. J. Frankel, M. P. da Cunha, and J. F. Vetelino, "A lateral-field-excited $LiTaO_3$ high-frequency bulk acoustic wave sensor," IEEE Trans. Ultrason., Ferroelec., Freq. Contr., 56(4), 779-787, 2009.

[7] R. D. Mindlin, "High frequency vibrations of crystal plates," Quart. Appl. Math. 19, 51-61, 1961.

[8] H. F. Tiersten, R. D. Mindlin, "Forced vibrations of piezoelectric crystal plates," Quart. Appl. Math. 20, 107-119, 1962.

[9] R. D. Mindlin, "High frequency vibrations of piezoelectric crystal plates," Int. J. Solids Structures, 8 (2-7), 895-906, 1972.

[10] P. C. Y. Lee, S. Syngellakis, J. P. Hou, "A two-dimensional theory for high-frequency vibrations of piezoelectric crystal plates with or without electrodes," J. Appl. Phys. 61 (2-4), 1249-1262, 1987.

[11] R. D. Mindlin and P. C. Y. Lee, "Thickness-shear and flexural vibrations of partially plated, crystal plates," Int. J. Solids Structures, 2, 125-139, 1966.

[12] J. Wang, P. C. Y. Lee, D. H. Bailey, Thickness-shear and flexural vibrations of linearly contoured crystal strips with multiprecision computation, Computers & Structures 70 (2-4) (2-1999) 437-445.

[13] J. Wang, W. H. Zhao, "The determination of the optimal length of crystal blanks in quartz crystal resonators," IEEE Trans. Ultrason., Ferroelec., Freq. Contr. 52 (2-11), 2023-2030, 2005.

[14] Y.-K. Yong, J. T. Stewart, "Mass-frequency influence surface, mode shapes, and frequency spectrum of a rectangular AT-cut quartz plate," IEEE Trans. Ultrason., Ferroelec., Freq. Contr. 38 (2-1), 67-73, 1991.

[15] P. C. Y. Lee and M. S. H. Tang, "Initial stress field and resonance frequencies of incremental vibrations in crystal resonators by finite element method," in: *Proc. of the 40th Annual Freq Contr Symp*, 152-160, 1986.

[16] J. Wang and J. S. Yang, "Higher-order theories of piezoelectric plates and applications," Applied Mechanics Reviews, 53, 87-99, 2000.

[17] W. Y. Wang, C. Zhang, Z. T. Zhang, T. F. Ma and G. P. Feng, "Energy-trapping mode in lateral-field-excited acoustic wave devices," Appl. Phys. Lett., 94, Art. No. 192901, 2009.

[18] R. C. Smythe and H. F. Tiersten, "An approximate expression for the motional capacitance of a lateral field resonator," IEEE Trans. Ultrason., Ferroelec., Freq. Contr., 35(3), 435-436, 1988.

[19] P. C. Y. Lee, "Electromagnetic-radiation from an at-cut quartz plate under lateral-field excitation," J. Appl. Phys., 65(4), 1395-1399**,** 1989

[20] R. D. Mindlin and W. J. Spencer, "Anharmonic, thickness-twist overtones of thickness-shear and flexural vibrations of rectangular, AT-cut quartz plates," J. Acoust. Soc. Am., 42(6), 1268-1277, 1967.

[21] J. Wang, W. H. Zhao and J. K. Du, "The determination of electrical parameters of quartz crystal resonators with the consideration of dissipation," Ultrasonics, 44, 869-873, 2006

[22] J. S. Yang and H. Y. Fang, "Analysis of a rotating elastic beam with piezoelectric films as an angular rate sensor," IEEE Trans. Ultrason., Ferroelect., Freq. Contr., 49(6), 798-804, 2002.

3. Energy Trapping in High-Frequency Vibrations of Piezoelectric Plates with Partial Mass Layers under Lateral Electric Field Excitation

3.1 Introduction

An important situation in resonator and sensor application is when the plate is partially covered by additional mass layers which can be either due to the accumulation of another material like in mass sensor applications or due to the inertia of electrodes [1-6]. The inertia of the mass layers is responsible for an important phenomenon called energy trapping in which the vibration is confined under the mass layers and decays rapidly outside them. Energy trapping is crucial to resonator mounting and has been the subject of many studies, mostly for TFE. For LFE, however, our understanding on energy trapping is limited. Further analysis is needed to understand the effect of mass layers on resonators under LFE, and the energy trapping in them in particular.

In this chapter we use Mindlin's first-order plate theory to study theoretically forced FS and TT motions of a piezoelectric plate with partial mass layers under a lateral electric field. An AT-cut quartz plate is used as an example for presenting numerical results. In addition to the motional capacitance of the plate which is important when the plate is used as a resonator, energy trapping and the relationship between the dimension of the mass layers and the number of trapped modes is also examined.

3.2 Structure

Consider a thin crystal plate of thickness 2*b* as shown in Fig. 3.1. The plate normal is along the x_2 axis. The x_1 and x_3 axes are in the middle plane of the plate. The central part of the plate where $|x_3|<c$ is symmetrically covered with identical, dielectric mass layers of thickness $2b'$ and density ρ'. The plate is electroded at the two end faces at $x_3=\pm L$, with the electrodes shown by the thick lines. A time-harmonic driving voltage $\pm V\exp(i\omega t)$ is applied across the electrodes. Under such a driving voltage, due to the particular anisotropy of monoclinic crystals, the plate can be excited into motions called straight-crested waves with one displacement component only, i.e., $u_1=u_1(x_2,x_3,t)$ and $u_2=u_3=0$, which is coupled to an electric potential in the form of $\phi=\phi(x_2,x_3,t)$.

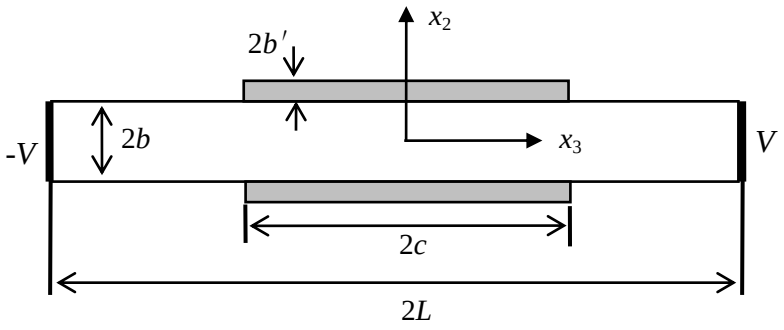

Fig. 3.1 A piezoelectric plate with mass layers and coordinate system

3.3 Governing Equations

For straight-crested waves without x_1 dependence in a plate with mass layers, the relevant equations of Mindlin's first-order plate theory reduce to the following equations of motion and electrostatics [7]:

$$\begin{aligned} &T_{31,3}^{(0)} = 2b\rho(1+R)\ddot{u}_1^{(0)}, \\ &T_{31,3}^{(1)} - T_{21}^{(0)} = \frac{2b^3}{3}\rho(1+3R)\ddot{u}_1^{(1)}, \\ &D_{3,3}^{(0)} = 0, \\ &D_{3,3}^{(1)} - D_2^{(0)} = 0, \end{aligned} \tag{3-1}$$

where $u_1^{(0)}(x_3,t)$ is the FS displacement, a low-frequency mode. $u_1^{(1)}(x_3,t)$ is the TT displacement, a high-frequency mode. They are related to u_1 through $u_1 = u_1^{(0)} + x_2 u_1^{(1)}$. The TT mode is the high-frequency operating mode of devices which is what we are interested in, but it is usually coupled to the FS mode through the elastic constant c_{56} as shown below. Therefore a coupled analysis is necessary. The mechanical and electric resultants in (3-1) are related to the plate displacements $u_1^{(0)}$ and $u_1^{(1)}$ as well as electric potentials $\phi^{(0)}$ and $\phi^{(1)}$ by the following constitutive relations:

$$T_{31}^{(0)} = 2b(c_{55}u_{1,3}^{(0)} + \kappa_1 c_{56}u_1^{(1)} + e_{25}\phi^{(1)} + e_{35}\phi_{,3}^{(0)}), \tag{3-2a}$$

$$T_{12}^{(0)} = 2b(\kappa_1 c_{56}u_{1,3}^{(0)} + \kappa_1^2 c_{66}u_1^{(1)} + \kappa_1 e_{26}\phi^{(1)} + \kappa_1 e_{36}\phi_{,3}^{(1)}), \tag{3-2b}$$

$$T_{31}^{(1)} = \frac{2b^3}{3}(\gamma_{55}u_{1,3}^{(1)} + \psi_{35}\phi_{,3}^{(1)}), \tag{3-2c}$$

$$D_2^{(0)} = 2b(e_{25}u_{1,3}^{(0)} + \kappa_1 e_{26}u_1^{(1)} - \varepsilon_{22}\phi^{(1)} - \varepsilon_{23}\phi_{,3}^{(1)}), \tag{3-2d}$$

$$D_3^{(0)} = 2b(e_{35}u_{1,3}^{(0)} + \kappa_1 e_{36}u_1^{(1)} - \varepsilon_{23}\phi^{(1)} - \varepsilon_{33}\phi_{,3}^{(0)}), \tag{3-2e}$$

$$D_3^{(1)} = \frac{2b^3}{3}(\psi_{35}u_{1,3}^{(1)} - \zeta_{33}\phi_{,3}^{(1)}). \tag{3-2f}$$

$\phi^{(0)}$ and $\phi^{(1)}$ are related to the potential ϕ through $\phi = \phi^{(0)} + x_2\phi^{(1)}$. In (3-2), $c_{pq}(=c_{pq}^E)$, e_{ip}, and $\varepsilon_{ij}(=\varepsilon_{ij}^S)$ are the usual elastic stiffness, piezoelectric constants, and dielectric constants. The other material constants in (3-2) are defined by

$$\begin{aligned} &\gamma_{55} = 1/s_{55}, \quad \psi_{35} = e_{35} - e_{36}c_{56}/c_{66} = d_{35}\gamma_{55}, \\ &\zeta_{33} = \varepsilon_{33} + e_{36}^2/c_{66}, \end{aligned} \tag{3-3}$$

where $s_{pq}(=s_{pq}^E)$ is the elastic compliance and d_{ip} is another set of piezoelectric constants different from but related to e_{ip}. For a plate with dielectric mass layers at the major surfaces at $x_2 = \pm b$, the shear correction factor κ_1 and the mass ratio *R* in the above equations are given by

$$\kappa_1^2 = \frac{\pi^2}{12}(1+R), \quad R = \frac{2\rho' b'}{\rho b}. \tag{3-4}$$

When (3-2) is substituted into (3-1), the following four equations result:

$$\begin{aligned} &c_{55}u_{1,33}^{(0)} + e_{35}\phi_{,33}^{(0)} + \kappa_1 c_{56}u_{1,3}^{(1)} + e_{25}\phi_{,3}^{(1)} = \rho(1+R)\ddot{u}_1^{(0)}, \\ &\gamma_{55}u_{1,33}^{(1)} + \psi_{35}\phi_{,33}^{(1)} \\ &\quad - 3b^{-2}(\kappa_1 c_{56}u_{1,3}^{(0)} + \kappa_1^2 c_{66}u_1^{(1)} + \kappa_1 e_{26}\phi^{(1)} + \kappa_1 e_{36}\phi_{,3}^{(0)}) = \rho(1+3R)\ddot{u}_1^{(1)}, \\ &e_{35}u_{1,33}^{(0)} + \kappa_1 e_{36}u_{1,3}^{(1)} - \varepsilon_{33}\phi_{,33}^{(0)} - \varepsilon_{23}\phi_{,3}^{(1)} = 0, \\ &\psi_{35}u_{1,33}^{(1)} - \zeta_{33}\phi_{,33}^{(1)} - 3b^{-2}(e_{25}u_{1,3}^{(0)} + \kappa_1 e_{26}u_1^{(1)} - \varepsilon_{22}\phi^{(1)} - \varepsilon_{23}\phi_{,3}^{(0)}) = 0. \end{aligned} \tag{3-5}$$

The equations for a plate without mass layers can be obtained from the above equations by setting the mass ratio R=0.

3.4 Dispersion Relations for Waves in Unbounded Plates

To understand energy trapping it is helpful to examine the dispersion relations for coupled FS and TT waves in unbounded plates. Let the wave frequency be ω and wave number along x_3 be ζ, and

$$\begin{aligned} u_1^{(0)} &= A_1 \cos(\zeta x_3 - \omega t), \quad u_1^{(1)} = A_2 \sin(\zeta x_3 - \omega t), \\ \phi^{(0)} &= A_3 \cos(\zeta x_3 - \omega t), \quad \phi^{(1)} = A_4 \sin(\zeta x_3 - \omega t), \end{aligned} \tag{3-6}$$

where A_1-A_4 are undetermined constants, ζ is wave number, and ω is frequency. (3-6) represents waves propagating in the x_3 direction. Substitution of (3-6) into (3-5) results in four linear, homogeneous equations for A_1-A_4. For nontrivial solutions the determinant of the coefficient matrix has to vanish, which yields an equation that determines ω versus ζ, or the dispersion relation. It is a quadratic equation for ω^2, which is too long to be presented here. For a given ζ, there are two roots for ω^2. For each root of ω^2, the two corresponding values of ω only differ by a sign and examining one of them is sufficient. We introduce the following dimensionless frequency Ω and dimensionless wave number Z

$$\Omega = \frac{\omega}{\omega_0}, \qquad Z = \zeta \Big/ \frac{\pi}{2b}, \qquad \omega_0^2 = \frac{\pi^2}{4\rho b^2}(c_{66} + e_{26}^2/\varepsilon_{22}), \tag{3-7}$$

where ω_0 is the plate fundamental thickness-shear frequency and is use as a normalizing frequency.

Dispersion relations for coupled FS and TT waves are shown in Fig. 3.2 for two cases together. One is for an infinite plate without mass layers. The other is for an infinite plate completely covered by mass layers, which has lower frequencies as expected. The branch for the TT wave has a finite intercept with the frequency axis, which is the cutoff frequency below which the TT wave cannot propagate. When mass layers are present, the TT wave cutoff frequency is also lowered a little. For a frequency in the small range between the two cutoff frequencies, the corresponding TT wave number for the plate with mass layers is real, representing a sinusoidal wave. At the same time, the corresponding TT wave number for the plate without mass layers is pure imaginary, representing an exponentially decaying field. Hence, if a plate has partial mass layers like what is shown in Fig. 3.1, in the small frequency range between the two cutoff frequencies, the vibration is sinusoidal under the mass layers and is exponentially decaying outside them, and is therefore confined to be within the part of the plate with mass layers (energy trapping). In this case, mounting at some distance away from the mass layer edges does not affect the vibration of the structure.

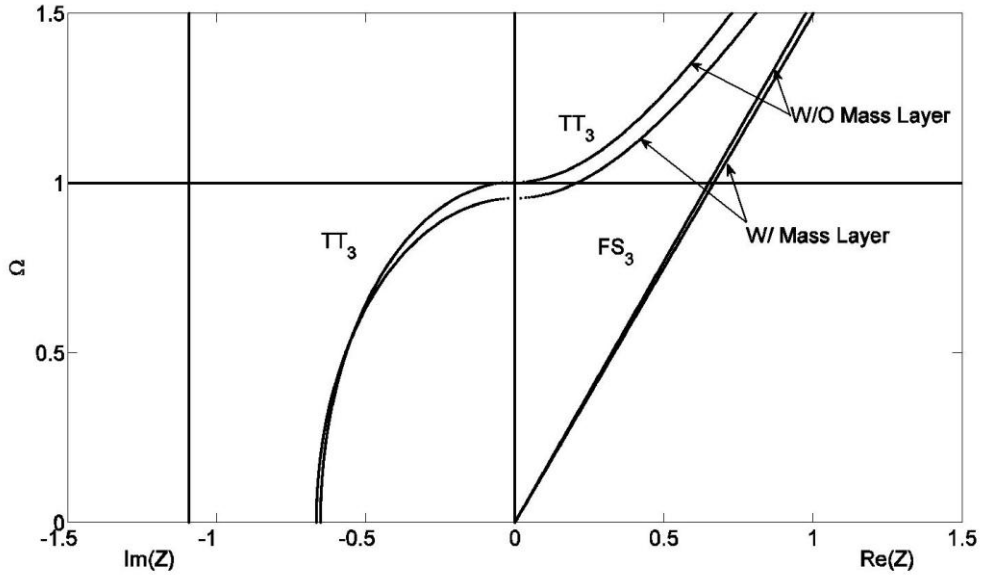

Fig. 3.2 Dispersion curves for plates with and without mass layers.

3.5 Vibrations of Finite Plates with Partial Mass Layers

In this section we study vibrations and energy trapping in the plate with partial mass layers as shown in Fig. 3.1. Due to the presence of partial mass layers, we need to obtain solutions for plates with and without mass layers separately, and then apply boundary conditions at the edges of the plate and continuity conditions at the junctions between different parts of the plate.

3.5.1 Central portion with mass layers

We consider stationary waves in the form of

$$\begin{aligned} u_1^{(0)} &= A_1 \sin(\zeta x_3)\exp(i\omega t), \quad u_1^{(1)} = A_2 \cos(\zeta x_3)\exp(i\omega t), \\ \phi^{(0)} &= A_3 \sin(\zeta x_3)\exp(i\omega t), \quad \phi^{(1)} = A_4 \cos(\zeta x_3)\exp(i\omega t), \end{aligned} \tag{3-8}$$

where A_1-A_4 are undetermined constants. (3-8) may be called symmetric modes because the main displacement of interest, $u_1^{(1)}$, is an even function of x_3. There are also modes with $u_1^{(1)}$ being an odd function of x_3 which may be called antisymmetric modes. Antisymmetric modes are of less interest because they cannot be excited by a lateral electric field in the symmetric structure in Fig. 3.1, and therefore will not be studied in this chapter. We look for steady-state solutions in which all fields are with the same time dependence which will be dropped for simplicity. Substitution of (3-8) into (3-5) results in four linear equations for A_1-A_4. For nontrivial solutions the determinant of the coefficient has to vanish, which yields a polynomial equation of degree four for ζ^2. There are four roots which are denoted by $(\zeta^{(m)})^2$, with m=1-4. Corresponding to a

typical $\zeta^{(m)}$, let the nontrivial solution of the linear equations (eigenvector) be $\beta_p^{(m)}$ with p=1-4. $\beta_p^{(m)}$ determines the ratios among A_1-A_4. It turns out that one of the roots for $(\zeta^{(m)})^2$ is zero. The general symmetric solution can be constructed as

$$\begin{Bmatrix} u_1^{(0)} \\ u_1^{(1)} \\ \phi^{(0)} \\ \phi^{(1)} \end{Bmatrix} = \sum_{m=1}^{3} \overline{C}^{(m)} \begin{Bmatrix} \beta_1^{(m)} \sin\left(\zeta^{(m)} x_3\right) \\ \beta_2^{(m)} \cos\left(\zeta^{(m)} x_3\right) \\ \beta_3^{(m)} \sin\left(\zeta^{(m)} x_3\right) \\ \beta_4^{(m)} \cos\left(\zeta^{(m)} x_3\right) \end{Bmatrix} + \overline{C}^{(4)} \begin{Bmatrix} 0 \\ A_1 \\ x_3 \\ B_1 \end{Bmatrix}, \tag{3-9}$$

where $\overline{C}^{(1)}$ through $\overline{C}^{(4)}$ are undetermined constants, and

$$\begin{aligned} A_1 &= -\frac{\varepsilon_{22}\kappa_1 e_{36} - \varepsilon_{23}\kappa_1 e_{26}}{\kappa_1^2 \varepsilon_{22} c_{66} + \kappa_1^2 e_{26}^2 - \frac{b^2}{3}\rho\omega^2 \varepsilon_{22}}, \\ B_1 &= -\left(\frac{\varepsilon_{23}}{\varepsilon_{22}} - \frac{\kappa_1^2 \varepsilon_{22} e_{26} e_{36} - \kappa_1^2 \varepsilon_{23} e_{26}^2}{\kappa_1^2 \varepsilon_{22}^2 c_{66} + \kappa_1^2 \varepsilon_{22} e_{26}^2 - \frac{b^2}{3}\rho\omega^2 \varepsilon_{22}^2} \right). \end{aligned} \tag{3-10}$$

3.5.2 Side portions without mass layers

Due to the symmetry of the structure in Fig. 3.1 and the symmetric modes we are studying, we only need to consider the right part of the plate in Fig. 3.1 with $c < x_3 < L$. Corresponding to a frequency in the small range between the two cutoff frequencies in Fig. 3.2, there are real and pure imaginary roots for the wave number. In addition, both of the terms with $u_1^{(1)}$ as an even and an odd function of x_3 should be included. In a way similar to the procedure from (3-8) to (3-9), the general solution for this case can be written as

$$\begin{Bmatrix} u_1^{(0)} \\ u_1^{(1)} \\ \phi^{(0)} \\ \phi^{(1)} \end{Bmatrix} = \sum_{\substack{m=1 \\ \text{Real } \zeta}} C^{(m)} \begin{Bmatrix} \beta_1^{(m)} \sin\left(\zeta^{(m)} x_3\right) \\ \beta_2^{(m)} \cos\left(\zeta^{(m)} x_3\right) \\ \beta_3^{(m)} \sin\left(\zeta^{(m)} x_3\right) \\ \beta_4^{(m)} \cos\left(\zeta^{(m)} x_3\right) \end{Bmatrix} + \sum_{\substack{m=2 \\ \text{Real } \zeta}} C^{(m)} \begin{Bmatrix} \beta_1^{(m)} \cos\left(\zeta^{(m)} x_3\right) \\ \beta_2^{(m)} \sin\left(\zeta^{(m)} x_3\right) \\ \beta_3^{(m)} \cos\left(\zeta^{(m)} x_3\right) \\ \beta_4^{(m)} \sin\left(\zeta^{(m)} x_3\right) \end{Bmatrix}$$
$$+ \sum_{\substack{m=3\text{-}6 \\ \text{Imaginary } \zeta}} C^{(m)} \begin{Bmatrix} \beta_1^{(m)} \exp\left(\zeta^{(m)} x_3\right) \\ \beta_2^{(m)} \exp\left(\zeta^{(m)} x_3\right) \\ \beta_3^{(m)} \exp\left(\zeta^{(m)} x_3\right) \\ \beta_4^{(m)} \exp\left(\zeta^{(m)} x_3\right) \end{Bmatrix} + C^{(7)} \begin{Bmatrix} 0 \\ A_2 \\ x_3 \\ B_2 \end{Bmatrix} + C^{(8)} \begin{Bmatrix} 0 \\ 0 \\ 1 \\ 0 \end{Bmatrix}, \tag{3-11}$$

where $C^{(1)}$ through $C^{(8)}$ are undetermined constants.

3.5.3 Boundary and continuity conditions

Resonators are used as elements of electric circuits for alternating currents. Two basic properties of a resonator, its resonant frequency and capacitance, are of primary interest for circuit analyses. Existing theoretical results on piezoelectric resonators are overwhelmingly on free-vibration frequency analysis. The capacitance of a resonator can only be obtained from an electrically forced vibration analysis. The capacitance of a piezoelectric resonator is called the motional capacitance because mechanical vibration of the resonator is involved through piezoelectric coupling. To calculate the motional capacitance of the resonator in Fig. 3.1, we consider the following boundary conditions for electrically forced vibration:

$$\begin{aligned}
&u_1^{(0)}(c^-) = u_1^{(0)}(c^+), \quad u_1^{(1)}(c^-) = u_1^{(1)}(c^+), \\
&T_{31}^{(0)}(c^-) = T_{31}^{(0)}(c^+), \quad T_{31}^{(1)}(c^-) = T_{31}^{(1)}(c^+), \\
&\phi^{(0)}(c^-) = \phi^{(0)}(c^+), \quad \phi^{(1)}(c^-) = \phi^{(1)}(c^+), \\
&D_3^{(0)}(c^-) = D_3^{(0)}(c^+), \quad D_3^{(1)}(c^-) = D_3^{(1)}(c^+), \\
&T_{31}^{(0)}(L) = 0, \quad T_{31}^{(1)}(L) = 0, \quad \phi^{(0)}(L) = V \exp(i\omega t), \quad \phi^{(1)}(L) = 0.
\end{aligned} \tag{3-12}$$

Due to symmetry, we only need to consider the boundary conditions at $x_3 = L$ and the continuity conditions at $x_3 = c$. Substituting (3-9) and (3-11) into (3-12), we obtain twelve linear, inhomogeneous equations for the twelve undetermined constants of $\overline{C}^{(1)}$ through $\overline{C}^{(4)}$ and $C^{(1)}$ through $C^{(8)}$, driven by *V*. Once these equations are solved on a computer, the plate displacements and potentials are known. Then the charge Q_e on the electrode at the right edge and capacitance *C* of the resonator can be calculated from

$$Q_e = -D_3^{(0)}(x_3 = c), \quad C = \frac{Q_e}{2V}. \tag{3-13}$$

3.5.4 Numerical results

As a numerical example, *b*=1mm is used. Damping is introduced by allowing the elastic constants to assume complex values, which can represent viscous damping. In our calculations, c_{pq} is replaced by $c_{pq}(1+iQ^{-1})$ where *Q* is a real, large and positive number. For quartz, *Q* is of the order of 10^5. We use $Q=10^4$ which is relatively small and represents relatively high damping. It is considered to be a single damping parameter representing all of the damping in the resonator. Note that the ω_0 in (3-2) is kept real as a frequency unit. We also fix the plate length *L/b*=50 and the mass ratio *R*=5%. In Figs. 3.3-3.5, we vary the length of the mass layers from *c/b*=8, 20, to 26.8 and plot the motional capacitance versus the driving frequency in Figs. 3.3(a), 3.4(a), and 3.5(a). The capacitance assumes maxima at resonances. When *c/b* increases, in the frequency interval considered, the number of resonances increases. The displacement distributions at resonances are shown in Figs. 3.3(b), 3.4 (b), and 3.5(b), respectively. The displacement

is large under the mass layers and small outside them. This is the co-called energy trapping phenomenon. Lower-order modes are trapped better. Even for a long and thin plate with L/b=50, the displacement field can still reach the edges. This is because we are considering coupled FS and TT motions. While the TT mode has a cutoff frequency and can be trapped, the FS mode does not have a cutoff frequency and cannot be trapped. As a consequence, the coupled motion can always feel the plate edges.

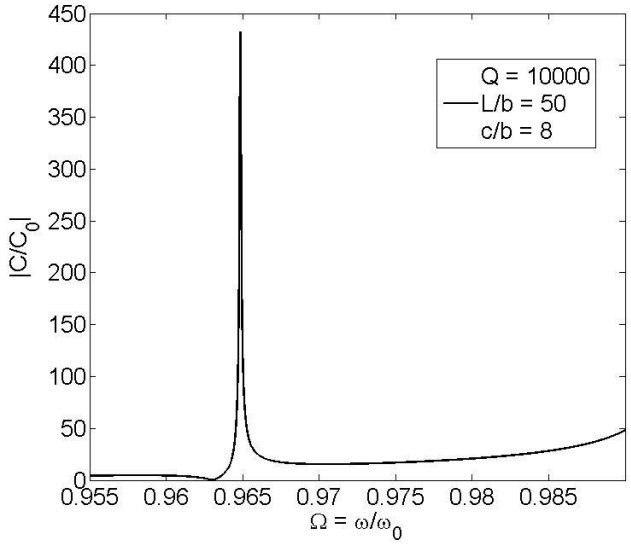

(a)

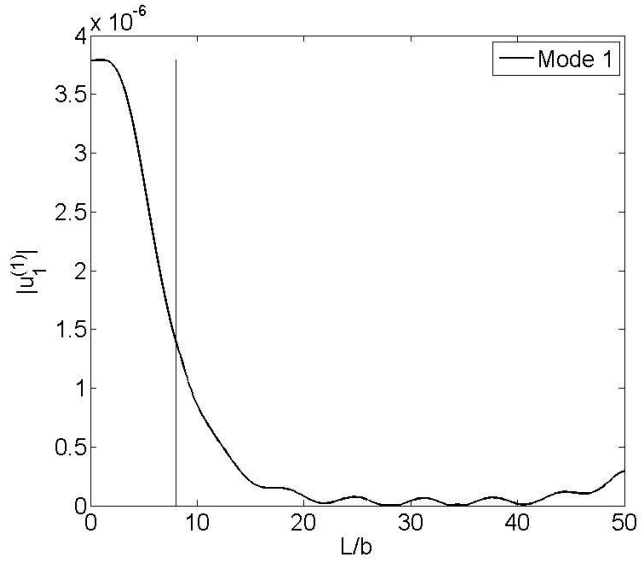

(b)

Fig. 3.3 *c/b*=8. (a) Capacitance versus frequency. (b) Displacement distribution at resonance (Ω =0.964845).

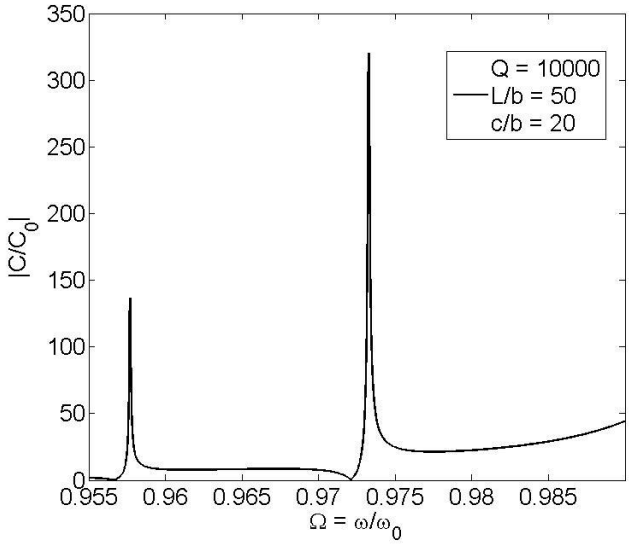

(a)

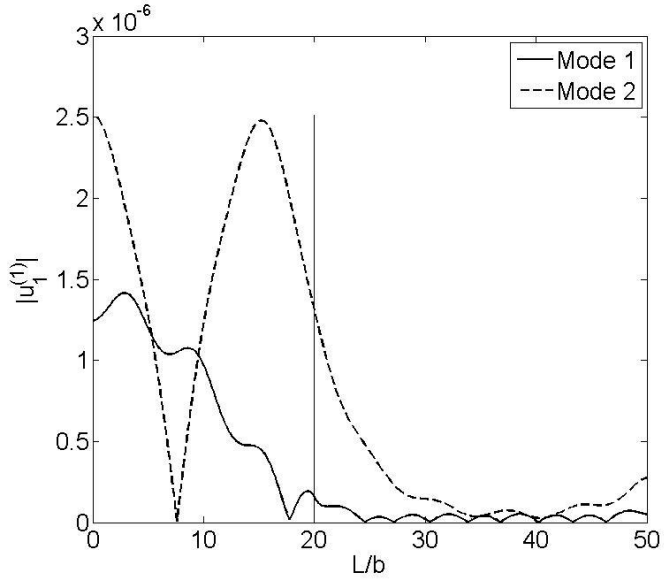

(b)

Fig. 3.4 *c/b*=20. (a) Capacitance versus frequency. (b) Displacement distributions at resonances (Ω =0.957691, 0.973267).

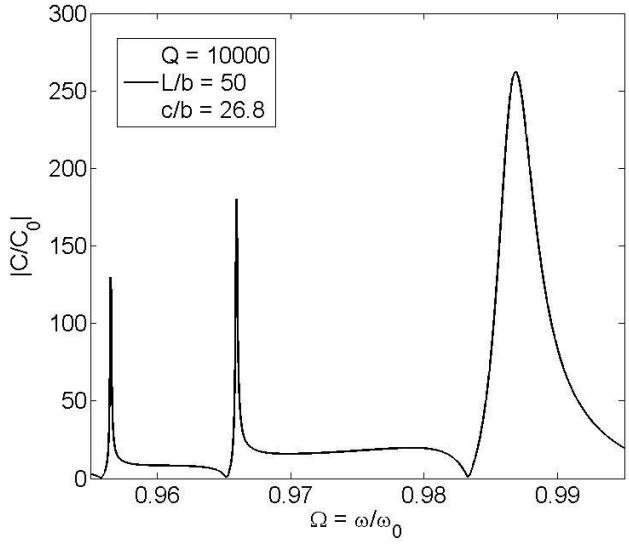

(a)

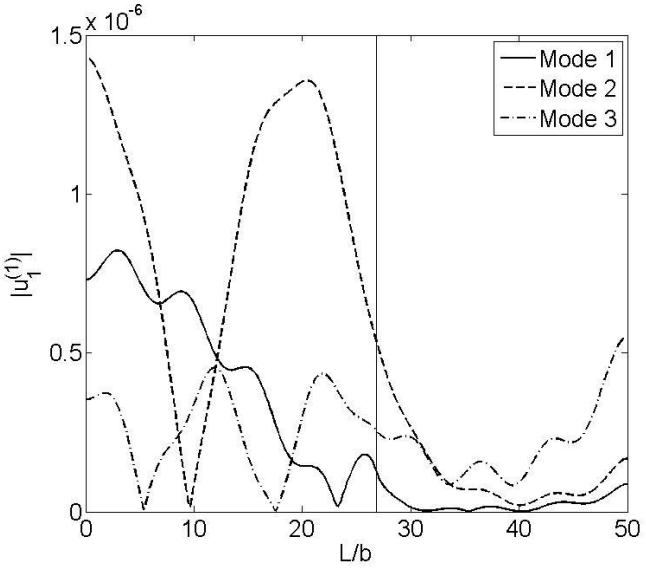

(b)

Fig. 3.5 *c/b*=26.8. (a) Capacitance versus frequency. (b) Displacement distributions at resonances (Ω =0.956521, 0.965944, 0.986854)

3.6 Conclusion

When an AT-cut quartz plate under LFE has partial mass layers, there exist a finite number of resonances in the frequency range between the cutoff frequencies of a plate with mass layers and a plate without mass layers. The motional capacitance assumes maxima at these resonances. The corresponding displacement distributions show energy trapping, with the vibration mainly in the part of the plate with mass layers. The number of trapped modes increases with the length of the mass layers. Lower-order modes are trapped better. Due to the coupling to the FS mode which cannot be trapped, the vibration can still feel the plate boundary slightly.

3.7 Reference

[1] R. D. Mindlin and P. C. Y. Lee, "Thickness-shear and flexural vibrations of partially plated, crystal plates," Int. J. Solids Structures, 2, 125-139, 1966.

[2] J. Wang, P. C. Y. Lee, D. H. Bailey, "Thickness-shear and flexural vibrations of linearly contoured crystal strips with multiprecision computation," Computers & Structures, 70 (4), 437-445, 1999.

[3] R. J. Byrne, P. Lloyd and W. J. Spencer, "Thickness-shear vibrations in rectangular AT-cut quartz plates with partial electrodes," J. Acoust. Soc. Am., 43 (2), 232-238, 1968.

[4] J. L. Bleustein and H. F. Tiersten, "Forced thickness-shear vibrations of discontinuously plated piezoelectric plates," J. Acoust. Soc. Am., 43 (6), 1311-1318, 1968.

[5] P. C. Y. Lee and W. J. Spencer, "Shear-flexure-twist vibrations in rectangular AT-cut quartz plates with partial electrodes," J. Acoust. Soc. Am., 45 (3), 637-645, 1969.

[6] J. S. Yang and J. A. Kosinski, "Effects of piezoelectric coupling on energy trapping of thickness-shear modes," IEEE Trans. Ultrason., Ferroelect., Freq. Contr., 51 (9), 1047-1049, 2004.

[7] R. D. Mindlin, "High frequency vibrations of plated, crystal plates," in: Progress in Applied Mechanics (the Prager Anniversary Volume), Macmillan, New York, 73-84, 1963.

4. Fluid-induced Frequency Shift in a Piezoelectric Plate Driven by Lateral Electric Fields

4.1 Introduction

A vibrating crystal (resonator) when is put in contact with a viscous fluid changes its resonant frequencies due to the inertia and viscosity of the fluid. This effect has been used to make fluid sensors for measuring fluid viscosity or density [1-3]. These sensors belong to the general category of those acoustic wave sensors called quartz crystal microbalances (QCMs). More references can be found in relevant review articles [4, 5]. For fluid sensor applications, vibration modes of a crystal body without a normal displacement at its surface are ideal and are of general interest. In these modes the surface of the body has no normal displacement so that no pressure waves are generated in the fluid. The fluid produces a tangential drag only on the body surface due to viscosity and the tangential motion of the surface, thereby causing a frequency shift in the body.

Quartz is the main piezoelectric crystal for resonator and sensor applications. Thickness-shear vibration of a quartz plate is the most widely used structure and mode for QCMs. The sensitivity given in the classical reference [1] for a fluid sensor is based on an elastic analysis without piezoelectric coupling which is small in quartz and can usually be neglected in a free vibration frequency analysis but must be considered in an electrically forced vibration analysis to obtain the impedance or admittance of a device. In real device operations electrodes are necessary for generating electric fields or collecting charges (currents). Electrodes are usually deposited on the two surfaces of a

crystal plate to produce a driving electric field in the plate thickness direction. This type of electrode arrangement is called thickness field excitation (TFE). Surface deposited electrodes are associated with a series of complicating effects including electrode inertia, stiffness, intrinsic stress, and thermal expansion which is usually incompatible with that of the crystal plate, etc. [6-8]. These effects of the electrodes are usually undesirable, especially when the electrodes are on the surface of the crystal plate where sensing is performed.

One way to avoid putting an electrode on the sensing surface of a crystal plate is to use side electrodes and the associated lateral or in-plane electric fields, called lateral field excitation (LFE) [9-12]. This makes LFE convenient for sensor applications in which the unelectroded active area of a resonator can be put in direct contact with measurands. However, there are very few theoretical results for devices driven by LFE in contrast to the vast literature on TFE.

In this chapter we study thickness-shear vibration of a quartz crystal plate with one surface in contact with a viscous fluid layer. The crystal plate is under LFE. The theory of linear piezoelectricity is used to model the crystal plate. The theory of Newtonian fluids is used for the fluid layer. For fluid sensor application we want to study fluid-induced frequency shift of the crystal plate from a free vibration analysis, and the capacitance of the plate from a forced vibration analysis.

4.2 Fields in different regions

Consider the structure shown in Fig. 4.1 which is unbounded in the x_1 direction. The crystal plate is of rotated Y-cut quartz which includes the widely used AT-cut quartz as a special case. The fluid is a linear Newtonian fluid. Whether the fluid is compressible or not does not matter because the motion to be considered is a pure shear without volume change. There are two edge electrodes at $x_3 = \pm c$. On these electrodes a driving voltage of $\phi = \pm V \exp(i\omega t)/2$ is applied where ϕ is the electric potential. We assume thin plates with *c*>>*b* so that edge effects can be neglected and pure thickness-shear modes exist. We consider time-harmonic motions and use the usual complex notation. All fields have the same $\exp(i\omega t)$ factor which will be dropped in the following for simplicity.

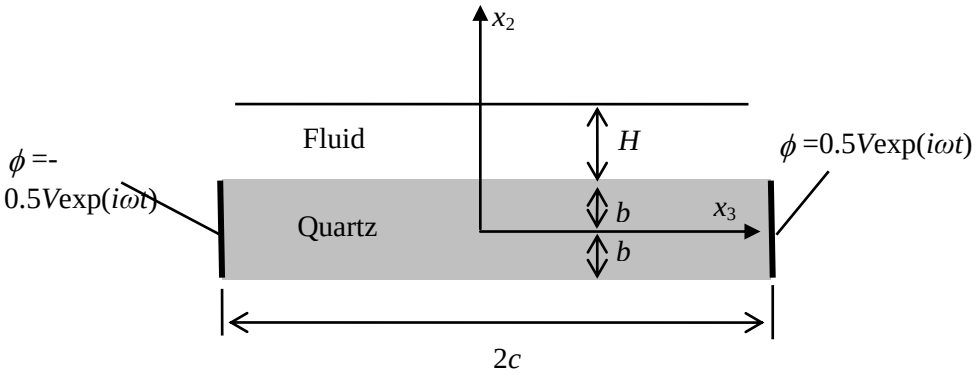

Fig. 4.1 A crystal plate with a fluid under a separated electrode

4.2.1 Upper free space

For thickness-shear modes independent of x_1 and x_3 in the plate, the corresponding governing equations of the electric field in the free space are

$$\begin{aligned} &D_{2,2} = 0, \\ &D_2 = \varepsilon_0 E_2, \\ &E_2 = -\phi_{,2}, \end{aligned} \tag{4-1}$$

where **E** is the electric field and **D** is the electric displacement. ε_0 is the free-space permittivity. We consider the case when $x_2 = \pm\infty$ are electrically open where $D_2 = 0$. Since D_2 is a constant in the free space as dictated by (4-1)$_1$, $D_2 \equiv 0$ in the free space. The free space electric potential is simply

$$\phi = -Ex_3 + C_1, \tag{4-2}$$

where $E = -V/2c$ is a constant, C_1 is an arbitrary constant. (4-2) implies that $E_3 = E$ and $D_2 = 0$. The open circuit condition at $x_2 = +\infty$ is satisfied.

4.2.2 Fluid

The fluid is assumed to be without electromechanical coupling. The electric fields are still governed by (4-1) but the free-space permittivity ε_0 needs to be replaced by the fluid permittivity ε. The equation of motion for the fluid is [13]

$$T_{21,2} = \rho_L \dot{v}_1, \tag{4-3}$$

where the shear stress is given by

$$T_{21} = \mu \frac{\partial v_1}{\partial x_2} \ . \tag{4-4}$$

μ and ρ_L are the viscosity and mass density of the fluid. v_1 and T_{21} are the relevant velocity and shear stress components. The potential and velocity fields in the fluid are

$$\begin{aligned} &\phi = -Ex_3 + C_1, \\ &v_1 = \{C_3 \sinh[(1+i)\eta(x_2 - b)] + C_4 \cosh[(1+i)\eta(x_2 - b)]\}, \end{aligned} \tag{4-5}$$

where C_3 and C_4 are integration constants, and

$$\eta = \sqrt{\frac{\rho_L \omega}{2\mu}} \ . \tag{4-6}$$

The relevant stress and electric displacement components needed for boundary and continuity conditions are

$$\begin{aligned} &T_{21} = (1+i)\mu\eta \{C_3 \cosh[(1+i)\eta(x_2 - b)] + C_4 \sinh[(1+i)\eta(x_2 - b)]\}, \\ &D_2 = 0. \end{aligned} \tag{4-7}$$

We note that the continuity of ϕ and D_2 between the upper free space and the fluid are already satisfied.

4.2.3 Crystal plate

In the crystal plate, due to the presence of E_3, we begin with the following trial fields. They will be shown to satisfy all governing equations and boundary/continuity conditions later.

$$u_1 = u_1(x_2), \quad u_2 = u_3 = 0, \quad \phi = \phi(x_2) - Ex_3 + C_2, \tag{4-8}$$

where C_2 is an undetermined constant. The nontrivial components of the strain, electric field, stress, and electric displacement components are, correspondingly,

$$2S_{12} = u_{1,2}, \quad E_2 = -\phi_{,2} \quad E_3 = -\phi_{,3} = E, \tag{4-9}$$

$$\begin{aligned} T_{31} &= c_{56}u_{1,2} + e_{25}\phi_{,2} - e_{35}E, \quad T_{21} = c_{66}u_{1,2} + e_{26}\phi_{,2} - e_{36}E, \\ D_2 &= e_{26}u_{1,2} - \varepsilon_{22}\phi_{,2} + \varepsilon_{23}E, \quad D_3 = e_{36}u_{1,2} - \varepsilon_{32}\phi_{,2} + \varepsilon_{33}E. \end{aligned} \tag{4-10}$$

The equation of motion and the charge equation of electrostatics take the following form:

$$\begin{aligned} T_{21,2} &= c_{66}u_{1,22} + e_{26}\phi_{,22} = -\rho\omega^2 u_1, \\ D_{2,2} &= e_{26}u_{1,22} - \varepsilon_{22}\phi_{,22} = 0. \end{aligned} \tag{4-11}$$

The displacement and potential fields determined from (4-11) are

$$u_1 = C_5 \sin[\xi(x_2 - b)] + C_6 \cos[\xi(x_2 - b)], \tag{4-12}$$

$$\phi = \frac{e_{26}}{\varepsilon_{22}} \{C_5 \sin[\xi(x_2 - b)] + C_6 \cos[\xi(x_2 - b)]\} + C_7(x_2 - b) - Ex_3 + C_2, \tag{4-13}$$

where C_5, C_6 and C_7 are undetermined constants, and

$$\xi^2 = \frac{\rho}{\bar{c}_{66}}\omega^2 . \tag{4-14}$$

The stress and electric displacement components are

$$T_{21} = \bar{c}_{66}\xi\{C_5\cos[\xi(x_2 - b)] - C_6\sin[\xi(x_2 - b)]\} + e_{26}C_7 - e_{36}E , \tag{4-15}$$

$$D_2 = -\varepsilon_{22}C_7 + \varepsilon_{23}E , \tag{4-16}$$

$$D_3 = \left(e_{36} - \frac{\varepsilon_{32}}{\varepsilon_{22}}e_{26}\right)\xi\{C_5\cos[\xi(x_2 - b)] - C_6\sin[\xi(x_2 - b)]\} - \varepsilon_{32}C_7 + \varepsilon_{33}E , \tag{4-17}$$

where $\bar{c}_{66} = c_{66}(1 + k_{26}^2)$, $k_{26}^2 = e_{26}^2 /(\varepsilon_{22}c_{66})$. The free charge Q_e on the edge electrode at $x_3 = c$ per unit length along x_1, the current I that flows into this electrode, and the admittance Y of the structure are given by

$$\begin{aligned} &Q_e = \int_{-b}^{b} -D_3 dx_2 , \\ &I = \dot{Q}_e = i\omega Q_e , \\ &Y = I/V . \end{aligned} \tag{4-18}$$

4.2.4 Lower free space

For the lower free space we have

$$\phi = -Ex_3 + C_8 , \tag{4-19}$$

where C_8 is an arbitrary constant. The open circuit condition $D_2 = 0$ at $x_2 = -\infty$ is satisfied.

4.3 Boundary and continuity conditions

The top of the fluid layer is traction-free, i.e.,

$$T_{21}(b+H)=0\,. \tag{4-20}$$

At the interface between the fluid and the top of the crystal plate, we have the continuity of the velocity, electric potential, shear stress, and normal electric displacement:

$$\begin{aligned} &\dot{u}_1(b^-)=v_1(b^+),\\ &\phi(b^-)=\phi(b^+),\\ &T_{21}(b^-)=T_{21}(b^+),\\ &D_2(b^-)=0. \end{aligned} \tag{4-21}$$

At the interface between the bottom of the crystal plate and the free space below it, we have:

$$\begin{aligned} &\phi(-b^-)=\phi(-b^+),\\ &D_2(-b^-)=0,\\ &T_{21}(-b^-)=0. \end{aligned} \tag{4-22}$$

We note that although there are eight equations in (4-20)-(4-22), they are effectively seven because D_2 in the crystal plate as given in (4-16) is a constant and $D_2(\pm b^-)=0$ are effectively one condition. Substitution of the relevant fields into (4-20)-(4-22) gives the following seven equations for C_1 through C_8:

$$
\begin{aligned}
&C_3 \cosh\left[(1+i)\eta H\right] + C_4 \sinh\left[(1+i)\eta H\right] = 0,\\
&C_1 - \frac{e_{26}}{\varepsilon_{22}} C_6 = C_2,\\
&\varepsilon_{22} C_7 = \varepsilon_{23} E,\\
&C_4 - i\omega C_6 = 0,\\
&-(1+i)\mu\eta C_3 + \bar{c}_{66}\xi C_5 + e_{26} C_7 = e_{36} E,\\
&\bar{c}_{66}\xi\left[C_5 \cos(2\xi b) + C_6 \sin(2\xi b)\right] + e_{26} C_7 = e_{36} E,\\
&\frac{e_{26}}{\varepsilon_{22}}\left[C_5 \sin(2\xi b) - C_6 \cos(2\xi b)\right] + C_7(2b) + C_8 = C_2.
\end{aligned}
\tag{4-23}
$$

Effectively C_1-C_2 and C_8-C_2 are two constants. Therefore the unknown constants in (4-23) are also seven.

4.4 Vibration analysis

In (4-23) E is the only driving term. In the following we consider free and electrically forced vibrations separately.

4.4.1 Free vibration

For free vibrations we set E=0. (4-23) becomes homogeneous. For nontrivial solutions the determinant of the coefficient matrix of (4-23) has to vanish, which gives the following frequency equation:

$$
\tan\left(2b\omega\sqrt{\frac{\rho}{\bar{c}_{66}}}\right) = -(1-i)\sqrt{\frac{\omega\rho_L\mu}{2\rho\bar{c}_{66}}}\tanh\left[(1+i)\eta H\right]. \tag{4-24}
$$

Quartz has a small piezoelectric coupling. If we neglect the small piezoelectric coupling by setting $e_{26}=0$ (in this case $\bar{c}_{66}=c_{66}$) and consider the limit when $H\to\infty$, (4-24) reduces to

$$\tan\left(2b\omega\sqrt{\frac{\rho}{c_{66}}}\right)=-(1-i)\sqrt{\frac{\omega\rho_L\mu}{2\rho c_{66}}}\,, \tag{4-25}$$

which is the frequency equation in [1].

On the other hand, if we neglect the drag due to fluid viscosity in (4-24) by setting μ=0, the right-hand side of (4-24) vanishes and the left-hand side can be factored into two equations. One is $\sin(\xi b)=0$ which is not of interest because it determines modes that are symmetric about $x_2=0$. What is used in devices is the other equation $\cos(\xi b)=0$ which determines modes antisymmetric about $x_2=0$. In this case,

$$\xi b=n\pi/2\,,\ n=1,\ 3,\ 5,\ \ldots\,. \tag{4-26}$$

Corresponding to (4-26), from (4-14) we obtain the following frequencies for antisymmetric thickness-shear modes when the fluid is not present as our reference frequencies:

$$\omega_0^{(n)}=\frac{n\pi}{2b}\sqrt{\frac{\bar{c}_{66}}{\rho}}\,. \tag{4-27}$$

We now return to the general frequency equation (4-24). Consider the case of a low viscosity fluid, we look for approximate roots of (4-24) by letting

$$\xi b \cong \frac{n\pi}{2} - \Delta^{(n)}, \tag{4-28}$$

where $\Delta^{(n)}$ is small. Substituting (4-28) into (4-24), for small viscosity, we obtain

$$\Delta^{(n)} \cong \frac{1-i}{2}\sqrt{\frac{\rho_L \mu \omega_0^{(n)}}{2\rho \bar{c}_{66}}}\tanh[(1+i)\eta_0^{(n)} H], \tag{4-29}$$

where $\eta_0^{(n)} = \sqrt{\rho_L \omega_0^{(n)}/(2\mu)}$. With $\Delta^{(n)}$ known from (4-29), from (4-14) we obtain the relative frequency shift as

$$\Delta\Omega^{(n)} = \frac{\omega^{(n)} - \omega_0^{(n)}}{\omega_0^{(n)}} = -\frac{2}{n\pi}\Delta^{(n)} = -\frac{1-i}{n\pi}\sqrt{\frac{\rho_L \mu \omega_0^{(n)}}{2\rho \bar{c}_{66}}}\tanh[(1+i)\eta_0^{(n)} H]. \tag{4-30}$$

(4-30) is more general than the classical result in [1] by including the effect of piezoelectric coupling in $\bar{c}_{66}$ and the effect of the finite fluid layer thickness *H*. When $e_{26} = 0$ and $H = \infty$, (4-30) reduces to

$$\Delta\omega^{(n)} = \omega^{(n)} - \omega_0^{(n)} = -\frac{1-i}{n\pi}\omega_0^{(n)}\sqrt{\frac{\rho_L \mu \omega_0^{(n)}}{2\rho \bar{c}_{66}}}. \tag{4-31}$$

When *n*=1, the real part of (4-31) gives the classical result of [1] for the frequency shift of the fundamental thickness-shear mode in a crystal resonator due to contact with a viscous fluid. The real part of (4-31) is negative, indicating that the fluid drag lowers the frequency. From (4-31) higher-order modes with larger *n* seem to have smaller frequency

shifts. The imaginary part of (4-31) represents the damping effect due to the fluid viscosity.

4.4.2 Forced vibration

For forced vibrations (4-23) is inhomogeneous. Under a real driving frequency the coefficient matrix does not vanish. A solution always exists, is unique, and can be obtained directly on a computer.

4.5 Numerical results

We will consider several mixed fluids. For the viscosity of two mixed fluids, we use the following formula from [14]:

$$\begin{aligned} \mu &= X_1^2 \mu_1 + X_2^2 \mu_2 + X_1 X_2 \mu', \\ \mu' &= \mu_1 + \mu_2, \end{aligned} \tag{4-34}$$

where X_1 and X_2 are mole fractions. For the dielectric constant, following [15], we use

$$\varepsilon = \varepsilon_1 p_1 + \varepsilon_2 p_2 , \tag{4-35}$$

where p_i are the relative volume fractions. The mass density of the mixture is based on the ratio between the mass sum and the volume sum.

Consider a resonator of AT-cut quartz with b=0.58 mm so that $\omega_0^{(1)} = 9\times 10^6$ 1/s. The fluid layer thickness is fixed to $H=2b$ except in Figs. 4.2 and 4.3. For the fluids we use ethanol with density ρ_L =0.78522 g/cm^3 and viscosity μ =1.04 mPa s, or toluene with ρ_L

=0.8669 g/cm^3 and μ=0.5503 mPa s, or chloroform with ρ_L=1.483 g/cm^3 and μ=0.542 mPa s.

Fig. 4.2 shows the effect of the fluid layer thickness *H* on frequency shifts due to different fluids for the fundamental mode with *n*=1. The fluid lowers the frequency as expected. For small *H* the frequency shift is proportional to *H*. There is a maximal frequency shift of the order of 10^{-4} when *H* is somewhat less than *b*, half the thickness of the crystal plate. This is considered strong and clear signals because typical thermal noises in quartz resonators are of the order of 10^{-6}. When *H>2b* the frequency shift becomes constant. In this case the fluid layer can in fact be treated as a half space. Fig. 4.3 shows similar behaviors of the third overtone mode with *n*=3, with smaller frequency shifts and quicker decay of fields in the fluids (smaller penetration depth).

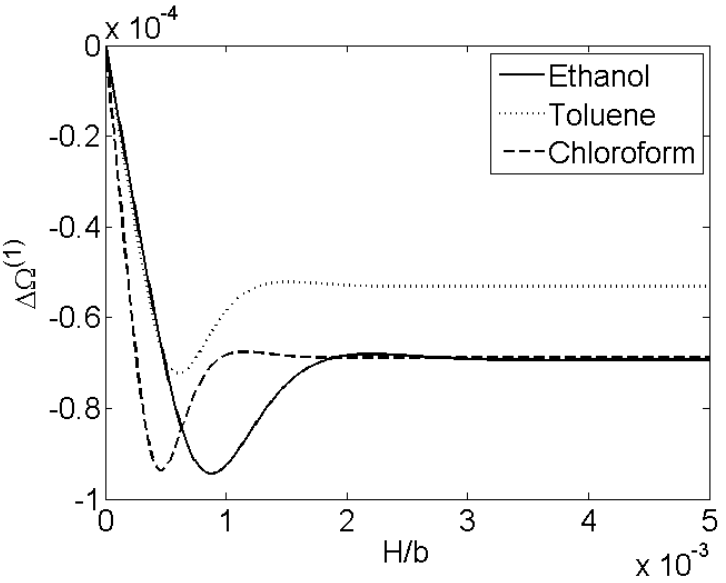

Fig. 4.2 $\Delta\Omega^{(1)}$ versus the fluid layer thickness H

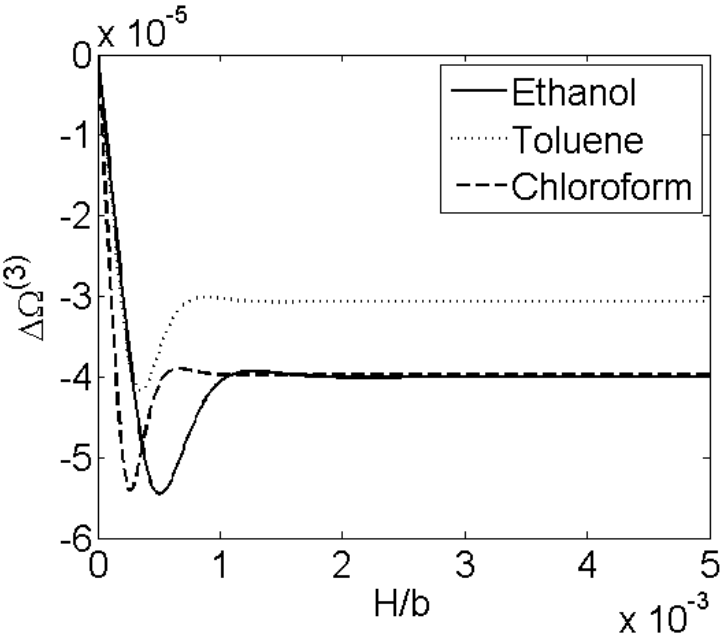

Fig. 4.3 $\Delta\Omega^{(1)}$ versus the fluid layer thickness H

To examine the effect of the fluid density individually, we artificially vary the density of ethanol and plot the result in Fig. 4.4. A heavier fluid with a larger density causes more frequency shift as expected. The relationship between ρ_L and $\Delta\Omega^{(n)}$ is essentially parabolic as suggested by (4-30). In Fig. 4.5 we artificially vary the viscosity of ethanol and observe similar effects.

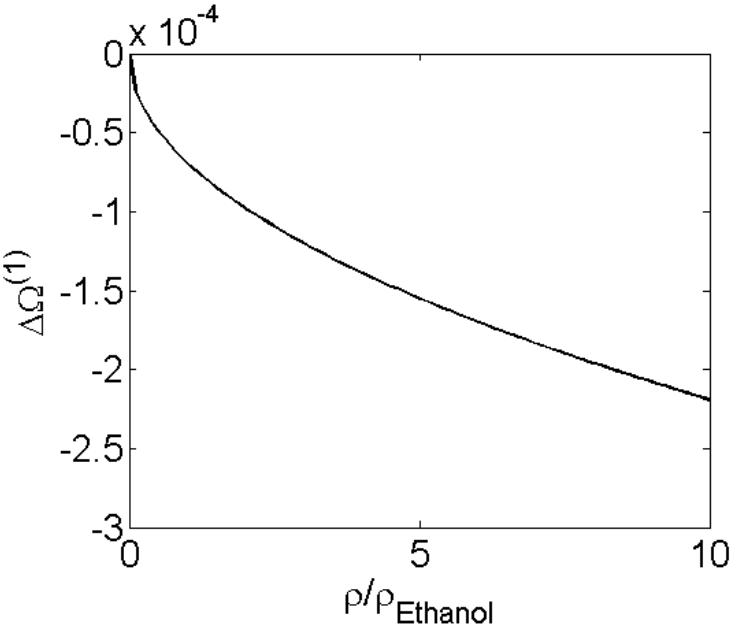

Fig. 4.4 Effects of fluid density on $\Delta\Omega^{(1)}$

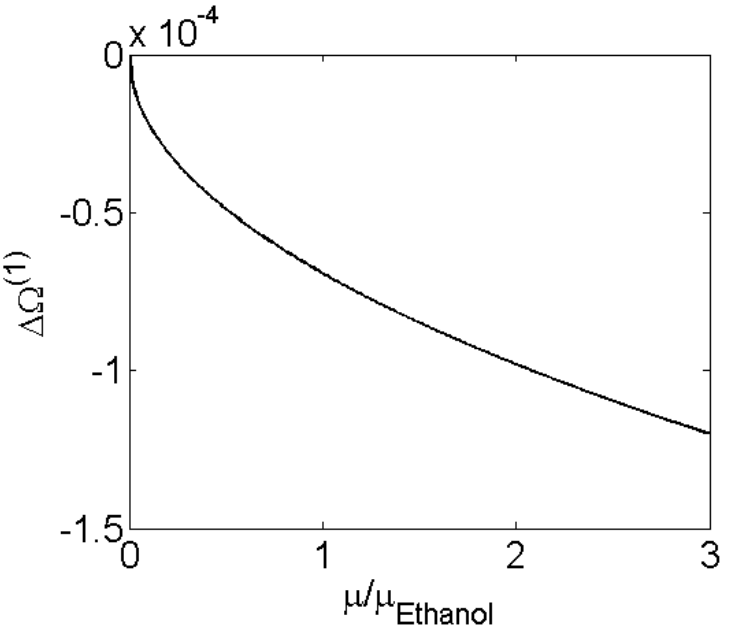

Fig. 4.5 Effects of fluid viscosity on $\Delta\Omega_1^{(1)}$

Fig. 4.6 is from the forced vibration analysis. It shows the admittance per unit length of the plate in the x_1 direction. At resonance the admittance assumes maximum. (a) shows an isolated resonance which is ideal for resonant acoustic wave sensors. (b) is a magnified picture of (a) locally near resonance.

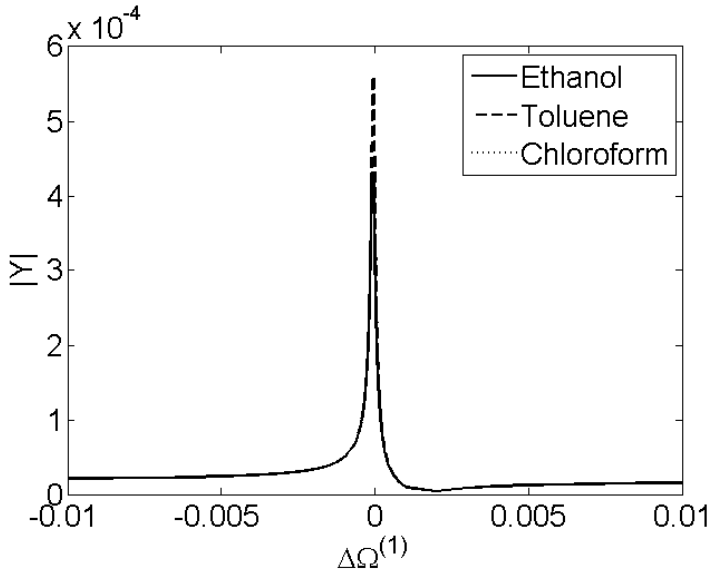

(a)

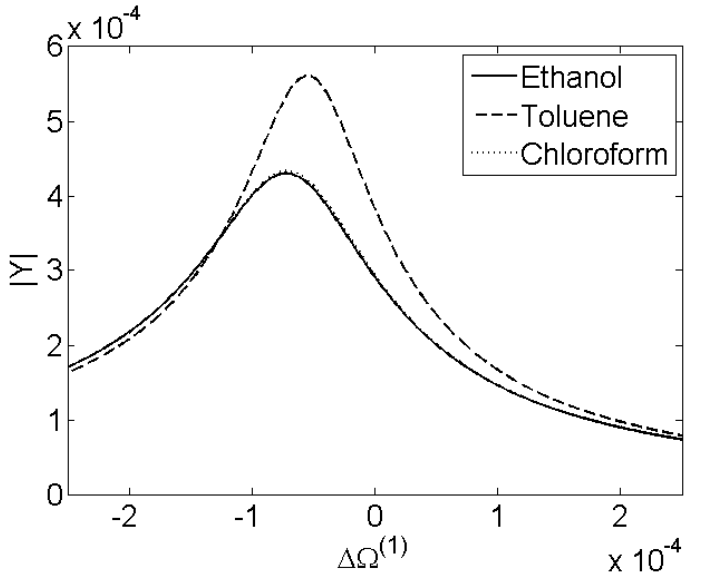

(b)

Fig. 4.6 Admittance versus driving frequency

4.6 Conclusion

An exact solution is obtained for thickness-shear vibrations of a rotated Y-cut quartz plate in contact with a fluid driven by a lateral electric field. An approximate expression for the frequency shifts due to the fluid is presented. It includes the classical result in [1] as a special case. The fluid density and viscosity tend to lower the frequencies of the crystal plate. Higher-order modes are less sensitive to the fluid than lower-order modes. The relative frequency shift is of the order of 10^{-4}. The results obtained are fundamental and useful for the understanding and design of quartz crystal fluid sensors driven by lateral electric fields.

4.7 References

[1] K. K. Kanazawa and J. G. Gordon II, "The oscillation frequency of a quartz resonator in contact with a liquid," Analytica Chimica Acta, 175, 99-105, 1985.

[2] F. Josse, Z. A. Shana, D. E. Radtke and D. T. Haworth, "Analysis of piezoelectric bulk-acoustic- wave resonators as detectors in viscous conductive liquids," IEEE Trans. Ultrason., Ferroelec., Freq. Contr., 37, 359-368, 1990.

[3] C. E. Reed, K. K. Kanazawa and J. H. Haufman, "Physical description of a viscoelastically loaded AT-cut quartz resonator," J. Apl. Phys., 68, 1993-2001, 1990.

[4] E. Benes, "Improved quartz crystal microbalance technique," J. Appl. Phys., 56, 608-626, 1984.

[5] E. Benes, M. Gröschl, W. Burger and M. Schmid, "Sensors based on piezoelectric resonators," Sensors and Actuators, A48, 1-21, 1995.

[6] E. P. EerNisse, "Simultaneous thin-film stress and mass-change measurement using quartz resonators," J. Appl. Phys., 43, 1330-1337, 1972.

[7] H. F. Tiersten and B. K. Sinha, "Temperature dependence of the resonant frequency of electroded doubly-rotated quartz thickness-mode resonators," J. Appl. Phys., 50, 8038-8051, 1979.

[8] H. F. Tiersten and B. K. Sinha, "Intrinsic stress in thin films deposited on anisotropic substrates and its influence on the natural frequencies of piezoelectric resonators," J. Appl. Phys., 52, 5614-5624, 1981.

[9] A. Ballato, E. R. Hatch, M. Mizan and T. L. Lukaszek, "Lateral field equivalent networks and piezocoupling factors of quartz plates driven in simple thickness modes," IEEE Trans. Ultrason., Ferroelec., Freq. Contr., 49(7), 922-928, 2002.

[10] A. Khan and A. Ballato, "Piezoelectric coupling factor calculations for plates of langatate driven in simple thickness modes by lateral-field-excitation," IEEE Trans. Ultrason., Ferroelec., Freq. Contr., 35(3), 435-436, 1988.

[11] R. C. Smythe and H. F. Tiersten, "An approximate expression for the motional capacitance of a lateral field resonator," 41st Annual Symposium on Frequency Control, 311-313, 1987.

[12] P. C. Y. Lee, "Electromagnetic-radiation from an at-cut quartz plate under lateral-field excitation," J. Appl. Phys., 65(4), 1395-1399, 1989

[13] R. L. Panton, "Incompressible Flow", John Wiley and Sons, New York, 1984

[14] R. K. Hind, E. McLaughlin and A. R. Ubbelohde**,** "Structure and viscosity of liquids. Camphor + pyrene mixtures", Trans. Faraday Soc., 56, 328-330, 1960.

[15] Thomas, B. W. *in Treatise on Analytical Chemistry*, Part I; Kolthoff, I. M., Elving, P. J., Eds.; Wiley: New York, 4, p2641, 1963

5. Frequency Shifts in a Quartz Crystal Plate under Separated Electrodes in Contact with a Fluid Layer with a Finite Thickness

5.1 Introduction

Since the missing electrodes on the sensing surfaces, the LFE sensors can provide good sensitivities on the mechanical properties of the fluid. Furthermore, several researchers [1, 2] indicate the LFE sensors are sensitive to the liquid electrical property, such as the permittivity. But in the previous chapter, we cannot find the effect of the liquid electrical property on the frequency shift.

In the real device, the applied electrical field cannot be ideal and homogeneously distributed within the entire quartz plate. As both the two electrodes are on the reference surface and only the sensing surface contacts the liquid layer, the electrical field lines, penetrating into the quartz plate and the liquid layer, also have an x_2-directed component, but very small [3]. This resembles the traditional thickness electric field excitation, but the liquid layer contacts the sensing surface directly. Therefore, a model of TFE sensor with one electrode separated is introduced to qualitatively describe the effect of the liquid permittivity on the frequency shifts in a real LFE liquid sensor.

5.2 Fields in different regions

Consider the structure shown in Fig. 5.1 which is unbounded in the x_1 and x_3 directions. The crystal plate is of rotated Y-cut quartz which includes the widely used AT-cut quartz as a special case. The fluid is a linear Newtonian fluid. Whether the fluid is

compressible or not does not matter because the motion to be considered is a pure shear without volume change. One electrode is at the top of the fluid layer. Another electrode is at the bottom of the crystal plate. Since the mechanical effects of an electrode (or a mass layer) on the crystal surface including inertia and stiffness are well understood [4, 5], in this chapter we focus on the mechanical and electrical effects of the fluid and assume that the electrodes are very thin so that their mechanical effects can be neglected. A time-harmonic driving voltage $V\exp(i\omega t)$ is applied across the electrodes. We consider time-harmonic motions and use the usual complex notation. All fields have the same $\exp(i\omega t)$ factor which will be dropped in the following for simplicity.

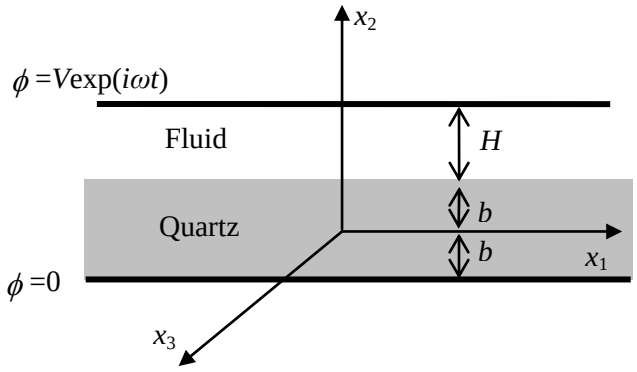

Fig. 5.1 A crystal plate with a fluid under a separated electrode

5.2.1 Fields in the fluid

The fluid is assumed to be without electromechanical coupling. For motions independent of x_1 and x_3, its electric and mechanical fields are governed by

$$\begin{aligned} &D_{2,2} = 0, \\ &D_2 = \varepsilon E_2, \\ &E_2 = -\phi_{,2}, \end{aligned} \tag{5-1}$$

and [6]

$$\begin{aligned} &T_{21,2} = \rho_L \dot{v}_1, \\ &T_{21} = \mu \frac{\partial v_1}{\partial x_2}, \end{aligned} \tag{5-2}$$

respectively. ε, μ, and ρ_L are the dielectric constant, viscosity, and mass density of the fluid. Dielectric losses in the fluid can be represented by a complex ε [7-9]. v_1 and T_{21} are the relevant velocity and shear stress components. (5-1) and (5-2) allow the following fields:

$$\begin{aligned} &\phi = C_1(x_2 - b) + C_2, \\ &D_2 = -\varepsilon C_1, \end{aligned} \tag{5-3}$$

$$\begin{aligned} &v_1 = \{C_3 \sinh[(1+i)\eta(x_2 - b)] + C_4 \cosh[(1+i)\eta(x_2 - b)]\}, \\ &T_{21} = (1+i)\mu\eta\{C_3 \cosh[(1+i)\eta(x_2 - b)] + C_4 \sinh[(1+i)\eta(x_2 - b)]\}, \end{aligned} \tag{5-4}$$

where C_1 through C_4 are integration constants, and

$$\eta = \sqrt{\frac{\rho_L \omega}{2\mu}}\ . \tag{5-5}$$

The free charge Q_e per unit area of the electrode at $x_2 = b + H$, the current I per unit area that flows into this electrode, and the admittance Y per unit electrode area of the structure are given by

$$\begin{aligned} &Q_e = -D_2 = \varepsilon C_1, \\ &I = \dot{Q}_e = i\omega Q_e, \\ &Y = I/V. \end{aligned} \tag{5-6}$$

5.2.2 Fields in the crystal plate

Due to the specific anisotropy of Rotated Y-cut [10], under the given driving voltage, the plate vibrates in thickness-shear motions with

$$u_1 = u_1(x_2)\exp(i\omega t), \quad u_2 = u_3 = 0, \quad \phi = \phi(x_2)\exp(i\omega t)\ . \tag{5-7}$$

The nontrivial components of the strain, electric field, stress, and electric displacement components are [10]

$$2S_{12} = u_{1,2}, \quad E_2 = -\phi_{,2}, \tag{5-8}$$

$$\begin{aligned} &T_{31} = c_{56}u_{1,2} + e_{25}\phi_{,2}, \quad T_{12} = c_{66}u_{1,2} + e_{26}\phi_{,2}, \\ &D_2 = e_{26}u_{1,2} - \varepsilon_{22}\phi_{,2}, \quad D_3 = e_{36}u_{1,2} - \varepsilon_{23}\phi_{,2}. \end{aligned} \tag{5-9}$$

The equation of motion and the charge equation of electrostatics take the following form:

$$T_{21,2} = c_{66}u_{1,22} + e_{26}\phi_{,22} = -\rho\omega^2 u_1\,,$$
$$D_{2,2} = e_{26}u_{1,22} - \varepsilon_{22}\phi_{,22} = 0. \tag{5-10}$$

$(5\text{-}10)_2$ can be integrated to yield

$$\phi = \frac{e_{26}}{\varepsilon_{22}}u_1 + +C_7(x_2 - b) + C_8\,, \tag{5-11}$$

where C_7 and C_8 are integration constants. Substituting (5-11) into the expression for T_{21}, D_2, and $(5\text{-}10)_1$, we obtain

$$T_{21} = \bar{c}_{66}u_{1,2} + e_{26}C_7\,, \quad D_2 = -\varepsilon_{22}C_7\,, \tag{5-12}$$

$$\bar{c}_{66}u_{1,22} = -\rho\,\omega^2 u_1\,, \tag{5-13}$$

where

$$\bar{c}_{66} = c_{66}(1 + k_{26}^2), \quad k_{26}^2 = \frac{e_{26}^2}{\varepsilon_{22}c_{66}}\,. \tag{5-14}$$

The general solution to (5-13), the corresponding expression for the electric potential, and the relevant shear stress and electric displacement components are

$$u_1 = C_5\sin[\xi(x_2 - b)] + C_6\cos[\xi(x_2 - b)]\,, \tag{5-15}$$

$$\phi = \frac{e_{26}}{\varepsilon_{22}}\{C_5\sin[\xi(x_2 - b)] + C_6\cos[\xi(x_2 - b)]\} + C_7(x_2 - b) + C_8\,, \tag{5-16}$$

$$T_{21} = \bar{c}_{66}\xi\{C_5\cos[\xi(x_2 - b)] - C_6\sin[\xi(x_2 - b)]\} + e_{26}C_7\,, \tag{5-17}$$

$$D_2 = -\varepsilon_{22} C_7 , \tag{5-18}$$

where C_5 and C_6 are integration constants, and

$$\xi^2 = \frac{\rho}{\bar{c}_{66}} \omega^2 . \tag{5-19}$$

5.3 Boundary and continuity conditions

The top of the fluid layer is traction-free and has the prescribed electric potential

$$\begin{aligned} &T_{21}(b+H) = 0, \\ &\phi(b+H) = V. \end{aligned} \tag{5-20}$$

At the interface between the fluid and the crystal plate, we have the continuity of the velocity, electric potential, shear stress, and normal electric displacement:

$$\begin{aligned} &\dot{u}_1(b^-) = v_1(b^+), \\ &\phi(b^-) = \phi(b^+), \\ &T_{21}(b^-) = T_{21}(b^+), \\ &D_2(b^-) = D_2(b^+). \end{aligned} \tag{5-21}$$

The bottom of the crystal plate is traction-free and grounded:

$$\begin{aligned} &\phi(-b) = 0, \\ &T_{21}(-b) = 0. \end{aligned} \tag{5-22}$$

Substitution of the relevant fields into (5-20)-(5-22) gives the following eight equations for C_1 through C_8:

$$
\begin{aligned}
&HC_1 + C_2 = V,\\
&\cosh[(1+i)\eta H]C_3 + \sinh[(1+i)\eta H]C_4 = 0,\\
&C_4 - i\omega C_6 = 0,\\
&C_2 - \frac{e_{26}}{\varepsilon_{22}} C_6 - C_8 = 0,\\
&(1+i)\mu\eta C_3 - \bar{c}_{66}\xi C_5 - e_{26} C_7 = 0,\\
&\varepsilon C_1 - \varepsilon_{22} C_7 = 0,\\
&\frac{e_{26}}{\varepsilon_{22}} \sin(-2b\xi) C_5 + \frac{e_{26}}{\varepsilon_{22}} \cos(-2b\xi) C_6 - 2bC_7 + C_8 = 0,\\
&\bar{c}_{66}\xi \cos(-2b\xi) C_5 - \bar{c}_{66}\xi \sin(-2b\xi) C_6 + e_{26} C_7 = 0.
\end{aligned}
\tag{5-23}
$$

5.4 Free and forced vibrations

In (5-23) V is the only driving term. For free vibrations we set V=0 and (5-23) becomes homogeneous. For nontrivial solutions the determinant of the coefficient matrix of (5-23) has to vanish, which gives the following frequency equation:

$$
\begin{aligned}
&\xi(H\frac{\varepsilon_{22}}{\varepsilon} + 2b)\sin(2b\xi) + 2\bar{k}_{26}^{\,2}[\cos(2b\xi) - 1]\\
&= \frac{(1-i)\mu\eta\omega}{\bar{c}_{66}\xi}[\bar{k}_{26}^{\,2}\sin(2b\xi) - \xi(H\frac{\varepsilon_{22}}{\varepsilon} + 2b)\cos(2b\xi)]\tanh[(1+i)\eta H],
\end{aligned}
\tag{5-24}
$$

where $\bar{k}_{26}^2 = e_{26}^{\,2}/(\varepsilon_{22}\bar{c}_{66})$.

If we neglect the piezoelectric coupling in (5-24) by setting $\bar{k}_{26}^2 = 0$ (in this case $\bar{c}_{66} = c_{66}$) and consider the limit when $H \to \infty$, (5-24) reduces to

$$
\tan\left(2b\omega\sqrt{\frac{\rho}{c_{66}}}\right) = -(1-i)\sqrt{\frac{\omega\rho_L\mu}{2\rho c_{66}}}\,, \tag{5-25}
$$

which is the frequency equation in [11].

On the other hand, if we neglect the drag due to fluid viscosity by setting μ=0, the right-hand side of (5-24) vanishes and the left-hand side can be factored into two equations. One is simply $\sin(\xi b)=0$ which is not of interest because in the special case of H=0 this equation determines modes that are essentially symmetric about $x_2=0$ which cannot be excited by a thickness electric field. What is used in devices is the other equation which can be written as

$$\cot(\xi b)=\frac{\bar{k}_{26}^2}{\left(\frac{\varepsilon_{22}H}{2\varepsilon}+b\right)\xi}\ , \tag{5-26}$$

which agrees with [12] for a crystal plate with an air gap under a separated electrode. Modes determined by (5-26) are essentially antisymmetric about $x_2=0$ and can be excited by a thickness electric field. (5-26) shows that in this case the fluid thickness and dielectric constant affect the resonant frequencies of the crystal plate. Quartz has a small piezoelectric coupling. For approximate solutions to (5-26), we neglect the small piezoelectric coupling coefficient, $\bar{k}_{26}^2$, in (5-26). In this case (5-26) has simple roots of

$$\xi b=n\pi/2\,,\ n=1,\ 3,\ 5,\ \ldots\ . \tag{5-27}$$

Corresponding to (5-27), from (5-19) we obtain the following frequencies for TSh vibrations of a crystal plate without piezoelectric coupling as our reference frequencies:

$$\omega_0^{(n)}=\frac{n\pi}{2b}\sqrt{\frac{\bar{c}_{66}}{\rho}}\ . \tag{5-28}$$

We now turn back to (5-24). Consider the case of a low viscosity fluid, we look for approximate roots of (5-24) by letting

$$\xi b \cong \frac{n\pi}{2} - \Delta^{(n)}. \tag{5-29}$$

Substituting (5-29) into (5-24), for small piezoelectric coupling and small viscosity, we obtain

$$\Delta^{(n)} \cong \frac{4\bar{k}_{26}^2}{\left(\frac{\varepsilon_{22}}{\varepsilon}\frac{H}{2b}+1\right)2n\pi} + \frac{1-i}{2}\sqrt{\frac{\rho_L \mu \omega_0^{(n)}}{2\rho \bar{c}_{66}}}\tanh[(1+i)\eta_0^{(n)} H]\,, \tag{5-30}$$

where $\eta_0^{(n)} = \sqrt{\rho_L \omega_0^{(n)}/(2\mu)}$. With $\Delta^{(n)}$ known from (5-30), from (5-19) we obtain the relative frequency shift as

$$\Delta\Omega^{(n)} = \frac{\omega^{(n)} - \omega_0^{(n)}}{\omega_0^{(n)}} = -\frac{2}{n\pi}\Delta^{(n)} = \Delta\Omega_1^{(n)} + \Delta\Omega_2^{(n)}, \tag{5-31}$$

where

$$\begin{aligned} \Delta\Omega_1^{(n)} &= -\frac{4\bar{k}_{26}^2}{\left(\frac{\varepsilon_{22}}{\varepsilon}\frac{H}{2b}+1\right)n^2\pi^2}, \\ \Delta\Omega_2^{(n)} &= -\frac{1-i}{n\pi}\sqrt{\frac{\rho_L \mu \omega_0^{(n)}}{2\rho \bar{c}_{66}}}\tanh[(1+i)\eta_0^{(n)} H]. \end{aligned} \tag{5-32}$$

(5-32) shows that higher-order modes with larger *n* have smaller frequency shifts. $\Delta\Omega_1^{(n)}$ is due to the piezoelectric coupling in the crystal and the dielectric effect of the fluid.

$\Delta\Omega_2^{(n)}$ is due to the density and viscosity of the fluid. $(5\text{-}32)_2$ is more general than the classical result in [11] by including the effects of H. When $H=\infty$, $(5\text{-}32)_2$ reduces to

$$\Delta\omega^{(n)} = \omega^{(n)} - \omega_0^{(n)} = -\frac{1-i}{n\pi}\omega_0^{(n)}\sqrt{\frac{\rho_L \mu \omega_0^{(n)}}{2\rho\bar{c}_{66}}}\,. \tag{5-33}$$

When n=1, the real part of (5-33) gives the classical result of [11] for the frequency shift of the fundamental TSh mode in a crystal resonator due the contact with a viscous fluid.

For forced vibrations (5-23) is nonhomogeneous. Under a real driving frequency the coefficient matrix does not vanish. A solution always exists, is unique, and can be obtained directly on a computer.

5.5 Numerical results

Consider a resonator with $\omega_0 = 9\times10^6$ 1/s and $H=2b$ unless otherwise stated. The fluid is ethanol mixed with toluene, chloroform, or water. We plot $\Delta\Omega_1^{(n)}$ versus the ethanol volume fraction for n=1 and 3 in Fig. 5.2 (a) and (b), respectively. The frequency shift of the mode with n=1 is an order of magnitude larger than that of the mode with n=3.

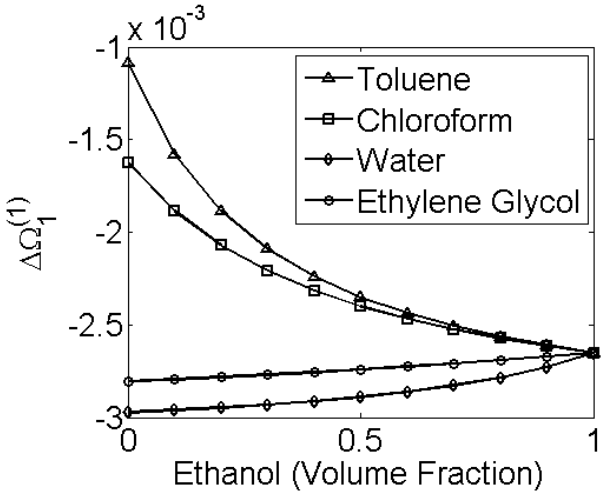

(a)

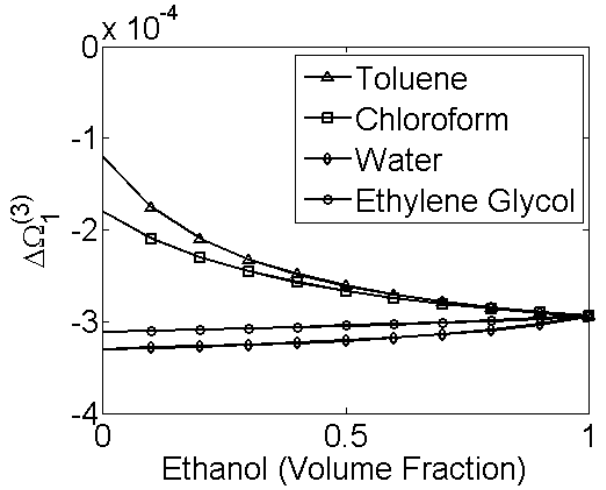

(b)

Fig. 5.2 $\Delta\Omega_1^{(n)}$ versus the volumn fraction of ethanol. (a) *n*=1; (b) *n*=3

Fig. 5.3 shows $\Delta\Omega_2^{(n)}$ versus the ethanol volume fraction for n=1 and 3 in (a) and (b), respectively. Again the frequency shift of the mode with n=1 is larger than that of the mode with n=3. Comparing Fig. 5.3 with Fig. 5.2, we see that the frequency shifts due to the fluid viscosity and density in Fig. 5.3 is an order of magnitude smaller that that due to piezoelectric coupling of the crystal and the dielectric constant of the fluid.

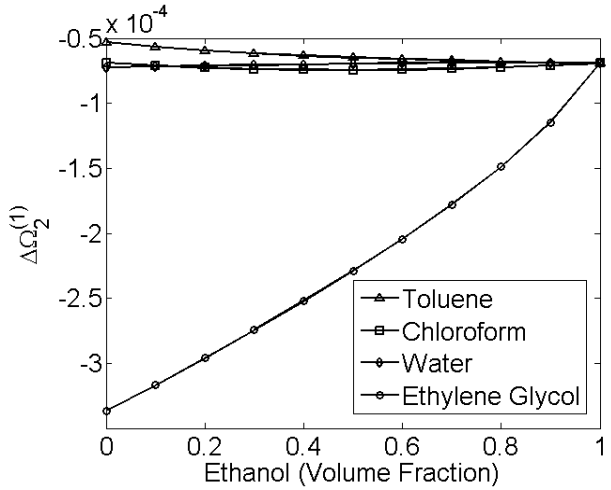

(a)

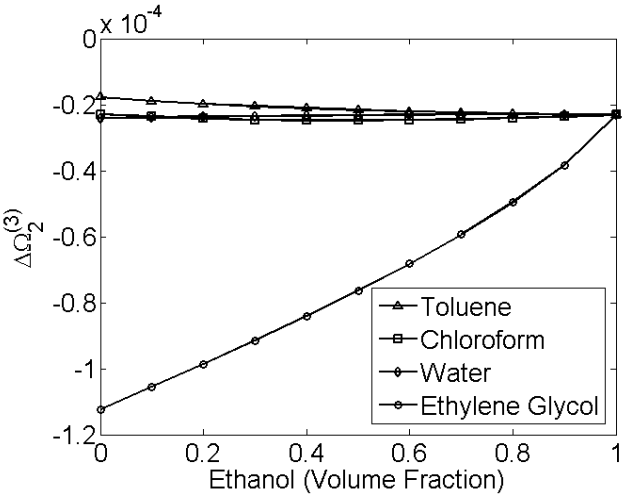

(b)

Fig. 5.3 $\Delta\Omega_2^{(n)}$ versus the volumn fraction of ethanol. (a) n=1; (b) n=3

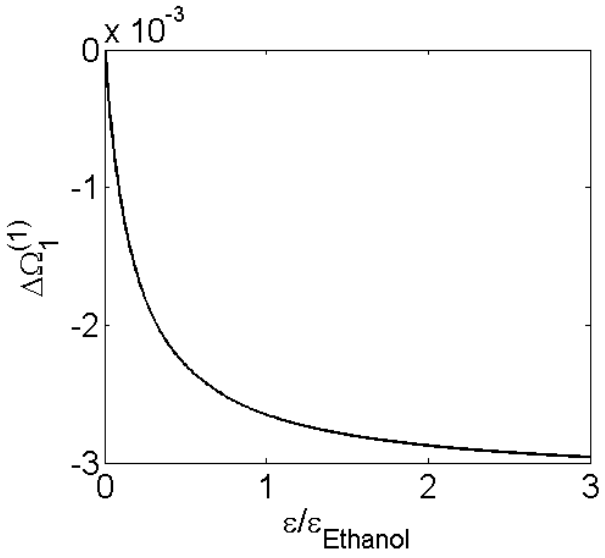

Fig. 5.4 Effects of fluid dielectric constant on $\Delta\Omega_1^{(1)}$

Fig. 5.4 is for the case when the fluid is 100% ethanol. To examine the effects of the fluid dielectric constant individually, we artificially vary the parameter and plot the result. The fluid dielectric constant lowers the frequency monotonically. The frequency is relatively more sensitive to the fluid dielectric constant when it is small.

Fig. 5.5 is also for the case when the fluid is 100% ethanol. We artificially vary the fluid density or viscosity separately. They lower the frequency as expected. These curves are simple and are convenient for viscosity or density sensing.

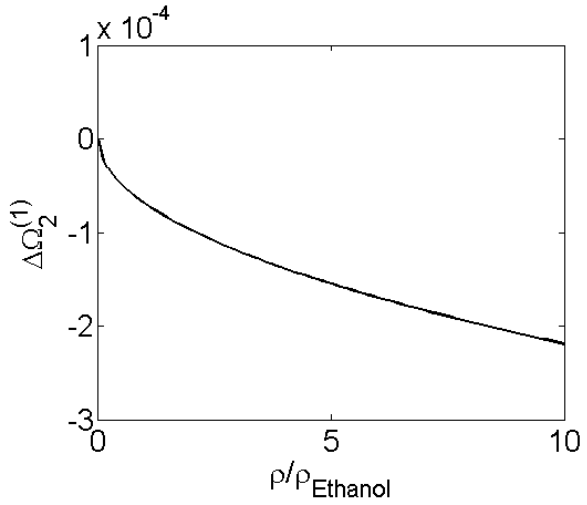

(a)

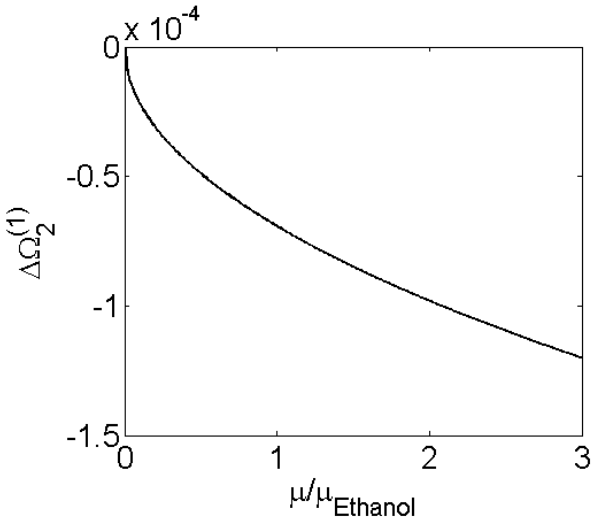

(b)

Fig. 5.5 Effects of fluid density (a) and viscosity (b) on $\Delta\Omega_2^{(1)}$

Fig. 5.6 shows the effect of the fluid layer thickness for different volume fractions of ethanol in ethylene glycol. $\Delta\Omega_1^{(1)}$ in (a) approaches a constant for large H. It is not sensitive to the volume fraction. $\Delta\Omega_2^{(1)}$ approaches a constant much quicker and it is sensitive to the volume fraction. For small H, $|\Delta\Omega_2^{(1)}|$ increases with H essentially linearly. Before it saturates, it reaches a maximum that is slightly larger than the saturation.

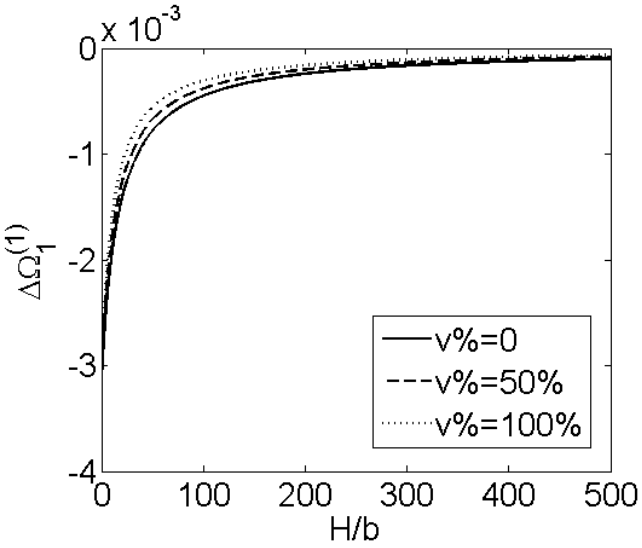

(a)

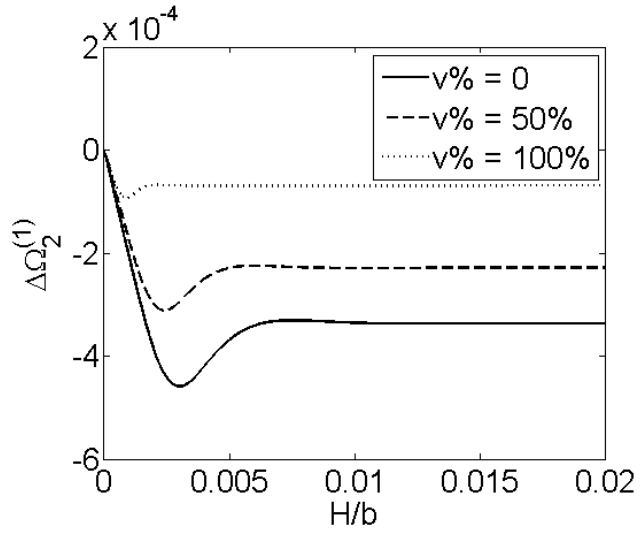

(b)

Fig. 5.6 Effect of fluid layer thickness on $\Delta\Omega_1^{(1)}$ (a) and $\Delta\Omega_2^{(1)}$ (b) for different volume fractions of ethanol in ethylene glycol

Fig. 5.7 is from the forced vibration analysis. It shows the admittance per unit plate surface area of the structure for different volume fractions of ethanol in toluene. (a) shows an isolated resonance which is ideal for resonant acoustic wave sensors. (b) is a magnified picture of (a) locally near resonance. When the volume fraction of ethanol increases from 0 to 100%, Fig. 5.7 (b) shows that the corresponding frequency change is of the order of 10^{-3}. With a frequency resolution of 10^{-5}, the ethanol concentration can be determined with an accuracy of 1%.

In the above figures, the relative frequency shift is of the order of 10^{-4} to 10^{-3} in general. This is considered strong and clear signals because typical thermal noises in quartz resonators are of the order of 10^{-6}.

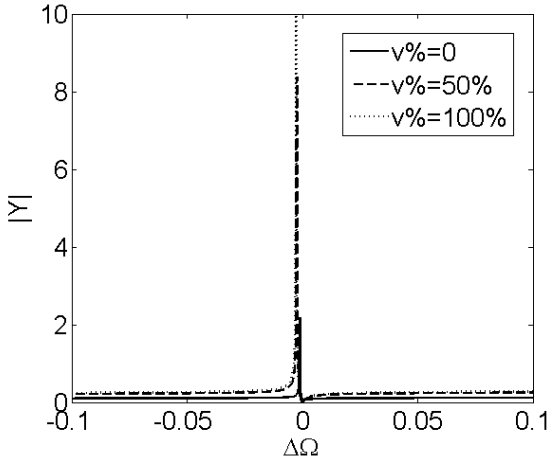

(a)

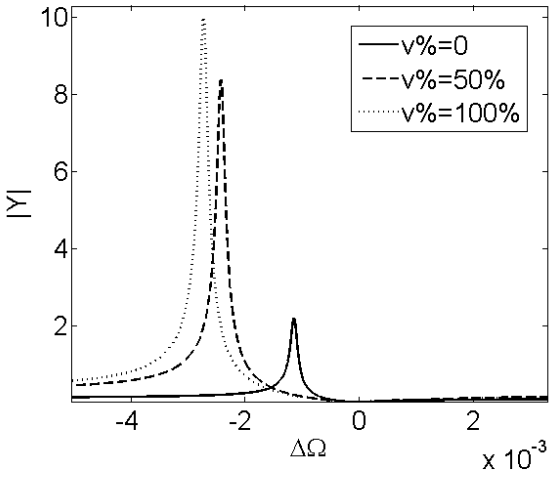

(b)

Fig. 5.7 Admittance for different volume fractions of ethanol in toluene (TFE)

5.6 Conclusion

An exact solution is obtained for thickness-shear vibrations of a rotated Y-cut quartz plate in contact with a fluid driven by a thickness electric field. An approximate expression for the frequency shifts due to the fluid is presented. The expression contains two parts. One is exactly what we got in last chapter and includes the classical result in [11] as a special case. The other is related to the permittivity of the fluid. The fluid permittivity, density and viscosity tend to lower the frequencies of the crystal plate. The frequency shift caused by the fluid permittivity is approximately one-order larger than the frequency shift caused by the fluid density and viscosity. These results show the same tendency given by the experimental results in [1]. Furthermore, the higher-order modes are less sensitive to the fluid than lower-order modes. The results obtained are fundamental and useful for the understanding and design of quartz crystal fluid sensors driven by lateral electric fields.

5.7 References

[1] Y. H. Hu, L. A. French, Jr., K. Radecsky, M. P. da Gunha, P. Millard and J. F. Vetelino, "A lateral field excited liquid acoustic wave sensor," IEEE Trans. Ultrason., Ferroelec., Freq. Contr., 51(11), 1373-1380, 2004.

[2] D. F. McCann, L. A. French Jr., M. S Wark and J. F Vetelino, "Recent advances in lateral field excited and monolithic spiral coil acoustic transduction bulk acoustic wave sensor platforms," Meas. Sci. Technol. 20, 124001, 2009

[3] U. Hempel, R. Lucklum, P. R. Hauptmann, E. P. EerNisse, D. Puccio and R. Fernandez Diaz, "Quartz crystal resonator sensors under lateral field excitation—a theoretical and experimental analysis," Meas. Sci. Technol., 19, 055201, 2008

[4] J. G. Miller and D. J. Bolef, "Acoustic wave analysis of the operation of quartz-crystal film-thickness monitors," J. Appl Phys. 39, 5815-5816, 1968.

[5] F. Boersma and E. C. van Ballegooyen, "Rotated Y-cut quartz crystal with two different electrodes treated as a one-dimensional acoustic composite resonator," J. Acoust. Soc. Am., 62(5-2), 335-340, 1977.

[6] R. L. Panton, "Incompressible Flow," John Wiley and Sons, New York, 1984

[7] F. Josse, Z. A. Shana, D. E. Radtke and D. T. Haworth, "Analysis of piezoelectric bulk-acoustic- wave resonators as detectors in viscous conductive liquids," IEEE Trans. Ultrason., Ferroelec., Freq. Contr., 37, 359-368, 1990.

[8] R. Holland, "Representation of dielectric, elastic, and piezoelectric losses by complex coefficients," IEEE Trans. on Sonics and Ultrasonics, 14, 18-20, 1967.

[9] H. F. Tiersten, "On the necessity of including electrical conductivity in the description of piezoelectric fracture in real materials," IEEE Trans. Ultrason., Ferroelec., Freq. Contr., 45(11), 1-3, 1998.

[10] H. F. Tiersten, "Linear Piezoelectric Plate Vibrations", Plenum, New York, 1969.

[11] K. K. Kanazawa and J. G. Gordon II, "The oscillation frequency of a quartz resonator in contact with a liquid," Analytica Chimica Acta, 175, 99-105, 1985.

[12] Z. T. Yang, S. H. Guo, Y. T. Hu and J. S. Yang, "Thickness-shear vibration of rotated y-cut quartz plates with unattached electrodes and asymmetric air gaps," Philosophical Magazine Letters, 89(5), 313-321, 2009.

6. Propagation of Shear-horizontal Waves in a Quartz Crystal Plate Carrying a Fluid Layer of Finite Thickness

6.1 Introduction

Certain shear modes in plates called thickness-shear (TSh) are widely used for fluid sensor applications [1-3]. Theoretically these modes can only exist in unbounded plates without edge effects. In these modes, motions of material particles are parallel to the surfaces of the plates, and particle velocities only vary along the plate thickness direction, without in-plane variations. From the viewpoint of wave propagation, TSh modes in a plate are waves propagating along the thickness direction of the plate and are bounced back and forth between the surfaces of the plate. The wave vector is parallel to the plate thickness direction, and the in-plane wave numbers are zero or the in-plane wave lengths are infinite. These TSh waves or modes are the idealized operating modes of many acoustic wave devices.

In reality, however, due to the finite size of devices, pure TSh modes cannot exist because of edge effects. Therefore, in real devices, usually the operating modes are in fact related to waves whose wave vectors have a small in-plane component. These waves have been referred to as essentially TSh waves, or transversely varying TSh waves. In the case when the transverse variation is in a direction perpendicular to the TSh particle velocity, the corresponding waves are called thickness-twist (TT) waves. These transversely varying waves are long waves in plates whose in-plane wave lengths are much larger than the plate thickness. Both stationary waves in resonators and propagating

waves in waveguides have been used for resonators and sensors. Understanding the behavior of long waves in plates is fundamentally important to plate acoustic wave devices.

The propagation of waves in crystal plates, elastic or piezoelectric, has been an active research subject for a long time [4-9]. In particular, waves in plates in contact with a fluid have been studied for fluid sensor applications, e.g., [10, 11]. Due to material anisotropy, modeling of crystal devices using the three-dimensional (6-3D) theory of elasticity or piezoelectricity usually involves considerable mathematical difficulties. In fluid sensor applications, this is further complicated by the fluid-structure interaction. Although long equations for determining the wave dispersion relations can often be formulated, they are typically involved with transcendental equations with multi-valued solutions and complex roots. Therefore numerical searches for the roots of the frequency equations are usually needed which still present various challenges even today with high speed computers. Sometimes some of the roots are missing. Once the roots are found it may be difficult to determine which roots are on the same dispersion curve because of the presence of many branches of them, especially in the high frequency range when the roots are crowded.

In this chapter we use Mindlin's first-order plate equations to study certain SH waves in a crystal plate in contact with a viscous fluid layer. In addition to pure TSh modes, we are interested in the propagation of long waves and how they are affected by the presence of the fluid. The use of 2D plate equations simplifies the problem and allows us to obtain

some simple and fundamental analytical results useful to the understanding and design of plate wave fluid sensors.

6.2 Two-dimensional plate equations

The equations for crystal plates vary considerably according to the symmetry of the crystals. Quartz is a crystal widely used for acoustic wave devices. Therefore we focus on quartz in the following. Quartz has very weak piezoelectric coupling. For frequency analysis the small piezoelectric coupling can be neglected and an elastic analysis is usually sufficient. This is common practice in the frequency analysis of resonant quartz devices. A particular cut of a quartz plate refers to the orientation of the plate when it is taken out of an anisotropic bulk quartz crystal. As a consequence quartz plates of different cuts exhibit different anisotropies in coordinates normal and parallel to the plate surfaces. Rotated Y-cut quartz plates are effectively monoclinic. They include the most frequently used AT-cut quartz plates as a special case. In this section we summarize the 2D plate equations for rotated Y-cut quartz [12, 13].

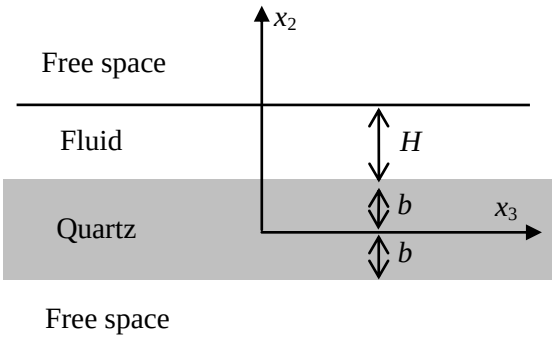

Fig. 6.1 A crystal plate with a fluid layer

Consider such a plate as shown in Fig. 6.1. It is in contact with a Newtonian fluid layer of thickness H. For rotated Y-cut quartz plates, shear-horizontal or antiplane motions with only one displacement component are allowed by the linear theory of anisotropic elasticity. These motions are particularly useful in device applications. They are described by

$$u_1 = u_1(x_2, x_3, t), \quad u_2 = u_3 = 0, \tag{6-1}$$

where **u** is the displacement vector. u_1 is governed by [14]

$$c_{66}u_{1,22} + c_{55}u_{1,33} + 2c_{56}u_{1,23} = \rho\ddot{u}_1. \tag{6-2}$$

Exact solutions to (6-2) can be attempted for relatively simple problems. Due to c_{56}, solving (6-2) is not easy and the results are usually complicated. (6-2) includes all SH modes. Since an acoustic wave device usually operates with a particular mode, it is simper to use 2D plate equations which describe the modes of interest only. The ideal operating mode is TSh which does not have x_1 and x_3 dependence. The variation of

these modes along x_1 has been reasonably well understood. Therefore this chapter is concerned with the x_3 dependence only without the x_1 dependence, the so-called straight-crested waves or modes. For straight-crested SH motions, the displacement field of the first-order plate theory is approximated by [12, 13]

$$u_1(x_2, x_3, t) = u_1^{(0)}(x_3, t) + x_2 u_1^{(1)}(x_3, t) \tag{6-3}$$

where $u_1^{(0)}(x_3, t)$ is the face-shear (FS) displacement, and $u_1^{(1)}(x_3, t)$ is the fundamental TT displacement. When $u_1^{(1)}(x_3, t)$ is independent of x_3, it reduces to the fundamental TSh which is the ideal mode of an infinite plate. Both $u_1^{(0)}$ and $u_1^{(1)}$ have tangential surface displacements only and are very useful for fluid sensor application. They are governed by the following plate equations of motion [12, 13]:

$$T_{31,3}^{(0)} + 2bT_1^{(0)} = 2b\rho\ddot{u}_1^{(0)}, \tag{6-4a}$$

$$T_{31,3}^{(1)} - T_{21}^{(0)} + \frac{2b^3}{3}T_1^{(1)} = \frac{2b^3}{3}\rho\ddot{u}_1^{(1)}. \tag{6-4b}$$

The plate resultants $T_{31}^{(0)}$, $T_{21}^{(0)}$ and $T_{31}^{(1)}$ represent plate internal forces and moments. They are related to the plate displacements $u_1^{(0)}$ and $u_1^{(1)}$ by the following constitutive relations [12, 13]:

$$T_{31}^{(0)} = 2b(c_{55}u_{1,3}^{(0)} + \kappa_1 c_{56}u_1^{(1)}), \tag{6-5a}$$

$$T_{12}^{(0)} = 2b(\kappa_1 c_{56}u_{1,3}^{(0)} + \kappa_1^2 c_{66}u_1^{(1)}), \tag{6-5b}$$

$$T_{31}^{(1)} = \frac{2b^3}{3}(\gamma_{55}u_{1,3}^{(1)} + \psi_{35}\phi_{,3}^{(1)}), \tag{6-5c}$$

where c_{pq} is the usual elastic stiffness, $\gamma_{55}=1/s_{55}$, and s_{pq} is the elastic compliance. κ_1 in the above equations is a shear correction factor [12, 13] which will be determined later. The mechanical surface loads in (6-4) are defined by

$$\begin{aligned} T_1^{(0)} &= \frac{1}{2b}\left[T_{21}\left(b^-\right)-T_{21}\left(-b^-\right)\right], \\ T_1^{(1)} &= \frac{3}{2b^3}\left[bT_{21}\left(b^-\right)+bT_{21}\left(-b^-\right)\right] \ , \end{aligned} \tag{6-6}$$

where b^- is the lower limit of b. Substitution of (6-5) into (6-4) gives two equations for $u_1^{(0)}$ and $u_1^{(1)}$:

$$c_{55}u_{1,33}^{(0)}+\kappa_1 c_{56}u_{1,3}^{(1)}+T_1^{(0)}=\rho\ddot{u}_1^{(0)}\ , \tag{6-7a}$$

$$\gamma_{55}u_{1,33}^{(1)}-3b^{-2}(\kappa_1 c_{56}u_{1,3}^{(0)}+\kappa_1^2 c_{66}u_1^{(1)})+T_1^{(1)}=\rho\ddot{u}_1^{(1)}\ . \tag{6-7b}$$

Clearly, c_{56} causes the coupling between $u_1^{(0)}$ and $u_1^{(1)}$. Therefore a coupled analysis is necessary. (6-7) has spatial derivatives with respective to x_3 only but not x_2 due to the plate approximation, and therefore is much simpler than (6-1).

6.3 Thickness-shear vibration

The shear correction factor κ_1 in the plate equations in the previous section is determined by requiring the resonant frequencies of the fundamental TSh mode calculated from the 3D exact equations and the 2D plate equations to be the same [12, 13]. The relevant 3D solution was given in Chapter 4. In this section we calculate the 2D solution and determine κ_1.

Consider the unbounded plate in Fig. 6.1. Whether the fluid is compressible or not does not matter because the motion to be considered is a pure shear without volume change. For time-harmonic motions we use the usual complex notation. All fields have the same $\exp(i\omega t)$ factor which will be dropped later for simplicity.

6.3.1 Fluid

The equation of motion for the fluid is [15]

$$T_{21,2} = \rho_L \dot{v}_1 , \tag{6-8}$$

where the shear stress is given by

$$T_{21} = \mu \frac{\partial v_1}{\partial x_2} \ . \tag{6-9}$$

μ and ρ_L are the viscosity and mass density of the fluid. v_1 and T_{21} are the relevant velocity and shear stress components. The velocity field can be determined as

$$v_1 = \{C_1 \sinh[(1+i)\eta(x_2 - b)] + C_2 \cosh[(1+i)\eta(x_2 - b)]\}, \tag{6-10}$$

where C_1 and C_2 are undetermined constants, and

$$\eta = \sqrt{\frac{\rho_L \omega}{2\mu}} \ . \tag{6-11}$$

The shear stress needed for boundary and continuity conditions is

$$T_{21} = (1+i)\mu\eta\{C_1 \cosh[(1+i)\eta(x_2 - b)] + C_2 \sinh[(1+i)\eta(x_2 - b)]\}. \tag{6-12}$$

6.3.2 Crystal Plate

For thickness vibrations independent of x_3, with the use of (6-6), (6-7) reduces to

$$\begin{aligned} &\frac{1}{2b}\left[T_{21}\left(b^-\right) - T_{21}\left(-b^-\right)\right] = \rho\ddot{u}_1^{(0)}, \\ &-3b^{-2}\kappa_1^2 c_{66} u_1^{(1)} + \frac{3}{2b^3}\left[bT_{21}\left(b^-\right) + bT_{21}\left(-b^-\right)\right] = \rho\ddot{u}_1^{(1)}. \end{aligned} \tag{6-13}$$

The bottom of the plate surface is traction free, with $T_{21}(-b^-) = 0$. At the top of the plate the shear stress is continuous, i.e., $T_{21}(b^-) = T_{21}(b^+)$ where b^+ is the upper limit of b. With these (6-13) becomes

$$\begin{aligned} &\frac{1}{2b}T_{21}\left(b^+\right) = \rho\ddot{u}_1^{(0)}, \\ &-3b^{-2}\kappa_1^2 c_{66} u_1^{(1)} + \frac{3}{2b^2}T_{21}\left(b^+\right) = \rho\ddot{u}_1^{(1)}. \end{aligned} \tag{6-14}$$

We let

$$u_1^{(0)} = C_3 \exp(i\omega t), \quad u_1^{(1)} = C_4 \exp(i\omega t) \tag{6-15}$$

where C_3 and C_4 are undetermined constants.

6.3.3 Boundary and Continuity Conditions

At the top of the fluid layer, we have the following traction-free condition:

$$T_{21}\left(b+H\right)=0\ . \tag{6-16}$$

At the interface between the crystal plate and the fluid, we have the continuity of particle velocity:

$$\dot{u}_1^{(0)}+b\dot{u}_1^{(1)}=v_1\left(b^+\right)\ . \tag{6-17}$$

Substituting the relevant fields in (6-10), (6-12), and (6-15) into (6-14), (6-16) and (6-17) results in four linear and homogeneous equations for C_1 through C_4:

$$\begin{aligned}
&\cosh\left[(1+i)\eta H\right]C_1+\sinh\left[(1+i)\eta H\right]C_2=0,\\
&C_2-i\omega C_3-i\omega bC_4=0,\\
&(1+i)\mu\eta C_1+2\rho b\omega^2C_3=0,\\
&3(1+i)\mu\eta C_1+\left(2\rho b^2\omega^2-6\kappa_1^2c_{66}\right)C_4=0.
\end{aligned} \tag{6-18}$$

For nontrivial solutions the determinant of the coefficient matrix of (6-18) has to vanish, which gives the following frequency equation:

$$\omega^2-\frac{3\kappa_1^2c_{66}}{\rho b^2}=\frac{(1-i)\mu\eta}{2\rho b\omega}\left(\frac{3\kappa_1^2c_{66}}{\rho b^2}-4\omega^2\right)\tanh\left[(1+i)\eta H\right]. \tag{6-19}$$

6.3.4 Correction Factor

The exact fundamental TSh frequency from the 3D equations when the fluid is not present is given by [16]

$$\omega_0 = \frac{\pi}{2b}\sqrt{\frac{c_{66}}{\rho}}\,. \tag{6-20}$$

When the plate is in contact with a low viscosity fluid layer, the fundamental TSh frequency is approximately given by Chapter 4

$$\omega = \omega_0(1+\Delta\Omega)\,, \tag{6-21}$$

where

$$\Delta\Omega = -\frac{1-i}{\pi}\sqrt{\frac{\rho_L\mu\omega_0}{2\rho c_{66}}}\tanh[(1+i)\eta_0 H]\,, \tag{6-22}$$

$$\eta_0 = \sqrt{\rho_L\omega_0/(2\mu)}\,. \tag{6-23}$$

Substitution of (6-21) into (6-19) determines

$$\kappa_1^2 = \frac{\pi^2}{12}(1-\Delta\Omega)\,. \tag{6-24}$$

We note that (6-24) is complex. Its real part is a frequency shift. Its negative part represents damped modes due to viscosity.

6.4 Propagation of face-shear and thickness-twist waves

With κ_1 determined, the plate equations are ready to be used to study propagating waves in the plate which is the main purpose of this chapter. We begin with coupled FS and TT waves and then examine uncoupled long FS and long TT waves separately.

6.4.1 Coupled waves

For propagating waves with both x_2 and x_3 dependence, the equations for the fluid are

$$\begin{aligned} &T_{21,2} + T_{31,3} = \rho_L \dot{v}_1, \\ &T_{21} = \mu \frac{\partial v_1}{\partial x_2}, \quad T_{31} = \mu \frac{\partial v_1}{\partial x_3}. \end{aligned} \tag{6-25}$$

Substituting the stresses into the equation of motion gives

$$\mu(v_{1,22} + v_{1,33}) = \rho_L \dot{v}_1 \ . \tag{6-26}$$

We consider the following propagating waves:

$$v_1 = \left\{ C_1 \sinh\left[\sqrt{\zeta^2 - 2i\eta^2}\,(x_2 - b)\right] + C_2 \cosh\left[\sqrt{\zeta^2 - 2i\eta^2}\,(x_2 - b)\right] \right\} \exp[i(\zeta x_3 - \omega t)] \ , \tag{6-27}$$

where C_1 and C_2 are undetermined constants, and (6-11) is still valid. For propagating waves in the crystal plate, we have

$$\begin{aligned} &c_{55} u_{1,33}^{(0)} + \kappa_1 c_{56} u_{1,3}^{(1)} + \frac{1}{2b} T_{21}(b^+) = \rho \ddot{u}_1^{(0)}, \\ &\gamma_{55} u_{1,33}^{(1)} - 3b^{-2}(\kappa_1 c_{56} u_{1,3}^{(0)} + \kappa_1^2 c_{66} u_1^{(1)}) + \frac{3}{2b^3} T_{21}(b^+) = \rho \ddot{u}_1^{(1)}. \end{aligned} \tag{6-28}$$

At the top of the fluid layer the traction-free boundary condition in (6-16) still holds. The continuity of velocity at the top of the plate surface given by (6-17) is also still valid. Let

$$u_1^{(0)} = C_3 \exp[i(\zeta x_3 - \omega t)], \quad u_1^{(1)} = C_4 \exp[i(\zeta x_3 - \omega t)] \ , \tag{6-29}$$

where C_3 and C_4 are undetermined constants. Substitution of (6-27) and (6-29) into (6-16), (6-17) and (6-28) yields the following four linear and homogeneous equations for C_1 through C_4:

$$\begin{aligned}
&C_1 + C_2 \tanh\left(\sqrt{\zeta^2 - 2i\eta^2}\, H\right) = 0, \\
&C_2 + i\omega C_3 + ib\omega C_4 = 0, \\
&\frac{\mu\sqrt{\zeta^2 - 2i\eta^2}}{2b} C_1 + (\rho\omega^2 - c_{55}\zeta^2) C_3 + i\kappa_1 c_{56}\zeta C_4 = 0, \\
&\frac{3}{2}\mu\sqrt{\zeta^2 - 2i\eta^2}\, C_1 - 3i\kappa_1 c_{56}\zeta C_3 + (\rho b^2\omega^2 - \gamma_{55} b^2\zeta^2 - 3\kappa_1^2 c_{66}) C_4 = 0.
\end{aligned} \tag{6-30}$$

For nontrivial solutions the determinant of the coefficient matrix has to vanish, which, together with (6-11), gives the flowing frequency equation that determines the dispersion relation of ω versus ζ:

$$\begin{aligned}
&(iAB\omega + \rho\omega^2 - c_{55}\zeta^2)(3iABb^2\omega + \rho b^2\omega^2 - \gamma_{55} b^2\zeta^2 - 3\kappa_1^2 c_{66}) \\
&\quad - (iABb\omega + i\kappa_1 c_{56}\zeta)(3iABb\omega - 3i\kappa_1 c_{56}\zeta) = 0,
\end{aligned} \tag{6-31}$$

where

$$A = \frac{\mu\sqrt{\zeta^2 - 2i\eta^2}}{2b}, \quad B = \tanh\left(\sqrt{\zeta^2 - 2i\eta^2}\, H\right). \tag{6-32}$$

In device applications usually long waves with a small or infinitesimal ζ are used. Therefore we expand the relevant terms in (6-31) into power series of ζ and neglect powers higher than two. Then (6-31) can be written as

$$F(\omega)\zeta^2 + G(\omega) = 0, \tag{6-33}$$

where

$$
\begin{aligned}
F(\omega) &= 4A_1B_2i\rho b^2\omega^3 + 4A_2B_1i\rho b^2\omega^{5/2} - A_1B_1i\gamma_{55}b^2\omega^{3/2} \\
&\quad -3A_1B_2i\kappa_1^2c_{66}\omega - 3A_2B_1i\kappa_1^2c_{66}\omega^{1/2} - 3A_1B_1ic_{55}b^2\omega^{3/2} \\
&\quad -\gamma_{55}\rho b^2\omega^2 - c_{55}\rho b^2\omega^2 + 3\kappa_1^2c_{66}c_{55} - 3\kappa_1^2c_{56}^2, \\
G(\omega) &= 4A_1B_1i\rho b^2\omega^{7/2} - 3A_1B_1i\kappa_1^2c_{66}\omega^{3/2} + \rho^2b^2\omega^4 - 3\kappa_1^2c_{66}\rho\omega^2,
\end{aligned}
\tag{6-34}
$$

and

$$
\begin{aligned}
&A_1 = \frac{1}{2b}\sqrt{-i\mu\rho_L}, \quad A_2 = \frac{1}{4b}\sqrt{\frac{i\mu^3}{\rho_L}}, \\
&B_1(\omega) = \tanh\left(\sqrt{-2i\eta^2}H\right), \quad B_2(\omega) = \frac{H\left[1-\tanh^2\left(\sqrt{-2i\eta^2}H\right)\right]}{2}\sqrt{\frac{i\mu}{\rho_L}}.
\end{aligned}
\tag{6-35}
$$

In the special case when the fluid is not present, for thickness modes with ζ=0, (6-33) determines two frequencies of 0 and ω_0. For small but nonzero values of ζ, (6-34) determines two dispersion relations for FS and TT waves. The FS branch goes through the origin $(\omega,\zeta)=(0,0)$. The TT branch has a finite intercept at $(\omega,\zeta)=(\omega_0,0)$ and ω_0 is called the cutoff frequency below which the TT wave becomes exponential in x_3 and cannot propagate. When the fluid is present, for low-viscosity fluids, we expect the two branches are modified slightly and discuss them separately below.

6.4.2 Long FS Waves

For the FS branch, when ζ is small, ω is also small and is of the same order (see [17] for the case when the fluid is not present). In this case, neglecting higher powers of ω, (6-34) can be approximated by

$$(3\kappa_1^2 c_{66}c_{55} - 3\kappa_1^2 c_{56}^2)\zeta^2 = 3\kappa_1^2 c_{66}\rho\omega^2 + 3A_1B_1 i\kappa_1^2 c_{66}\omega^{3/2}, \tag{6-36}$$

where the effect of the fluid is represented by the second term on the right-hand side. When the fluid is not present and the crystal plate is alone, denoting the wave frequency by ω_{Plate}, (6-36) reduces to the following known dispersion relation for long FS waves [17]:

$$\omega_{\text{Plate}} = \sqrt{\frac{c_{66}c_{55} - c_{56}^2}{\rho c_{66}}}\,\zeta = \sqrt{\frac{\gamma_{55}}{\rho}}\,\zeta, \tag{6-37}$$

which is nondispersive. An immediate observation is that the second term on the right-hand side of (6-36) makes the waves dispersive. For numerical results an AT-cut quartz plate with *b*=1mm is used, which is a typical thickness for quartz devices. For the fluid we choose as an example chloroform with $\rho_L = 1.483\times10^3\,\text{kg/m}^3$ and a relatively low viscosity of $\mu = 0.542\,\text{mPas}$ (smaller than the viscosity of water). We consider real frequencies and solve (6-36) for complex wave numbers. For figure plotting we introduce the following dimensionless frequencies and wave number:

$$\Omega = \frac{\omega}{\omega_0}, \quad \Omega_{\text{Plate}} = \frac{\omega_{\text{Plate}}}{\omega_0}, \quad Z = \frac{\zeta}{\pi/(2b)} = X + iY. \tag{6-38}$$

Long waves are described by small values of the real part *Z*.

Figure 2 shows the effect of viscosity on the dispersion relation of long FS waves. The viscosity of chloroform is artificially varied while other parameters are fixed. Fig. 6.2 (a) shows a fundamental and qualitative effect of the fluid viscosity which changes

the dispersion curve from real to complex indicating attenuation due to fluid viscosity, and from a straight line to a curve showing dispersion. Fig. 6.2 (b) shows the real part of the dispersion relation which is essentially linear and hence the fluid induced dispersion is small. Fig. 6.2 (c) shows the difference between the real part of (6-36) and (6-37), in which the fluid induced dispersion becomes visible. It can be seen from Fig. 6.2 (c) that, although long waves are usually used in real devices, the frequency shift is larger when the wave number X is larger or the wave is shorter. This is because shorter waves have lager velocity gradients in the x_3 direction and hence a larger viscous stress T_{31}. Fig. 6.2 (c) also shows that the fluid lowers the frequency, and higher viscosity causes more frequency shift. The relative frequency shift is of the order of 10^{-5} which is considered a significant frequency change because the thermal noise in crystal resonators is typically of the order of 10^{-6}. Therefore a 10^{-5} frequency shift is a clear and measurable signal. Fig. 6.2 (d) shows the imaginary part of the complex wave number. It is positive, representing attenuation for the right-traveling waves given in (6-29). For a fixed frequency, higher viscosity causes larger attenuation.

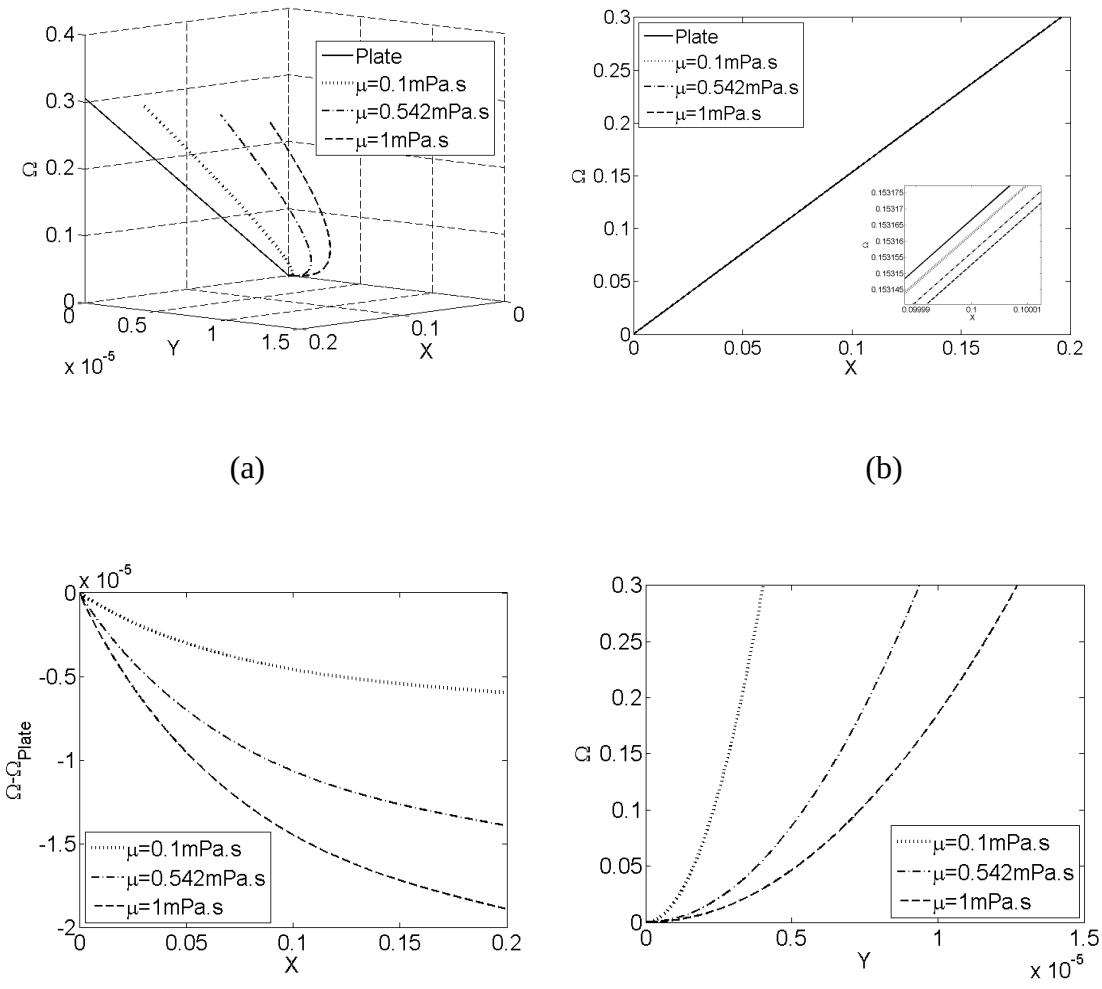

Fig. 6.2 Effects of fluid viscosity on FS waves, H=2b.

Figure 3 shows the effect of the fluid density. The behaviors in Fig. 6.3 are similar to those in Fig. 6.2. This is as expected because, as shown in (6-22), the fluid viscosity and density appear together in a product in the first-order approximation of the frequency shift. In a typical application, one needs to know either the fluid density or viscosity and then uses an acoustic wave fluid sensor to measure the other. How to separate the density from viscosity still remains a challenging problem in acoustic wave fluid sensors.

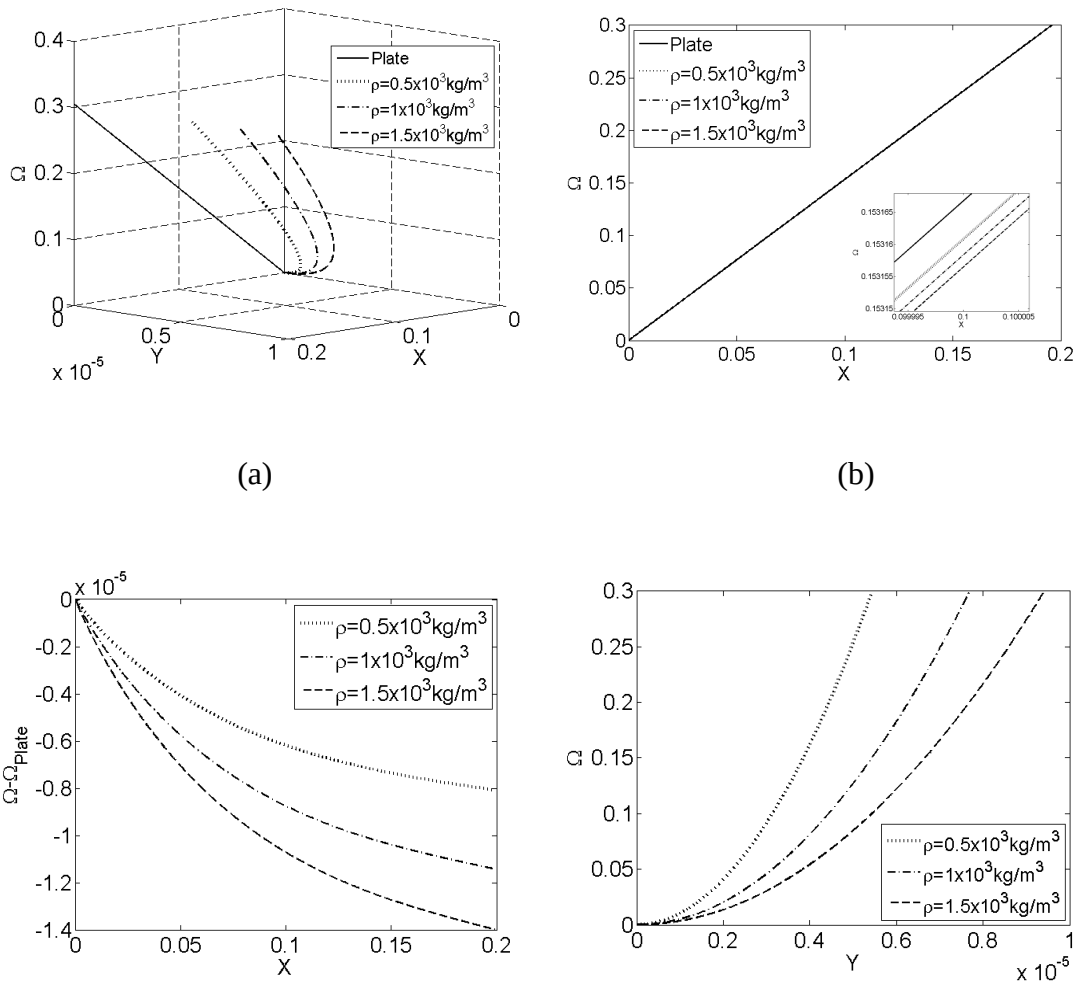

Fig. 6.3 Effects of fluid density on FS waves, H=2b.

Figure 4 shows the effect of the fluid layer thickness H. The cases of H=0.5b and H=1b are indistinguishable in the figure. In this case effectively the fluid layer can be treated as a semi-infinite half space. The frequency shift is an increasing function of H for small H only (Chapter 4). When H reaches a certain value, there exists a maximal frequency shift after which the frequency shift decreases with H (Chapter 4). What is shown in Fig. 6.4 (c) is the case when a larger H has a smaller frequency shift.

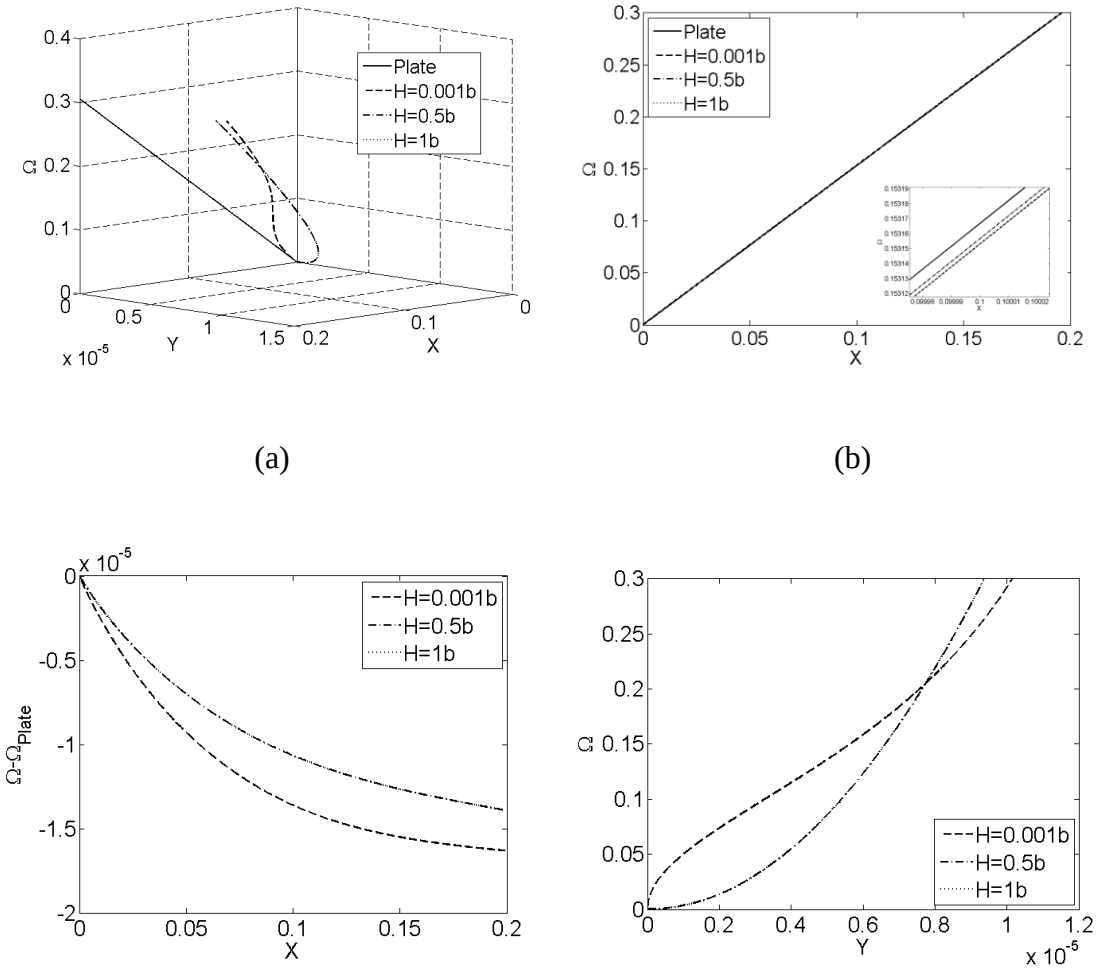

Fig. 6.4 Effects of fluid layer thickness on FS waves (H=0.5b and H=1b overlap).

6.4.3 Long TT Waves

For the TT branch, when ζ is small, ω is finite. In this case, we denote

$$\omega = \omega_0 (1 + \Delta\Omega), \tag{6-39}$$

where $\Delta\Omega$ is small. Substituting (6-39) into (6-31), for small $\Delta\Omega$, we obtain

$$\frac{\omega - \omega_0}{\omega_0} = \Delta\Omega = -\frac{D_3}{D_4} - \frac{D_1 D_4 - D_2 D_3}{D_4^2}\zeta^2, \tag{6-40}$$

where

$$\begin{aligned}
D_1 &= 4A_1 B_2^0 i\rho b^2 \omega_0^3 + 4A_2 B_1^0 i\rho b^2 \omega_0^{5/2} - A_1 B_1^0 i\gamma_{55} b^2 \omega_0^{3/2} \\
&\quad - 3A_1 B_2^0 i\kappa_1^2 c_{66}\omega_0 - 3A_2 B_1^0 i\kappa_1^2 c_{66}\omega_0^{1/2} - \gamma_{55}\rho b^2 \omega_0^2 - 3A_1 B_1^0 i c_{55} b^2 \omega_0^{3/2} \\
&\quad - c_{55}\rho b^2 \omega_0^2 + 3\kappa_1^2 c_{66} c_{55} - 3\kappa_1^2 c_{56}^2, \\
D_2 &= 12A_1 B_2^0 i\rho b^2 \omega_0^3 + 10A_2 B_1^0 i\rho b^2 \omega_0^{5/2} - \frac{3}{2} A_1 B_1^0 i\gamma_{55} b^2 \omega_0^{3/2} - 3A_1 B_2^0 i\kappa_1^2 c_{66}\omega_0 \\
&\quad - \frac{3}{2} A_2 B_1^0 i\kappa_1^2 c_{66}\omega_0^{1/2} - 2\gamma_{55}\rho b^2 \omega_0^2 - \frac{9}{2} A_1 B_1^0 i c_{55} b^2 \omega_0^{3/2} - 2c_{55}\rho b^2 \omega_0^2, \\
D_3 &= 4A_1 B_1^0 i\rho b^2 \omega_0^{7/2} - 3A_1 B_1^0 i\kappa_1^2 c_{66}\omega_0^{3/2} + \rho^2 b^2 \omega_0^4 - 3\kappa_1^2 c_{66}\rho\omega_0^2, \\
D_4 &= 14A_1 B_1^0 i\rho b^2 \omega_0^{7/2} - \frac{9}{2} A_1 B_1^0 i\kappa_1^2 c_{66}\omega_0^{3/2} + 4\rho^2 b^2 \omega_0^4 - 6\kappa_1^2 c_{66}\rho\omega_0^2.
\end{aligned} \tag{6-41}$$

In (6-41), for low-viscosity fluids, since B_1 and B_2 are always multiplied with A_1 or A_2 which depend on μ, B_1 and B_2 have been approximated by

$$B_1^0(\omega) \cong B_1(\omega_0), \quad B_2^0(\omega) \cong B_2(\omega_0). \tag{6-42}$$

(6-40) shows that locally, near cutoff, the dispersion curve can be approximated by a parabola and therefore long TT waves are dispersive. When $\zeta = 0$, (6-40) reduces to

$$\omega = \omega_0 \left(1 - \frac{D_3}{D_4} \right), \tag{6-43}$$

which is complex. Numerical results for the effects of fluid viscosity, density, and layer thickness on long TT waves are shown in Figs. 5, 6, and 7, respectively. When there is no fluid, part of the dispersion curve of TT waves is real and the rest is pure imaginary. The dispersion curve does not go through the origin. It has a finite intercept with the Ω axis which is the cutoff frequency. The basic effects of the fluid on long TT waves are similar to the case of FS waves. The dispersion curve becomes complex. TT waves are with higher frequencies than FS waves and therefore decay faster in the fluid.

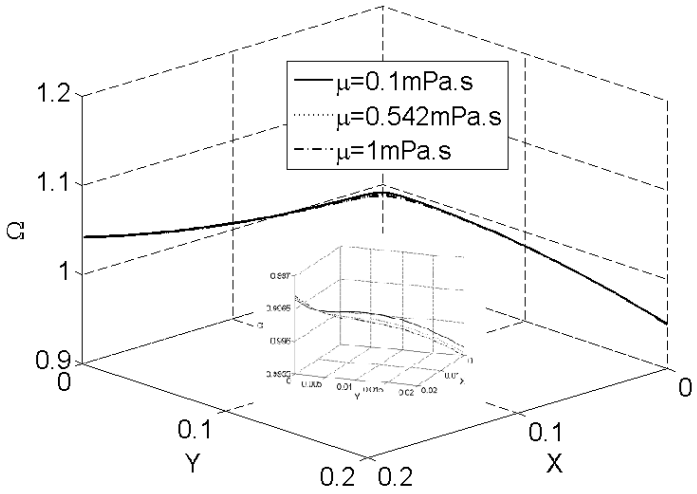

(a)

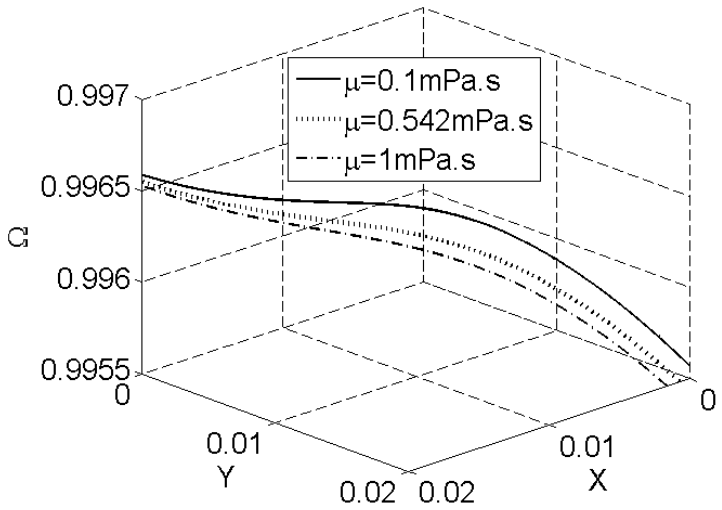

(b)

Fig. 6.5 Effects of fluid viscosity on TT waves, H=2b.

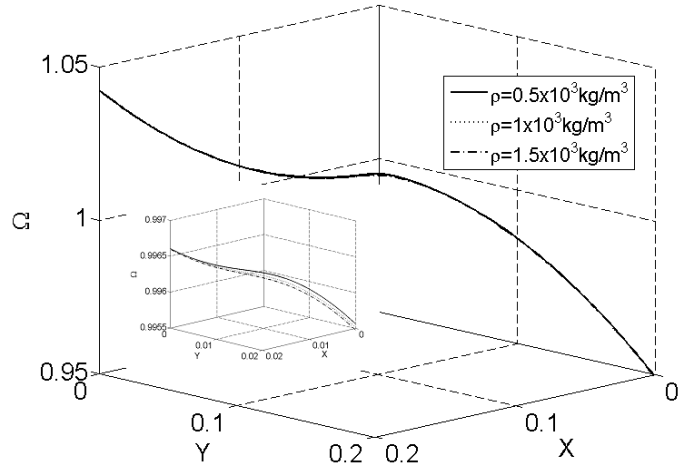

(a)

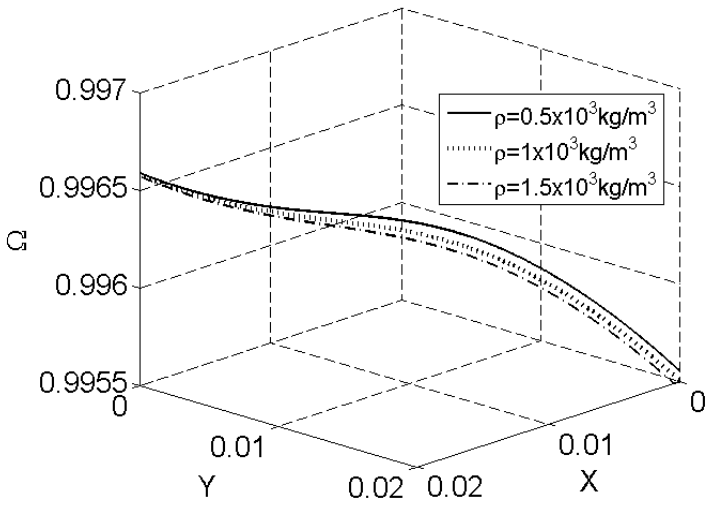

(b)

Fig. 6.6 Effects of fluid density on TT waves, H=2b.

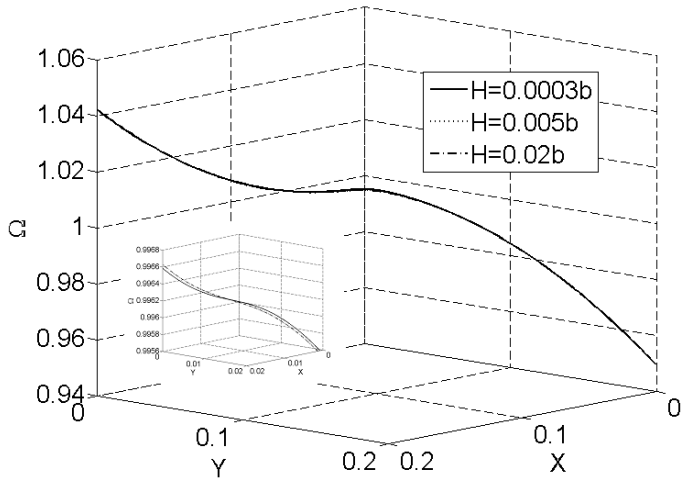

(a)

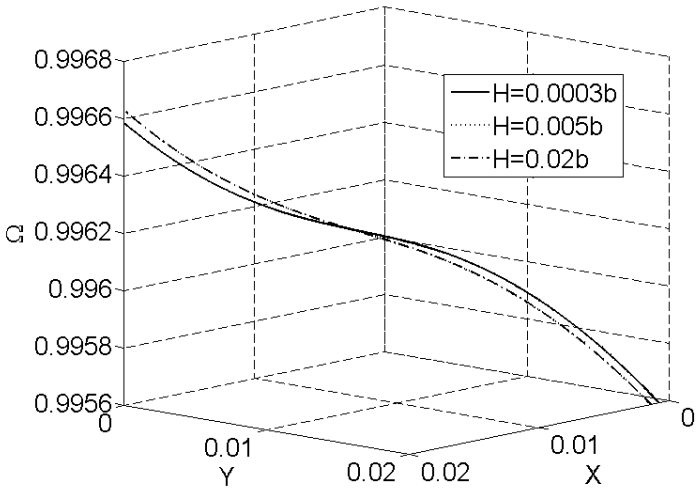

(b)

Fig. 6.7 Effects of fluid layer thickness on TT waves (H=0.005b and H=0.02b overlap).

6.5 Conclusion

Analytical solutions are obtained for TSh modes and FS as well as TT waves in a crystal plate carrying a viscous fluid layer. Approximate expressions for frequency shifts and dispersion relations are presented. The frequencies and dispersion relations become complex due to the fluid, indicating damped modes and waves with attenuation. The fluid viscosity and density lower the frequencies together in a combined manner, causing (additional) dispersion. Shorter waves tend to have larger frequency shifts. Long FS waves become dispersive due to the fluid. Typical relative frequency shifts are of the order of 10^{-5} which is detectable by crystal resonators and waveguides. The results obtained are fundamental and useful for the understanding and design of quartz crystal fluid sensors.

6.6 References

[1] K. K. Kanazawa and J. G. Gordon II, "The oscillation frequency of a quartz resonator in contact with a liquid," Analytica Chimica Acta, 175, 99-105, 1985.

[2] F. Josse, Z. A. Shana, D. E. Radtke and D. T. Haworth, "Analysis of piezoelectric bulk-acoustic- wave resonators as detectors in viscous conductive liquids," IEEE Trans. Ultrason., Ferroelec., Freq. Contr., 37, 359-368, 1990.

[3] C. E. Reed, K. K. Kanazawa and J. H. Haufman, "Physical description of a viscoelastically loaded AT-cut quartz resonator," J. Apl. Phys., 68, 1993-2001, 1990.

[4] Bleustein, J.L., "Some simple modes of wave propagation in an infinite piezoelectric plate," Journal of Acoustical Society of Amermican, 45, 614-620, 1969.

[5] Schmidt, G.H., "a. On anti-symmetric waves in an unbounded piezoelectric plate with axisymmetric electrodes," International Journal of Solids and Structures 13, 179-195, 1977

[6] Schmidt, G.H., b. "Resonances of an unbounded piezoelectric plate with circular electrodes," Paul, H.S., 1977

[7] H. S. Paul, D. P. Raju and T. R. Balakrishnan, "Free vibrations of a piezoelectric layer of hexagonal (6mm) class," International Journal of Engineering Science, 21, 691-704. International Journal of Engineering Science. 15, 495-510, 1983

[8] S. Syngellakis and P. C. Y. Lee, "Piezoelectric wave dispersion curves for infinite anisotropic plates," J. Appl. Phys., 73(11), 7152-7161, 1993.

[9] Stewart, J.T. and Yong, Y.K., "Exact analysis of the propagation of acoustic waves in multilayered anisotropic piezoelectric plates," IEEE Transactions on Ultrasonics, Ferroelectrics, and Frequency Control, 40, 375-390, 1994

[10] Peng, F., Liu, H. and Hu, S. Y., "Love wave propagation in a layered piezoelectric structure immersed in a fluid," Key Engineering Materials, 306-308: 1211-1216, 2006.

[11] F. L. Guo and R. Sun, "Propagation of Bleustein-Gulyaev wave in 6mm piezoelectric materials loaded with viscous fluid," International Journal of Solids and Structures, 45, 3699-3710, 2008.

[12] R. D. Mindlin, "High frequency vibrations of crystal plates," Quart. Appl. Math. 19, 51-61, 1961.

[13] R. D. Mindlin, “High frequency vibrations of piezoelectric crystal plates,” Int. J. Solids Structures, 8 (7), 895-906, 1972.

[14] J. S. Yang, “An Introduction to the Theory of Piezoelectricity,” Springer, 57, 2005.

[15] R. L. Panton, “Incompressible Flow,” John Wiley and Sons, New York, 1984

[16] H. F. Tiersten, “A corrected modal representation of thickness vibrations in quartz plates and its influence on the transversely varying case,” IEEE Trans. Ultrason., Ferroelect., Freq. Contr., 50, 1436-1443, 2003

[17] R. D. Mindlin, “Face-shear waves in rotated Y-cut quartz plates,” Mechanics of the Solid State, F. P. J. Rimrott and J. Schwaighofer (eds.), University of Toronto Press, 143-145, 1968.

7. Propagation of Shear-horizontal Waves in a Piezoelectric Plate in Contact with a Semi-infinite Fluid

7.1 Introduction

In this chapter we use Mindlin's first-order plate equations to study shear-horizontal (SH) or antiplane waves in a piezoelectric plate in contact with a semi-infinite viscous fluid. The analysis applies to both quartz and langasite because they have the same crystal symmetry. In addition to pure TSh modes, we are interested in the propagation of long waves and how they are affected by the presence of the fluid. In the frequency range of interest, there are two coupled SH waves. One is the TT wave and the other is called a face-shear (FS) waves. The use of 2D plate equations simplifies the problem and allows us to obtain some fundamental results analytically. These results are useful to the understanding and design of plate wave fluid sensors.

7.2 Two-Dimensional Plate Equations

The equations for piezoelectric plates vary considerably according to the symmetry of the crystals. A particular cut of a crystal plate refers to the orientation of the plate when it is taken out of an anisotropic bulk crystal. As a consequence crystal plates of different cuts exhibit different anisotropies in coordinates normal and parallel to the plate surfaces. The widely used rotated Y-cut plates of quartz and langasite are effectively monoclinic. In this section we summarize the 2D plate equations for rotated Y-cut quartz and

langasite [1]. Consider such a plate as shown in Fig. 7.1. It is in contact with a semi-infinite Newtonian fluid.

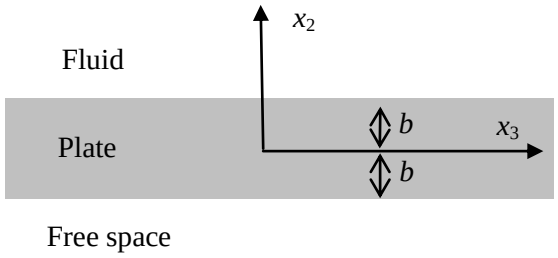

Fig. 7.1 A piezoelectric plate in contact with a semi-infinite fluid

For monoclinic piezoelectric crystals, SH or antiplane motions with only one displacement component are allowed by the linear theory of piezoelectricity [2]. These motions are particularly useful in device applications. They are described by

$$\begin{aligned} &u_1 = u_1(x_2, x_3, t), \quad u_2 = u_3 = 0, \\ &\phi = \phi(x_2, x_3, t), \end{aligned} \tag{7-1}$$

where **u** is the displacement vector and ϕ is the electric potential. u_1 and ϕ are governed by [2]

$$\begin{aligned} &c_{66}u_{1,22} + c_{55}u_{1,33} + 2c_{56}u_{1,23} \\ &\quad + e_{26}\phi_{,22} + e_{35}\phi_{,33} + (e_{25} + e_{36})\phi_{,23} = \rho\ddot{u}_1, \\ &e_{26}u_{1,22} + e_{35}u_{1,33} + (e_{25} + e_{36})u_{1,23} \\ &\quad - \varepsilon_{22}\phi_{,22} - \varepsilon_{33}\phi_{,33} - 2\varepsilon_{23}\phi_{,23} = 0. \end{aligned} \tag{7-2}$$

There are many waves governed by (7-2). In the frequency range from zero to slightly above the most widely used fundamental TSH frequency, the displacement and potential fields are approximated by [1]

$$\begin{aligned} u_1(x_2, x_3, t) &= u_1^{(0)}(x_3, t) + x_2 u_1^{(1)}(x_3, t), \\ \phi(x_2, x_3, t) &= \phi^{(0)}(x_3, t) + x_2 \phi^{(1)}(x_3, t), \end{aligned} \tag{7-3}$$

where $u_1^{(0)}(x_3, t)$ is the FS displacement, and $u_1^{(1)}(x_3, t)$ is the fundamental TT displacement with one nodal point only along the plate thickness. When $u_1^{(1)}(x_3, t)$ is independent of x_3, it reduces to the fundamental TSh mode which can exist in an infinite plate only. Both $u_1^{(0)}$ and $u_1^{(1)}$ have tangential surface displacements only and are ideal useful for fluid sensor application. $u_1^{(0)}$, $u_1^{(1)}$, $\phi^{(0)}$ and $\phi_1^{(1)}$ are governed by the following plate equations of motion and electrostatics [1]:

$$T_{31,3}^{(0)} + 2bT_1^{(0)} = 2b\rho\ddot{u}_1^{(0)}, \tag{7-4a}$$

$$T_{31,3}^{(1)} - T_{21}^{(0)} + \frac{2b^3}{3} T_1^{(1)} = \frac{2b^3}{3} \rho\ddot{u}_1^{(1)}, \tag{7-4b}$$

$$D_{3,3}^{(0)} + 2bD^{(0)} = 0, \tag{7-4c}$$

$$D_{3,3}^{(1)} - D_2^{(0)} + \frac{2b^3}{3} D^{(1)} = 0, \tag{7-4d}$$

The plate mechanical resultants $T_{31}^{(0)}$, $T_{21}^{(0)}$ and $T_{31}^{(1)}$ as well as the plate electric resultants $D_3^{(0)}$, $D_2^{(0)}$ and $D_3^{(1)}$ in (7-4) are related to the plate displacements $u_1^{(0)}$ and $u_1^{(1)}$ as well as electric potentials $\phi^{(0)}$ and $\phi^{(1)}$ by the following constitutive relations [1]:

$$T_{31}^{(0)} = 2b(c_{55}u_{1,3}^{(0)} + \kappa_1 c_{56}u_1^{(1)} + e_{25}\phi^{(1)} + e_{35}\phi_{,3}^{(0)}), \tag{7-5a}$$

$$T_{12}^{(0)} = 2b(\kappa_1 c_{56}u_{1,3}^{(0)} + \kappa_1^2 c_{66}u_1^{(1)} + \kappa_1 e_{26}\phi^{(1)} + \kappa_1 e_{36}\phi_{,3}^{(1)}), \tag{7-5b}$$

$$T_{31}^{(1)} = \frac{2b^3}{3}(\gamma_{55}u_{1,3}^{(1)} + \psi_{35}\phi_{,3}^{(1)}), \tag{7-5c}$$

$$D_2^{(0)} = 2b(e_{25}u_{1,3}^{(0)} + \kappa_1 e_{26}u_1^{(1)} - \varepsilon_{22}\phi^{(1)} - \varepsilon_{23}\phi_{,3}^{(1)}), \tag{7-5d}$$

$$D_3^{(0)} = 2b(e_{35}u_{1,3}^{(0)} + \kappa_1 e_{36}u_1^{(1)} - \varepsilon_{23}\phi^{(1)} - \varepsilon_{33}\phi_{,3}^{(0)}), \tag{7-5e}$$

$$D_3^{(1)} = \frac{2b^3}{3}(\psi_{35}u_{1,3}^{(1)} - \zeta_{33}\phi_{,3}^{(1)}) \tag{7-5f}$$

where $c_{pq}(=c_{pq}^E)$, e_{ip}, and $\varepsilon_{ij}(=\varepsilon_{ij}^S)$ are the usual elastic stiffness, piezoelectric constants, and dielectric constants. The other material constants in (7-5) are defined by

$$\begin{aligned} &\gamma_{55} = 1/s_{55}, \quad \psi_{35} = e_{35} - e_{36}c_{56}/c_{66} = d_{35}\gamma_{55}, \\ &\zeta_{33} = \varepsilon_{33} + e_{36}^2/c_{66}, \end{aligned} \tag{7-6}$$

where $s_{pq}(=s_{pq}^E)$ is the elastic compliance and d_{ip} is another set of piezoelectric constants different from but related to e_{ip} [2]. κ_1 in the above equations is a shear correction factor [1] which will be determined later. The mechanical and electric surface loads in (7-4) are defined by [1]

$$\begin{aligned} T_1^{(0)} &= \frac{1}{2b}\left[T_{21}\left(b^-\right) - T_{21}\left(-b^-\right)\right], \\ T_1^{(1)} &= \frac{3}{2b^3}\left[bT_{21}\left(b^-\right) + bT_{21}\left(-b^-\right)\right], \\ D^{(0)} &= \frac{1}{2b}\left[D_2\left(b^-\right) - D_2\left(-b^-\right)\right], \\ D^{(1)} &= \frac{3}{2b^3}\left[bD_2\left(b^-\right) + bD_2\left(-b^-\right)\right], \end{aligned} \tag{7-7}$$

where b^- is the lower limit of b. Substitution of (7-5) into (7-4) gives four equations for $u_1^{(0)}$, $u_1^{(1)}$, $\phi^{(0)}$ and $\phi^{(1)}$:

$$c_{55}u_{1,33}^{(0)} + e_{35}\phi_{,33}^{(0)} + \kappa_1 c_{56}u_{1,3}^{(1)} + e_{25}\phi_{,3}^{(1)} + T_1^{(0)} = \rho\ddot{u}_1^{(0)}, \tag{7-8a}$$

$$\gamma_{55}u_{1,33}^{(1)} + \psi_{35}\phi_{,33}^{(1)} - 3b^{-2}(\kappa_1 c_{56}u_{1,3}^{(0)} + \kappa_1^2 c_{66}u_1^{(1)} + \kappa_1 e_{26}\phi^{(1)} + \kappa_1 e_{36}\phi_{,3}^{(0)}) + T_1^{(1)} = \rho\ddot{u}_1^{(1)}, \tag{7-8b}$$

$$e_{35}u_{1,33}^{(0)} + \kappa_1 e_{36}u_{1,3}^{(1)} - \varepsilon_{33}\phi_{,33}^{(0)} - \varepsilon_{23}\phi_{,3}^{(1)} + D^{(0)} = 0, \tag{7-8c}$$

$$\psi_{35}u_{1,33}^{(1)} - \zeta_{33}\phi_{,33}^{(1)} - 3b^{-2}(e_{25}u_{1,3}^{(0)} + \kappa_1 e_{26}u_1^{(1)} - \varepsilon_{22}\phi^{(1)} - \varepsilon_{23}\phi_{,3}^{(0)}) + D^{(1)} = 0. \tag{7-8d}$$

(7-8a) and (7-8b) describe the so-called straight-crested waves propagating in the x_3 direction without x_1 dependence. (7-8c) and (7-8d) are from electrostatics. They do not describe waves but will affect the wave frequencies through piezoelectric coupling. Clearly, c_{56} causes the coupling between $u_1^{(0)}$ and $u_1^{(1)}$. Therefore a coupled analysis of FS and TT is necessary no matter which one we are interested in. (7-8) has spatial derivatives with respective to x_3 only but not x_2 due to the plate approximation and therefore is much simpler than (7-1).

7.3 Thickness-Shear Vibration

The shear correction factor κ_1 in the plate equations in the previous section is determined by requiring the resonant frequencies of the fundamental TSh mode calculated from the 3D equations of piezoelectricity and the 2D equations of piezoelectric plates to be the same. The 3D solution was given in Chapter 4. In this section we calculated the 2D solution and determine κ_1. Consider the plate in Fig. 7.1. Whether the

fluid is compressible or not does not matter because the motion to be considered is a pure shear without volume change. We consider time-harmonic motions and use the usual complex notation. All fields have the same $\exp(i\omega t)$ factor which will be dropped in the following for simplicity. The electric field in the fluid and the free space is neglected. This is a common approximation valid when the dielectric constant of the plate is larger than that of the fluid and the free space.

7.3.1 Fluid

The equation of motion for the fluid is [3]

$$T_{21,2} = \rho_L \dot{v}_1 , \tag{7-9}$$

where the shear stress is given by

$$T_{21} = \mu \frac{\partial v_1}{\partial x_2} \ . \tag{7-10}$$

μ and ρ_L are the viscosity and mass density of the fluid. v_1 and T_{21} are the relevant velocity and shear stress components. The velocity field in the fluid is

$$v_1 = C_1 \exp[-(1+i)\eta(x_2 - b)], \tag{7-11}$$

where C_1 is an undetermined constant and

$$\eta = \sqrt{\frac{\rho_L \omega}{2\mu}} \ . \tag{7-12}$$

(7-11) decays from the plate surface into the fluid. The relevant stress component needed for boundary and continuity conditions is

$$T_{21} = -(1+i)\mu\eta C_1 \exp\left[-(1+i)\eta(x_2 - b)\right]. \tag{7-13}$$

7.3.2 Crystal Plate

For thickness vibrations independent of x_3, with the use of (7-7), (7-8) reduces to

$$\begin{aligned}
&\frac{1}{2b}\left[T_{21}\left(b^-\right) - T_{21}\left(-b^-\right)\right] = \rho\ddot{u}_1^{(0)},\\
&-3b^{-2}\left(\kappa_1^2 c_{66} u_1^{(1)} + \kappa_1 e_{26}\phi^{(1)}\right) + \frac{3}{2b^3}\left[bT_{21}\left(b^-\right) + bT_{21}\left(-b^-\right)\right] = \rho\ddot{u}_1^{(1)},\\
&\frac{1}{2b}\left[D_2\left(b^-\right) - D_2\left(-b^-\right)\right] = 0,\\
&-3b^{-2}\left(\kappa_1 e_{26} u_1^{(1)} - \varepsilon_{22}\phi^{(1)}\right) + \frac{3}{2b^3}\left[bD_2\left(b^-\right) + bD_2\left(-b^-\right)\right] = 0.
\end{aligned} \tag{7-14}$$

The bottom of the plate surface is traction free with $T_{21}(-b^-) = 0$. At the top of the plate the shear stress is continuous, i.e., $T_{21}(b^-) = T_{21}(b^+)$ where b^+ is the upper limit of b. Since $D_2 \equiv 0$ in the fluid and the free space, the continuity of D_2 at the plate surfaces requires that $D_2(\pm b^-) = 0$. With these (7-14)$_3$ is trivially satisfied and (7-14)$_{1,2,4}$ become

$$\begin{aligned}
&\frac{1}{2b}T_{21}\left(b^+\right) = \rho\ddot{u}_1^{(0)},\\
&-3b^{-2}\left(\kappa_1^2 c_{66} u_1^{(1)} + \kappa_1 e_{26}\phi^{(1)}\right) + \frac{3}{2b^2}T_{21}\left(b^+\right) = \rho\ddot{u}_1^{(1)},\\
&\kappa_1 e_{26} u_1^{(1)} - \varepsilon_{22}\phi^{(1)} = 0.
\end{aligned} \tag{7-15}$$

We let

$$u_1^{(0)} = C_2 \exp(i\omega t), \quad u_1^{(1)} = C_3 \exp(i\omega t),$$
$$\phi^{(1)} = C_4 \exp(i\omega t), \tag{7-16}$$

where C_2 through C_4 are undetermined constants.

7.3.3 Boundary and Continuity Conditions

At the interface between the crystal plate and the fluid, we have the continuity of particle velocity

$$\dot{u}_1^{(0)} + b\dot{u}_1^{(1)} = v_1\left(b^+\right) . \tag{7-17}$$

Substituting the relevant fields in (7-11), (7-13) and (7-16) into (7-15) and (7-17) results in four linear equations for C_1 through C_4. For nontrivial solutions the determinant of the coefficient matrix has to vanish, which gives the following frequency equation:

$$\omega^2 - \frac{3\kappa_1^2 \bar{c}_{66}}{\rho b^2} = \frac{(1-i)\mu\eta}{2\rho b\omega}\left(\frac{3\kappa_1^2 \bar{c}_{66}}{\rho b^2} - 4\omega^2\right) . \tag{7-18}$$

7.3.4 Correction Factor

The exact fundamental TSh frequency from the 3D equations when the fluid is not present was given by [4]

$$\omega_0 = \frac{\pi}{2b}\sqrt{\frac{\bar{c}_{66}}{\rho}}, \quad \bar{c}_{66} = c_{66} + \frac{e_{26}^2}{\varepsilon_{22}} . \tag{7-19}$$

When a piezoelectric plate is in contact with a semi-infinite, low-viscosity fluid, the fundamental TSh frequency is approximately given by Chapter 4

$$\omega = \omega_0 (1 + \Delta\Omega), \tag{7-20}$$

where

$$\Delta\Omega = -\frac{1-i}{\pi}\sqrt{\frac{\rho_L \mu \omega_0}{2\rho \bar{c}_{66}}}, \tag{7-21}$$

$$\eta_0 = \sqrt{\rho_L \omega_0 /(2\mu)}. \tag{7-22}$$

Substitution of (7-21) into (7-18) determines

$$\kappa_1^2 = \frac{\pi^2}{12}(1 - \Delta\Omega). \tag{7-23}$$

We note that (7-23) is complex. Its real part is a negative frequency shift. Its imaginary part represents damped motion due to viscosity.

7.4 Propagating of FS and TT Waves

With κ_1 determined, the plate equations are ready to be used to study propagating waves in the plate, which is the main purpose of this chapter. We begin with coupled FS and TT waves and then examine uncoupled long FS and long TT waves separately.

7.4.1 Coupled Waves

For propagating waves with both x_2 and x_3 dependence, the equations for the fluid are

$$\begin{aligned} &T_{21,2} + T_{31,3} = \rho_L \dot{v}_1, \\ &T_{21} = \mu \frac{\partial v_1}{\partial x_2}, \quad T_{31} = \mu \frac{\partial v_1}{\partial x_3}. \end{aligned} \tag{7-24}$$

Substituting the stresses in $(7\text{-}24)_2$ into the equation of motion in $(7\text{-}24)_1$ gives

$$\mu(v_{1,22} + v_{1,33}) = \rho_L \dot{v}_1 \ . \tag{7-25}$$

We consider the following propagating wave that already satisfies (7-25):

$$v_1 = C_1 \exp\left[-\sqrt{\zeta^2 - 2i\eta^2}\,(x_2 - b) \right] \exp[i(\zeta x_3 - \omega t)], \tag{7-26}$$

where C_1 is an undetermined constant, and (7-12) is still valid. In the square root operation in (7-26) the root with a positive real part should be taken for decaying behavior at $x_2 = \infty$. The stress component needed in the interface condition is given by

$$T_{21} = \mu \frac{\partial v_1}{\partial x_2} = -\mu \sqrt{\zeta^2 - 2i\eta^2}\, C_1 \exp\left[-\sqrt{\zeta^2 - 2i\eta^2}\,(x_2 - b) \right] \exp[i(\zeta x_3 - \omega t)]. \tag{7-27}$$

For propagating waves in the crystal plate, we have

$$\begin{aligned} &u_1^{(0)} = C_2 \exp[i(\zeta x_3 - \omega t)], \quad u_1^{(1)} = C_3 \exp[i(\zeta x_3 - \omega t)], \\ &\phi^{(0)} = C_4 \exp[i(\zeta x_3 - \omega t)], \quad \phi^{(1)} = C_5 \exp[i(\zeta x_3 - \omega t)], \end{aligned} \tag{7-28}$$

where C_2 through C_5 are undetermined constants.

Substituting of (7-26)-(7-28) into (7-8) and (7-17), using $D_2(\pm b^-)=0$, we obtain five linear and homogeneous equations for C_1 through C_5. For nontrivial solutions the determinant of the coefficient matrix of has to vanish, which yields the frequency equation that determines the dispersion relations of ω versus ζ which is symbolically written as

$$f(\omega,\zeta)=0. \tag{7-29}$$

As a reference, the dispersion curves for the special case when the fluid is not present are shown in Fig. 7.2 for quartz in which the dimensionless wave number is defined by

$$\Omega=\frac{\omega}{\omega_0},\ Z=\zeta\Big/\frac{\pi}{2b}=X+iY. \tag{7-30}$$

The curve for the FS waves looks linear and therefore has little dispersion. The curve for the TT wave is curved and is clearly dispersive. The TT dispersion curve has a finite intercept with the Ω axis which is the cutoff frequency below which the wave cannot propagate. There are two vertical lines. One is at X=Re(Z)=0, the other is at Y=Im(Z) slightly larger than 1. These two lines are due to the equations of electrostatics in (7-8c) and (7-8d). If we neglect piezoelectric couplings and drop (7-8c) and (7-8d), these two vertical lines will disappear. When the fluid is not present, there is no damping in the system. The dispersion curves of FS and TT waves are either real or pure imaginary.

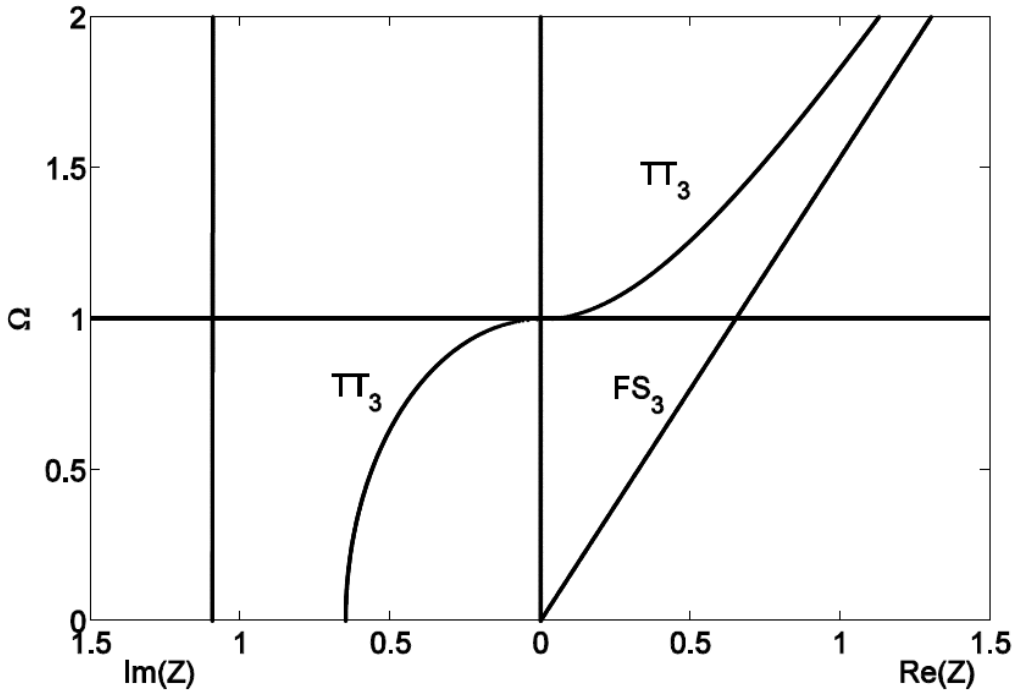

Fig. 7.2 Dispersion relations for coupled FS and TT waves in a plate alone without fluids.

When the fluid is present, for long waves which are important in applications, we expand (7-29) into power series of ζ and neglect powers higher than four. Then (7-29) can be approximated by

$$F(\omega)\zeta^4 + G(\omega)\zeta^2 = 0\,, \tag{7-31}$$

where

$$\begin{aligned} F(\omega) &= F_1\omega^{7/2} + F_2\omega^{5/2} + F_3\omega^{3/2} + F_4\omega^{1/2} + F_5\omega^4 + F_6\omega^2 + F_7\,, \\ G(\omega) &= G_1\omega^{7/2} + G_2\omega^{3/2} + G_3\omega^4 + G_4\omega^2\,, \end{aligned} \tag{7-32}$$

$$F_1 = 4iA_1\zeta_{33}\varepsilon_{33}\rho b^4, \tag{7-33a}$$

$$F_2 = 12iA_2\varepsilon_{22}\varepsilon_{33}\rho b^2 - 12iA_2\varepsilon_{23}^2\rho b^2, \tag{7-33b}$$

$$\begin{aligned} F_3 = {} & 9iA_1\varepsilon_{23}^2 c_{55} b^2 - 9iA_1\varepsilon_{22}\varepsilon_{33}c_{55}b^2 - 3iA_1\zeta_{33}\varepsilon_{33}\kappa_1^2 c_{66}b^2 - 3iA_1\zeta_{33}e_{36}^2\kappa_1^2 b^2 \\ & - 6iA_1\psi_{35}\varepsilon_{33}e_{26}\kappa_1 b^2 + 6iA_1\psi_{35}\varepsilon_{23}e_{36}\kappa_1 b^2 + 3iA_1\gamma_{55}\varepsilon_{23}^2 b^2 - 3iA_1\gamma_{55}\varepsilon_{22}\varepsilon_{33}b^2 \\ & + 18iA_1\varepsilon_{23}e_{25}e_{35}b^2 - 9iA_1\varepsilon_{22}e_{35}^2 b^2 - 9iA_1\varepsilon_{33}e_{25}^2 b^2, \end{aligned} \tag{7-33c}$$

$$F_4 = 9iA_2\varepsilon_{23}^2\kappa_1^2 c_{66} - 9iA_2\varepsilon_{22}\varepsilon_{33}\kappa_1^2 c_{66} + 18iA_2\varepsilon_{23}e_{26}e_{36}\kappa_1^2 - 9iA_2\varepsilon_{22}e_{36}^2\kappa_1^2 - 9iA_2\varepsilon_{33}e_{26}^2\kappa_1^2, \tag{7-33d}$$

$$F_5 = \zeta_{33}\varepsilon_{33}\rho^2 b^4, \tag{7-33e}$$

$$\begin{aligned} F_6 = {} & -3\zeta_{33}\varepsilon_{33}\kappa_1^2 c_{66}\rho b^2 - 3\zeta_{33}e_{36}^2\kappa_1^2\rho b^2 + 3\gamma_{55}\varepsilon_{23}^2\rho b^2 - 3\gamma_{55}\varepsilon_{22}\varepsilon_{33}\rho b^2 \\ & + 6\psi_{35}\varepsilon_{23}e_{36}\kappa_1\rho b^2 - 6\psi_{35}\varepsilon_{33}e_{26}\kappa_1\rho b^2 + 3\varepsilon_{23}^2 c_{55}\rho b^2 - 3\varepsilon_{22}\varepsilon_{33}c_{55}\rho b^2 \\ & + 6\varepsilon_{23}e_{25}e_{35}\rho b^2 - 3\varepsilon_{33}e_{25}^2\rho b^2 - 3\varepsilon_{22}e_{35}^2\rho b^2, \end{aligned} \tag{7-33f}$$

$$\begin{aligned} F_7 = {} & 9\varepsilon_{23}^2\kappa_1^2 c_{56}^2 - 9\varepsilon_{23}^2\kappa_1^2 c_{55}c_{66} + 9\varepsilon_{22}\varepsilon_{33}\kappa_1^2 c_{55}c_{66} - 9\varepsilon_{22}\varepsilon_{33}\kappa_1^2 c_{56}^2 \\ & + 18\varepsilon_{23}e_{25}e_{36}\kappa_1^2 c_{56} + 18\varepsilon_{23}e_{26}e_{35}\kappa_1^2 c_{56} - 18\varepsilon_{22}e_{35}e_{36}\kappa_1^2 c_{56} - 18\varepsilon_{33}e_{25}e_{26}\kappa_1^2 c_{56} \\ & + 9\varepsilon_{22}e_{36}^2\kappa_1^2 c_{55} + 9\varepsilon_{33}e_{26}^2\kappa_1^2 c_{55} - 18\varepsilon_{23}e_{26}e_{36}\kappa_1^2 c_{55} \\ & + 9\varepsilon_{22}e_{35}^2\kappa_1^2 c_{66} + 9\varepsilon_{33}e_{25}^2\kappa_1^2 c_{66} - 18\varepsilon_{23}e_{25}e_{35}\kappa_1^2 c_{66} \\ & + 9e_{25}^2 e_{36}^2\kappa_1^2 + 9e_{26}^2 e_{35}^2\kappa_1^2 - 18e_{25}e_{26}e_{35}e_{36}\kappa_1^2, \end{aligned} \tag{7-33g}$$

$$G_1 = 12iA_1\varepsilon_{22}\varepsilon_{33}\rho b^2 - 12iA_1\varepsilon_{23}^2\rho b^2, \tag{7-34a}$$

$$G_2 = 9iA_1\varepsilon_{23}^2\kappa_1^2 c_{66} - 9iA_1\varepsilon_{22}\varepsilon_{33}\kappa_1^2 c_{66} + 18iA_1\varepsilon_{23}e_{26}e_{36}\kappa_1^2 - 9iA_1\varepsilon_{22}e_{36}^2\kappa_1^2 - 9iA_1\varepsilon_{33}e_{26}^2\kappa_1^2, \tag{7-34b}$$

$$G_3 = 3\varepsilon_{22}\varepsilon_{33}\rho^2 b^2 - 3\varepsilon_{23}^2\rho^2 b^2, \tag{7-34c}$$

$$G_4 = 9\varepsilon_{23}^2\kappa_1^2 c_{66}\rho - 9\varepsilon_{22}\varepsilon_{33}\kappa_1^2 c_{66}\rho + 18\varepsilon_{23}e_{26}e_{36}\kappa_1^2\rho - 9\varepsilon_{22}e_{36}^2\kappa_1^2\rho - 9\varepsilon_{33}e_{26}^2\kappa_1^2\rho, \tag{7-34d}$$

$$A_1 = \frac{1}{2b}\sqrt{-i\mu\rho_L}\,, \quad A_2 = \frac{1}{4b}\sqrt{\frac{i\mu^3}{\rho_L}}\,. \tag{7-35}$$

Next we examine (7-31) for FS and TT waves separately.

7.4.2 Long FS Waves

For the FS branch, when ζ is small, ω is also small and is of the same order (see Fig. 7.2). In this case, neglecting higher powers of ω, (7-31) can be approximated by

$$F_7\zeta^2 + G_2\omega^{3/2} + G_4\omega^2 = 0\,, \tag{7-36}$$

where the effect of the fluid is represented by the second term. When the fluid is not present, denoting the wave frequency by ω_{Plate}, (7-36) reduces to the following known dispersion relation for long FS waves [5]:

$$\omega_{\text{Plate}} = \sqrt{\frac{c_{66}c_{55} - c_{56}^2}{\rho c_{66}}}\,\zeta = \sqrt{\frac{\gamma_{55}}{\rho}}\,\zeta\,, \tag{7-37}$$

which is nondispersive.

For numerical results we consider three common crystal plates of AT-cut quartz, Y-cut langasite, and Y-cut langanite. The plate thickness is fixed with b=1mm which is typical for crystal devices. For the fluid we choose, as an example, chloroform with $\rho_L = 1.483\times10^3\,\text{kg/m}^3$ and a relatively low viscosity of $\mu = 0.542\,\text{mPas}$ (smaller than the viscosity of water). We consider real frequencies and solve (7-36) for complex wave numbers.

Figure 3 shows the effect of viscosity on the dispersion relation of long FS waves with a small *Z*. The ω_0 of quartz is used as a common normalizing frequency. The curves for langasite and langanite are close to each other because their material constants are close. When the fluid is present, an immediate observation is that the second term of (7-36) makes the dispersion curves complex in Fig. 7.3 (a), indicating energy absorption in the fluid due to viscosity and the related wave attenuation. Fig. 7.3 (b) shows the real parts of the dispersion relations which are essentially linear and hence the fluid induced dispersion is small. Fig. 7.3 (c) shows the imaginary parts of the dispersion curves which are positive, representing attenuation for the right-traveling waves given in (7-28).

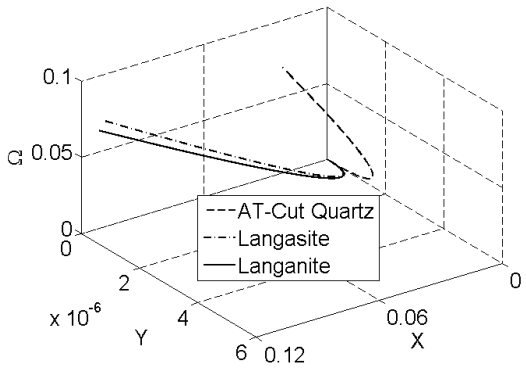

(a)

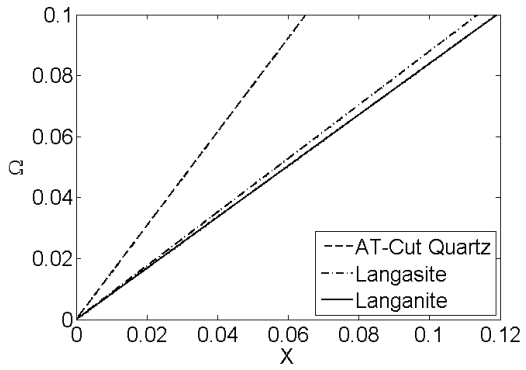

(b)

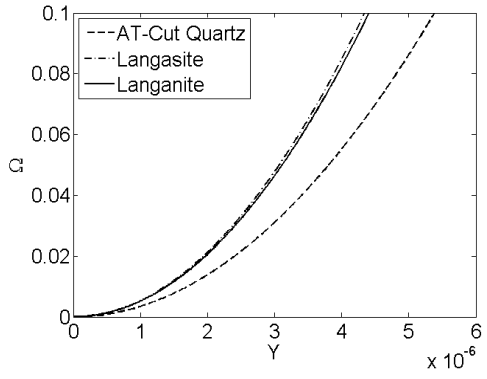

(c)

Fig. 7.3 Dispersion curves of long FS waves for different materials.

Fig. 7.4 shows the effects of the fluid viscosity and piezoelectric coupling on wave frequencies through the real parts of the dispersion relations. The results for quartz, langasite, and langanite are shown separately in (a), (b), and (c). For each material the special case when the plate is alone without the fluid and piezoelectric coupling is used as a reference. This special case may be denoted by $\mu = 0$ and e=0 where e represents piezoelectric coupling. Since the effects of viscosity and piezoelectric coupling are small, the relative frequency shifts from the reference ($\Delta\Omega = \Omega - \Omega_{\text{Plate}}$) are shown in the figure. The effect of piezoelectric coupling is roughly of the order of 10^{-4}. Therefore it should be included in the analysis, or it can be experimentally determined through calibration of devices. Once the piezoelectric effect is taken into consideration, the effect of viscosity on frequency can be used to measure fluid viscosity. The fluid viscosity lowers the frequency as expected, whether piezoelectric coupling is considered or not. The relative frequency shift due to viscosity is of the order of 10^{-5} which is considered a significant frequency change because the thermal noise in crystal resonators is of the order of 10^{-6}. Therefore a 10^{-5} frequency shift is a clear and measurable signal. As shown in (7-21), the fluid viscosity and density appear together in a product in the first-order approximation of the frequency shift. In a typical application, one needs to know either the fluid density or viscosity and then uses an acoustic wave fluid sensor to measure the other. How to separate the density from viscosity still remains a challenging problem in acoustic wave fluid sensors.

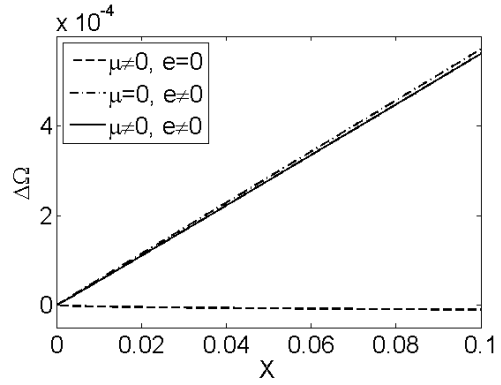

(a)

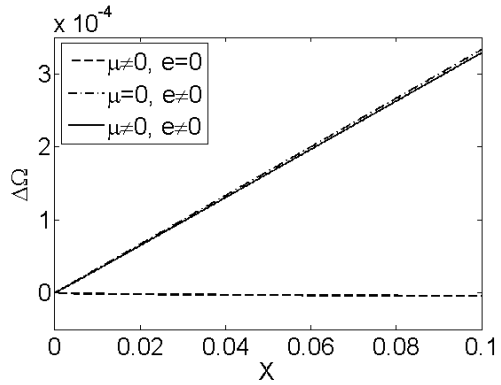

(b)

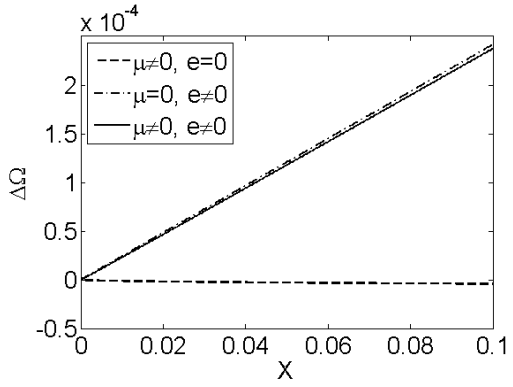

(c)

Fig. 7.4 Effects of viscosity and piezoelectric coupling on long FS waves.

7.4.3 Long TT Waves

For the TT branch, when ζ is small, ω is finite (see Fig. 7.2). In this case, we denote

$$\omega = \omega_0 \left(1 + \frac{\Delta\omega}{\omega_0} \right) \tag{7-38}$$

where $\Delta\omega/\omega_0$ is small. Substituting (7-38) into (7-31), for small $\Delta\omega/\omega_0$, we obtain

$$\begin{aligned} \frac{\omega - \omega_0}{\omega_0} = & -\frac{F_1{\omega_0}^{7/2} + F_2{\omega_0}^{5/2} + F_3{\omega_0}^{3/2} + F_4{\omega_0}^{1/2} + F_5{\omega_0}^4 + F_6{\omega_0}^2 + F_7}{\frac{7}{2}G_1{\omega_0}^{7/2} + \frac{3}{2}G_2{\omega_0}^{3/2} + 4G_3{\omega_0}^4 + 2G_4{\omega_0}^2}\zeta^2 \\ & - \frac{G_1{\omega_0}^{7/2} + G_2{\omega_0}^{3/2} + G_3{\omega_0}^4 + G_4{\omega_0}^2}{\frac{7}{2}G_1{\omega_0}^{7/2} + \frac{3}{2}G_2{\omega_0}^{3/2} + 4G_3{\omega_0}^4 + 2G_4{\omega_0}^2}. \end{aligned} \tag{7-39}$$

(7-39) shows that locally, near cutoff, the dispersion curve of TT waves can be approximated by a parabola and therefore long TT waves are dispersive.

Numerical results for long TT waves are shown in Figs. 7.5. When there is no fluid, part of the dispersion curve of TT waves is real and the rest is pure imaginary (Fig. 7.5 (a)). When the fluid is present, the dispersion curves in Fig. 7.5 (b) look the same as those in Fig. 7.5 (a). To see the difference we magnify Fig. 7.5 (b) for smaller values of *Z* and show the results in Fig. 7.5 (c). It can be seen from Fig. 7.5 (c) that the dispersion curves become complex and do not go through the Ω axis. We note that when $\zeta = 0$ (7-39) reduces to

$$\frac{\omega}{\omega_0} = 1 - \frac{G_1\omega_0^{7/2} + G_2\omega_0^{3/2} + G_3\omega_0^{4} + G_4\omega_0^{2}}{\frac{7}{2}G_1\omega_0^{7/2} + \frac{3}{2}G_2\omega_0^{3/2} + 4G_3\omega_0^{4} + 2G_4\omega_0^{2}}, \tag{7-40}$$

which is complex. The last term on the right-hand side of (7-40) depends on ε_{23}, ε_{33}, and e_{36}. Therefore it is related to E_3 which is not present in the analysis of TSh modes in Section 3. This accounts for the small deviation from 1 when Z=0 in Fig. 7.5 (a).

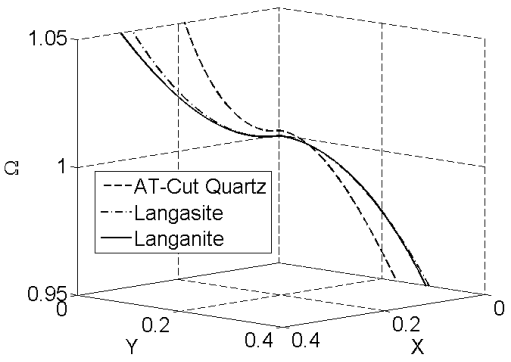

(a)

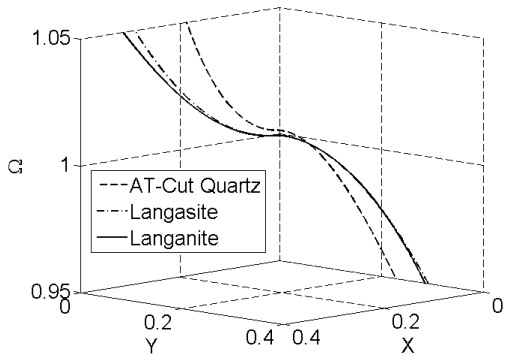

(b)

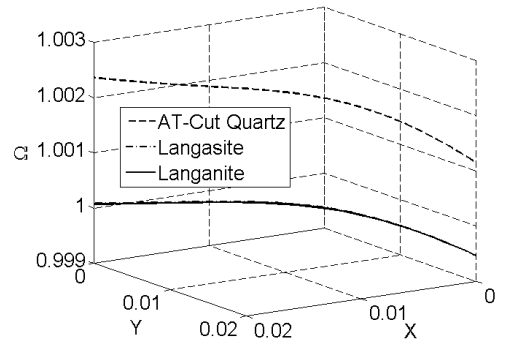

(c)

Fig. 7.5 Dispersion relation of long TT waves. (a) Without fluid. (b) With fluid. (c) With fluid (magnified).

7.5 Conclusion

Analytical solutions are obtained for TSh modes and long FS as well as long TT waves in a piezoelectric plate in contact with a viscous fluid. Contrasted to Chapter 6, this chapter has a simpler fluid layer. Therefore, we consider the electrical coupling in the plate. The frequencies and dispersion relations become complex due to the fluid, indicating damped modes and waves with attenuation. The fluid viscosity and density lower the frequencies together in a combined manner, causing (additional) dispersion. Long FS waves become slightly dispersive due to the fluid. The effect of piezoelectric coupling is roughly of the order of 10^{-4}. As a consequent, it should be included in the analysis. Typical relative frequency shifts due to the fluid are of the order of 10^{-5} which is detectable by crystal resonators and waveguides. The results obtained are fundamental and useful for the understanding and design of quartz crystal fluid sensors.

7.6 References

[1] R. D. Mindlin, "High frequency vibrations of piezoelectric crystal plates," Int. J. Solids Structures, 8 (7), 895-906, 1972.

[2] J. S. Yang, "An Introduction to the Theory of Piezoelectricity," Springer, 57, 2005.

[3] R. L. Panton, "Incompressible Flow," John Wiley and Sons, New York, 1984

[4] H. F. Tiersten, "A corrected modal representation of thickness vibrations in quartz plates and its influence on the transversely varying case," IEEE Trans. Ultrason., Ferroelect., Freq. Contr., 50, 1436-1443, 2003

[5] R. D. Mindlin, "Face-shear waves in rotated Y-cut quartz plates," Mechanics of the Solid State, F. P. J. Rimrott and J. Schwaighofer (eds.), University of Toronto Press, 1968, 143-145.

8. Conclusion

Since piezoelectrical plates with lateral electrical field as fluid sensors attract more and more attentions, the lack of the theoretical research on such plates will be a limitation to the development of those fluid sensors. Hence, we did several theoretical analyses on the piezoelectrical plates with lateral electrical field.

When an At-cut quartz plate is under LFE, the dominating displacements are FS and TT. Within the first-order plate theory, there is only one resonance for pure thickness vibration. For straight-crested waves, the two electrostatic equations contribute to two branches in the dispersion relations, in addition to the two branches for FS and TT waves. Frequency spectra of finite plates consists of the "sum" of those of FS and TT modes with mode veering at the intersections. To avoid strong couplings between FS and TT, certain values of the plate length/thickness ratio should be avoided. Mindlin's first-order plate theory is effective in analyzing vibrations of crystal plates under LFE.

Then, we find that when an AT-cut quartz plate under LFE has partial mass layers, there are a finite number of resonances in the frequency range between the cutoff frequencies of a plate with mass layers and a plate without mass layers. The motional capacitance assumes maxima at these resonances. The corresponding displacement distributions show energy trapping, with the vibration mainly in the part of the plate with mass layers. The number of trapped modes increases with the length of the mass layers. Lower-order modes are trapped better. Due to the coupling to the FS mode which cannot be trapped, the vibration can still feel the plate boundary slightly. These results can be

utilized in mounting a LFE sensor to avoid the external perturbation introduced by the mounts.

As these plates are used as fluid sensors, an exact solution is obtained for thickness-shear vibrations of a rotated Y-cut quartz plate in contact with a fluid driven by a lateral electric field. An approximate expression for the frequency shifts due to the fluid is presented. The fluid density and viscosity tend to lower the frequencies of the crystal plate. Higher-order modes are less sensitive to the fluid than lower-order modes. The relative frequency shift is of the order of 10^{-4}.

In the real LFE sensors, the electrical field lines, penetrating into the quartz plate and the liquid layer, also have an x_2-directed component, which makes the real LFE sensors sensitive to the fluid electrical property, such as permittivity. We introduced a model of TFE sensor with one electrode separated to qualitatively describe the effect of the liquid permittivity on the frequency shifts in a real LFE liquid sensor. An exact solution is obtained for thickness-shear vibrations of such model in contact with a fluid. An approximate expression for the frequency shifts due to the fluid is presented. The expression contains two parts. One is exactly what we have in Chapter 4. The other is related to the permittivity of the fluid. The fluid permittivity, density and viscosity tend to lower the frequencies of the crystal plate. These results show the same tendency given by the experimental results. Furthermore, the higher-order modes are less sensitive to the fluid than lower-order modes.

Finally, we studied the propagation of shear-horizontal waves in a piezoelectric plate in contact with a fluid layer as an acoustic wave sensor for measuring fluid viscosity or density. Two kinds of fluid layers are applied. One is with finite thickness, and the other one is semi-infinite. Approximate dispersion relations for long face-shear and thickness-twist waves are given analytically. In the first one, the results only show the effects of the fluid on wave characteristics. In the other, the results showing the effects of the fluid and the piezoelectric coupling in the plate on wave characteristics are presented. Analytical solutions are obtained for TSh modes and long FS as well as long TT waves in a piezoelectric plate in contact with a viscous fluid. The frequencies and dispersion relations become complex due to the fluid, indicating damped modes and waves with attenuation. The fluid viscosity and density lower the frequencies together in a combined manner, causing (additional) dispersion. Long FS waves become slightly dispersive due to the fluid. Typical relative frequency shifts due to the fluid are of the order of 10-5 which is detectable by crystal resonators and waveguides. Furthermore, the second case shows the effect of piezoelectric coupling is roughly of the order of 10^{-4}. Therefore it should be included in the analysis. The results obtained are fundamental and useful for the understanding and design of quartz crystal fluid sensors.

Appendix A

Electroelastic Material Constants

Material constants of a few piezoelectrics are summarized below. The numerical results given in this dissertation are calculated from these constants.

Permittivity of free space $\varepsilon_0 = 8.854 \times 10^{-12} \, Faraday/m$.

AT-cut quartz

AT-cut quartz is special case of rotated Y-cut quartz, whose material constants are [1]

$\rho = 2649 kg/m^3$,

$$[c_{pq}] = \begin{bmatrix} 86.74 & -8.25 & 27.15 & -3.66 & 0 & 0 \\ -8.25 & 129.77 & -7.42 & 5.7 & 0 & 0 \\ 27.15 & -7.42 & 102.83 & 9.92 & 0 & 0 \\ -3.66 & 5.7 & 9.92 & 38.61 & 0 & 0 \\ 0 & 0 & 0 & 0 & 68.81 & 2.53 \\ 0 & 0 & 0 & 0 & 2.53 & 29.01 \end{bmatrix} \times 10^9 \, N/m^2,$$

$$e_{ip} = \begin{pmatrix} 0.171 & -0.152 & -0.0187 & 0.067 & 0 & 0 \\ 0 & 0 & 0 & 0 & 0.108 & -0.095 \\ 0 & 0 & 0 & 0 & -0.0761 & 0.067 \end{pmatrix} C/m^2,$$

$$\varepsilon_{ij} = \begin{pmatrix} 39.21 & 0 & 0 \\ 0 & 39.82 & 0.86 \\ 0 & 0.86 & 40.42 \end{pmatrix} \times 10^{-12} C/Vm.$$

Langasite

The material constants of Langasite are [2]

$$\rho = 5743 kg/m^3,$$

$$[c_{pq}] = \begin{bmatrix} 18.875 & 10.475 & 9.589 & -1.412 & 0 & 0 \\ 10.475 & 18.875 & 9.589 & 1.412 & 0 & 0 \\ 9.589 & 9.589 & 26.14 & 0 & 0 & 0 \\ -1.412 & 1.412 & 0 & 5.35 & 0 & 0 \\ 0 & 0 & 0 & 0 & 5.35 & -1.412 \\ 0 & 0 & 0 & 0 & -1.412 & 4.2 \end{bmatrix} \times 10^{10} N/m^2,$$

$$e_{ip} = \begin{pmatrix} -0.44 & 0.44 & 0 & -0.08 & 0 & 0 \\ 0 & 0 & 0 & 0 & 0.08 & 0.44 \\ 0 & 0 & 0 & 0 & 0 & 0 \end{pmatrix} C/m^2,$$

$$\varepsilon_{ij} = \begin{pmatrix} 167.5 & 0 & 0 \\ 0 & 167.5 & 0 \\ 0 & 0 & 448.9 \end{pmatrix} \times 10^{-12} C/Vm.$$

Langanite

The material constants of Langanite are [3]

$$\rho = 5934 kg/m^3,$$

$$[c_{pq}] = \begin{bmatrix} 19.07 & 10.93 & 9.82 & 1.35 & 0 & 0 \\ 10.93 & 19.07 & 9.82 & -1.35 & 0 & 0 \\ 9.82 & 9.82 & 26.05 & 0 & 0 & 0 \\ 1.35 & -1.35 & 0 & 5.04 & 0 & 0 \\ 0 & 0 & 0 & 0 & 5.04 & 1.35 \\ 0 & 0 & 0 & 0 & 1.35 & 4.07 \end{bmatrix} \times 10^{10} N/m^2,$$

$$e_{ip} = \begin{pmatrix} -0.44 & 0.44 & 0 & 0.05 & 0 & 0 \\ 0 & 0 & 0 & 0 & -0.05 & 0.44 \\ 0 & 0 & 0 & 0 & 0 & 0 \end{pmatrix} C/m^2,$$

$$\varepsilon_{ij} = \begin{pmatrix} 20.2 & 0 & 0 \\ 0 & 20.2 & 0 \\ 0 & 0 & 79.4 \end{pmatrix} \varepsilon_0.$$

References

[1] H. F. Tiersten, “Linear Piezoelectric Plate Vibrations”, Plenum, New York, 1969.

[2] B. P. Sorokin, P. P. Turchin, S. I. Burkov, D. A. Glushkov and K. S. Alexandrov, “Influence of static electric field, mechanical pressure and temperature on the propagation of acoustic waves in $La_3Ga_5SiO_{14}$ piezoelectric single crystals,” in: *Proc.* IEEE Int. Frequency Control Symp.,161-169, 1996.

[3] Yu. V. Pisarevsky, P. A. Senushencov and P. A. Popov B. V. Mill, “New strong piezoelectric $La_3Ga_{5.5}Nb_{0.5}O_{14}$ with temperature compensation cuts,” in: *Proc.* IEEE Int. Frequency Control Symp., 653-656, 1996.